SHIPS IN ICE:
THE INTERACTION PROCESS AND PRINCIPLES OF DESIGN

CENTRE FOR NEWFOUNDLAND STUDIES

TOTAL OF 10 PAGES ONLY
MAY BE XEROXED

(Without Author's Permission)

BIN ZOU

001311

CENTRE FOR NFLD. STUDIES
MEMORIAL UNIVERSITY
OF NEWFOUNDLAND

INFORMATION TO USERS

This manuscript has been reproduced from the microfilm master. UMI films the text directly from the original or copy submitted. Thus, some thesis and dissertation copies are in typewriter face, while others may be from any type of computer printer.

The quality of this reproduction is dependent upon the quality of the copy submitted. Broken or indistinct print, colored or poor quality illustrations and photographs, print bleedthrough, substandard margins, and improper alignment can adversely affect reproduction.

In the unlikely event that the author did not send UMI a complete manuscript and there are missing pages, these will be noted. Also, if unauthorized copyright material had to be removed, a note will indicate the deletion.

Oversize materials (e.g., maps, drawings, charts) are reproduced by sectioning the original, beginning at the upper left-hand corner and continuing from left to right in equal sections with small overlaps. Each original is also photographed in one exposure and is included in reduced form at the back of the book.

Photographs included in the original manuscript have been reproduced xerographically in this copy. Higher quality 6" x 9" black and white photographic prints are available for any photographs or illustrations appearing in this copy for an additional charge. Contact UMI directly to order.

UMI

A Bell & Howell Information Company
300 North Zeeb Road, Ann Arbor MI 48106-1346 USA
313/761-4700 800/521-0600

SHIPS IN ICE:
THE INTERACTION PROCESS AND PRINCIPLES OF DESIGN

BY

©BIN ZOU, M.ENG., B.ENG.

A Thesis submitted to the School of Graduate Studies
in partial fulfillment of the degree of
Doctor of Philosophy

Faculty of Engineering and Applied Science
Memorial University of Newfoundland
May, 1996

St. John's Newfoundland

National Library of Canada
Acquisitions and Bibliographic Services
395 Wellington Street
Ottawa ON K1A 0N4
Canada

Bibliothèque nationale du Canada
Acquisitions et services bibliographiques
395, rue Wellington
Ottawa ON K1A 0N4
Canada

Your file Votre référence

Our file Notre référence

The author has granted a non-exclusive licence allowing the National Library of Canada to reproduce, loan, distribute or sell copies of this thesis in microform, paper or electronic formats.

L'auteur a accordé une licence non exclusive permettant à la Bibliothèque nationale du Canada de reproduire, prêter, distribuer ou vendre des copies de cette thèse sous la forme de microfiche/film, de reproduction sur papier ou sur format électronique.

The author retains ownership of the copyright in this thesis. Neither the thesis nor substantial extracts from it may be printed or otherwise reproduced without the author's permission.

L'auteur conserve la propriété du droit d'auteur qui protège cette thèse. Ni la thèse ni des extraits substantiels de celle-ci ne doivent être imprimés ou autrement reproduits sans son autorisation.

0-612-23115-1

Canada

To June and Jamie

Abstract

For ships operating in arctic and sub-arctic waters, ice load is a major threat. Due to the uncertainties in ice conditions and varying operating situations, an accurate estimation on design ice load is difficult. The objective of the present research is to investigate the ice loads and the associated structural strength from aspects of mechanics, statistics and design principles.

First, the ice-structure interaction process is investigated from the view point of mechanics. The interaction is characterized by ice fracture and damage. The ice load is highly localized within high pressure regions termed critical zones. A numerical analysis was carried out to investigate how a crack may propagate in an ice sheet and how the ice material is damaged during an ice-structure interaction. The analysis showed that small shear cracks, with mixed modes, are more likely the candidates for the fracture spalls and the formation of critical zones.

Critical zones vary in space and time. These critical zones are characterized using parameters such as spatial density, zonal area, and the zonal force. These parameters in the model were calibrated using ship trial data of CCGS Louis St. Laurent. The ice loads on a design area were modelled as a random number of critical zones, each with a random force. Based on this model and extreme value theory, a design curve was proposed for the estimation of extreme ice loads.

Third, the strength of the structure was investigated. A long plate, loaded by uniform pressure was proposed as the design model for the plating. Due to the randomness of ice load, there are uncertainties associated with the design model. To understand this uncertainty, various load scenarios were investigated using the finite element method. The results show that the plate fails at a dominant section, which fails in a way similar to an "equivalent long plate". Factors affecting the failure of the panel are lateral support and

interaction between critical zones. These factors were investigated and empirical formula were derived based on finite element modelling.

A simplified model was proposed to investigate the failure of the "equivalent long plate". This model was used, together with factors of lateral support, location and interactions between critical zones from empirical formula, in Monte Carlo simulation scheme to model the uncertainty of the design model of the structure. The simulated results of the uncertainty factor were approximated by a lognormal distribution.

Finally, the results from the analysis on the ice loads and the structural resistance were used in discussion of the design principles. Two design methods, i.e., reliability design and code design methods, were discussed. Principles in selecting design load and resistance were discussed. These principles were applied in an example design of an offshore oil tanker. Reliability of the plates from different design strategies were evaluated. It was found that, for ultimate rupture, a yearly maximum with a probability of exceedance of 10^{-4} is appropriate as the design load.

Acknowledgments

I am greatly indebted to my supervisor, Dr. Ian Jordaan, NSERC/Mobil Industrial Research Professor in Ocean Engineering, Memorial University, for his inspiration and support throughout the project. He taught me a new method in approaching an engineering problem, which also affected my way of everyday thinking.

I would also like to thank my co-supervisors, Dr. M.R. Haddara, Chairman, Naval Architecture and Ocean Engineering at Memorial University, and Dr. G. Timco, National Research Council Canada, for their advises and suggestions. Their help, especially in the latter stages of the project, is very much appreciated.

During the project, I had the opportunity to work with Dr. Frederking, Dr. B. Parsons, Mr. D. Spencer of National Research Council, Dr. J. Dempsey of Clarkson University and Dr. M. Kachnov of Tuft's University. Their suggestions and encouragement are appreciated.

The help and encouragement offered by my colleagues, Mr. Jing Xiao, Dr. R. McKenna, Mr. Mark Fuglem, Ms. M. Johnston, Dr. Sanjay Singh, Dr. Dmitri Matskevitch, Mr. Barry Stone, Ms. Karen Muggeridge, Mr. Trevor Butler and Mr. Bin Liu are greatly appreciated.

I am deeply indebted to my family members, my wife June, my son Jamie, my parents and parents in law who kept me in the state with full of hope and energy.

Financial support for this work was provided by the Natural Sciences and Engineering Research Council of Canada (NSERC), Centre for Cold Ocean Resource Engineering (C-CORE), Offshore Development Fund, National Energy Board. The courtesy and generosity of these organizations is gratefully acknowledged.

Contents

Abstract III

Acknowledgments V

Contents VI

List of Figures X

List of Tables XV

Nomenclature XVI

Chapter 1 Introduction 1

1.1 Overview 1

1.2 Scope of the Work 4

Chapter 2 Ice-Structure Interaction Process 6

2.1 Introduction 6

2.2 Ice Fracture 9

2.3 Analysis of Kendall's Double Cantilever Beam Theory 11

2.4 Analysis of Beam Model By Hutchinson and Suo 22

2.5 Analysis of Small Cracks at Different Locations 28

2.6 Ice Damage 31

2.7 Fracture and Damage Interplay in Ice-Structure Interaction 34

2.8 Conclusions 37

Chapter 3 Probabilistic Analysis of Ice Loads 38

3.1 Introduction 38

3.2 Extremal Analysis 43

3.3 Previous Experience in Statistical Analysis of Ice Loads 47

3.3.1 Overview 47

3.3.2 An Approach Based on Data of Ship Ramming Trials 47

3.4 Statistical Analysis of Critical Zones 52

3.4.1 Definition of the Problem 52

3.4.2 Analysis of Ship Trial Data of Louis St. Laurent 53

3.4.3 The Probabilistic Model 62

3.4.4 Application and Results 67

3.5 Exposure 72

3.5.1 Statistics of Ice Loads in The Baltic 75

3.5.2 Comparison of the Different Duration of Interactions 78

3.6 Concluding Remarks 78

Chapter 4 Structural Strength 81

4.1 Introduction 81

4.2 The Long Plate Model 84

4.2.1 Two-Hinge and Three-Hinge Failure 86

4.2.2 Membrane Action and Ultimate Rupture 88

4.2.3 Finite Element Analysis of A Long Plate 91

4.3 The Patch Load Model 94

4.3.1 Model Development 94

4.3.2 Results 101

4.3.3 Finite Element Analysis 103

4.4 Structural Response to Critical Zonal Forces 105

4.5 Design Strategy 110

4.6 Conclusions and Recommendations 112

Chapter 5 A Probabilistic Analysis of The Design Model 114

5.1 Introduction 114

5.2 Structural Response to Realistic Loads 115

5.2.1 Cases With One Critical Zone 116

5.2.2 The Case With Two or More Critical Zones 124

5.3 A Long Plate Loaded By Non-Uniform Forces 131

5.3.1 Three Hinge Mechanism 131

5.3.2 Membrane Action and Ultimate Rupture 134

5.3.3 Results and Comparison With Finite Element Modelling 137

5.4 Modeling of the Uncertainty in the Design Model 139

5.4.1 The Model 139

5.4.2 Results 142

5.6 Conclusions and Recommendations 145

Chapter 6 Design Principles 146

6.1 Introduction 146

6.2 Design Methods 147

6.2.1 Reliability Method 150

6.2.2 Code Design 152

6.3 Design Load 154

6.3.1 Exposure 155

6.3.2 Specified Load and Load Factor 157

6.3.3 Design Ice Load for the Concept Design 161

6.4 Resistance of the Structure 161

6.5 Design of the Plating 163

6.5.1 Dynamic Yield and Dynamic Ultimate Stresses *164*

6.5.2 Design of Plate Thickness and Risk Analysis *166*

6.6 Conclusions and Recommendations 168

Chapter 7 Concluding Remarks **171**

Reference **174**

List of Figures

Figure 2. 1 Schematic Illustration of A Critical Zone with Spalls 7

Figure 2. 2 Angle of Crack Propagation (Palaniswamy and Knauss, 1974) 12

Figure 2. 3 Data of Shen and Lin (1986) Fitted to the Maximum SERR Analysis of Palaniswamy and Knauss (1974). Data Normalized with K_I=0.107 MPa $m^{1/2}$ 12

Figure 2. 4 Kendall's double cantilever beam 13

Figure 2. 5 Kendall's model for the crack off the center line (from Kendall 1978) 15

Figure 2. 6 Struts with no constrains at free ends 16

Figure 2. 7 Double Cantilever Beam with restrained ends from DeFranco and Dempsey (1990) 17

Figure 2. 8 An ice sheet with a central crack, loaded by an indentor 18

Figure 2. 9 (a) Results of strain energy release rate, (b) detail of figure (a) 20

Figure 2. 10 An ice sheet with crack in different vertical locations 21

Figure 2. 11 G values for cracks at different locations 22

Figure 2. 12 A Beam Model by Suo (1990) 23

Figure 2. 13 An Idealized Ice-Structure Interaction 25

Figure 2. 14 Analysis on the effect of location of the crack 26

Figure 2. 15 Analysis on effect of w 27

Figure 2. 16: Analysis on the effect of x_0 27

Figure 2. 17 Results of Monte Carlo Simulations 29

Figure 2. 18 Tensile Stress Zone and Shear stress Zones 31

Figure 2. 19 G Values of Different Crack Lengths 32

Figure 2. 20 Schematic Illustration of Pressure Variation During the Interaction Process 35

Figure 2. 21 Effect of Spalls on Total Force 36

Figure 3. 1 Schematic View of Three Regions of Pressure within a Design Window. 39

Figure 3. 2 Critical Zone Activity Within the Contact Area, (based on Blount et al., 1981, Case I) 40

Figure 3. 3 The Tail of a Distribution 46
Figure 3. 4 Ranked Data on Local Pressure Measured Onboard the USCGC Polar Sea. (Jordaan et al. 1993a) 49
Figure 3. 5 Results of α for ln p_e vs. x Plots (Jordaan et al., 1993a) 50
Figure 3. 6 Probability density of extreme pressure (Jordaan et al., 1993a) 53
Figure 3. 7 Schematic Illustration of Contact Area, Critical Zones and Design Windows 54
Figure 3. 8 Location of Various Pressure Sensors (dashed circles indicate sensors in inactive region, each rectangular in solid lines indicates the area a pressure sensor represents in approach B) 56
Figure 3. 9 Approximation of Critical Zones 57
Figure 3. 10 Time Slices Correspond to Peak Pressures 61
Figure 3. 11 Probability of Critical Zonal Force 62
Figure 3. 12 Schematic View of A Design with The Critical Zones 63
Figure 3. 13 Modelling of Critical Zonal Forces 66
Figure 3. 14 Probability of Local Pressure (Results of Approach A) 69
Figure 3. 15 Probability of Local Pressure (Results of Approach B) 69
Figure 3. 16 Results of α Values 70
Figure 3. 17 Results of x_0 Values 70
Figure 3. 18 Modified Values of x_0 for Maximum Pressure Per Ram 72
Figure 3. 19 Schematic Diagram Showing Time Traces for a) a Ram and b) a Continuous Interaction(from Jordaan et al., 1993a) 74
Figure 3. 20 The most probable extreme loads obtained as a function of days in ice in various sea area for the bow frame (FFR2) (From Kujala, 1991, Figure 14) 76
Figure 3. 21 Comparison Between Canadian Arctic Class and Baltic Class 79

Figure 4. 1 A Ship Panel Subjected by Ice Impact Loads 83
Figure 4. 2 Schematic Illustration of Plastic Failure Mechanism (based on Carter et al., 1992). 85

Figure 4. 3(a) Schematic Diagram of a Plate With Fixed Ends and Loaded by Lateral Pressure, (b) Distribution of Bending Moment. 87
Figure 4. 4 Schematic Diagram of Three Hinge Mechanism. 88
Figure 4. 5 Schematic Diagram of Membrane Action 89
Figure 4. 6 Schematic Diagram of Membrane Action Failure Mechanism. 90
Figure 4. 7 Mechanical Properties of Material 91
Figure 4. 8 A section of the deflected plate and the distribution of the principal strains. 93
Figure 4. 9 Illustration of Different Failure Mechanism 93
Figure 4. 10 An Idealized Plate Under Lateral Pressure. 95
Figure 4. 11 Rigid Plastic Deformation and Elasto-plastic Deformation 96
Figure 4. 12 Illustration of Three Possible Failure Patterns. 97
Figure 4. 13 Variation of Normalized Pressure at Collapse against β 102
Figure 4. 14 The Normalized Strength of the Plate with Different Loaded Width. 102
Figure 4. 15 Normalized Strength for Different Deflections at Midspan Prior to Failure 103
Figure 4. 16 Deformed panel (H = 0.3 m) 104
Figure 4. 17 Pressure vs. displacement at midspan 104
Figure 4. 18 Strength at various load widths 105
Figure 4. 20 Selected Load Cases 107
Figure 4. 21 Deformed panel, showing contours of principal strains (Case 1) 108
Figure 4. 22 Pressure vs. Displacement at midspan 108
Figure 4. 23 Deformed panel and distributions of principal strain (Case 21) 109
Figure 4. 24 Deformed panel and distributions of principal strain (Case 22) 109
Figure 4. 25 Deformed panel and distributions of principal strain (Case 23) 110
Figure 4. 26 Analysis of design pressure for CAC1 Vessels with r =0.46, n = 10000 112

Figure 5. 1 Probability of the Number of Critical Zones on a 0.72 m^2 Panel 116
Figure 5. 2 Probability Density of Critical Zonal Area (from Approach A of Chapter 3) 117
Figure 5. 3 Zonal Forces vs. Zonal Area (from Approach A of Chapter 3) 117
Figure 5. 4 A panel loaded by one critical zone 119

Figure 5. 5 The case with one critical zone 120
Figure 5. 6 Analysis of the effect of the length of critical zone, h 122
Figure 5. 7 Analysis of the effect of the location of critical zones 122
Figure 5. 8 Relative locations between Critical Zones 126
Figure 5. 9 Cases with two or more critical zones 127
Figure 5. 10 Effect of $\bar{h}$ (the analysis is supported by the previous analysis of h) 129
Figure 5. 11 Analysis on the effect of interaction between critical zones. 129
Figure 5. 12 Analysis of CASE C 132
Figure 5. 13 Schematic Diagram of a Beam Loaded by multiple Point loads 133
Figure 5. 14 Three Hinge Mechanism 134
Figure 5. 15 Schematic View of Membrane Action of a Beam Loaded with point Loads 135
Figure 5. 16 Beam under Different Loading Conditions, (a) Beam Loaded by Uniform Point Loads, (b) Beam Loaded by Tent Shape Point Loads, (c) Beam Loaded by A Single Point Load 138
Figure 5. 17 Different load cases 138
Figure 5. 18 Variation of the location of a critical zone 141
Figure 5. 19 A randomly chosen load case 141
Figure 5. 20 A Scheme of Monte Carlo Simulations 143
Figure 5. 21 Model Uncertainty for Plastic Collapse 144
Figure 5. 22 Model Uncertainty for Ultimate Rupture 144

Figure 6. 1 Analysis of a Design Decision 148
Figure 6. 2 Comparison of Failure Probabilities a) A Safe Structure, b) An Unsafe Structure, and c) An Over-designed Structure 151
Figure 6. 3 Schematic View of the Process of Optimal Design of Structure 152
Figure 6. 4 Load-Resistance Problem 154
Figure 6. 5 Schematic illustration of different rules of specifying the load. 158
Figure 6. 6 Three classes of loads (Maes, 1986) 158
Figure 6. 7 Relationship between Safety Factors and Exceedance Probability 160

Figure 6. 8 Probability of Failure for Different Plate Thickness 167
Figure 6. 9 Plate Thickness for Different Design Strategies 169
Figure 6. 10 Probability of Failure (ultimate Rupture) 170
Figure 6. 11 Probability of Failure (Three hinge Failure) 170

List of Tables

Table 3. 1 Area assigned for each pressure sensor 57

Table 3. 2 Mean zonal Area and the Spatial Density 60

Table 3. 3 Parameters of exponential distribution of critical zonal force 60

Table 4. 1 Particulars of the plate beam 92

Table 4. 2 β values for different cases. 97

Table 5. 1 Results of finite element analysis for Cases 1 to 20 123

Table 5. 2 Results of finite element analysis for Cases 21 to 39 130

Table 5. 3 The Mean Pressure at Three Hinge Collapse for Different Load Type 137

Table 5. 4 Comparison of Point Load Model with the Approximate Solutions 138

Table 5. 5 Results for Cases d, e and f 139

Table 5. 6 Probability Density Functions for Model Uncertainty (lognormal) 142

Table 6. 1 Principal Particulars of the Vessel 148

Table 6. 2 Plate Thickness for Different Class Ships 167

Nomenclature

A_H	zone with high pressure
A_L	region with low pressure
A_0	spalled region
a	design area (m^2)
B	uncertainty in design model of the structure
cdf	cumulative probability function
COV	coefficient of variance
D_N	damage due to microcracking
E	Young's modules (MPa)
f_{3h}^{h}, f_u^{h}	factor of lateral support for plastic collapse and ultimate rupture, respectively
$f_{3h}^{\Lambda}, f_u^{\Lambda}$	factor of location for plastic collapse and ultimate rupture, respectively
f_{3h}^{ξ}, f_u^{ξ}	factor of interaction support for plastic collapse and ultimate rupture, respectively
$F_Z(z)$	cumulative probability of Z
G	Strain Energy Release rate (J/m^2)
h	length of the critical zone (m)
K_I	stress intensity factor for mode I (tensile) fracture (MPa $m^{1/2}$)
K_{IC}	fracture toughness (MPa $m^{1/2}$)
K_{II}	stress intensity factor for mode II (shear) fracture (MPa $m^{1/2}$)
L	load

M	bending moment (N.m)
M_p	plastic bending moment (N.m)
n	number of rams per year
P_{2H}	pressure at 2-Hinge collapse (MPa)
P_{3H}	pressure at 3-Hinge collapse (MPa)
p_e	probability of exceedance
p_u	pressure at ultimate rupture (MPa)
r	proportion of hits
R	resistance of the structure
R^d	resistance from the design model
r_s	specified resistance
s	frame spacing (m)
S	damage parameter defined in Shaperay's theory.
t	plate thickness (m)
U_T	total energy of the system
x_d	design load
x_s	specified load
Z	the maximum of a set of random quantities
α	dispersion of double an exponential distribution
α	load factor (Chapter 6)
β	material factor

δ_{max}	deflection at midspan
ϕ	aspect ratio of a panel
λt	expected number of events
Λ	parameter of location
μ, $E(X)$	mean of X
ν	Poisson's ratio
θ	direction of fracture propagation (rad.)
ρ	spatial density of critical zones (zones/m^2)
σ_y	yield stress (MPa)
σ_y^*	$(\sigma_y+\sigma_u)/2$
σ_u	ultimate strength (MPa)
σ, $VAR(X)$	Variance of X
ξ	parameter for interaction between critical zones

Chapter 1

Introduction

1.1 Overview

The hull of a ship is exposed to different environmental forces during its lifetime. These forces include hydrostatic loads, wave loads, wind loads and ice impact loads. The load during interaction with ice is a major consideration for the design of ships in arctic and subarctic waters. Considerable forces due to ice impact may result when an arctic class vessel strikes multi-year ice or ice island fragments, or when a subarctic vessel strikes an undetected growler or bergy bit. For a designer or an engineer, choosing a design ice load has always been a challenge because of the uncertainties of ice loads in nature. These uncertainties are partially due to the varying ice conditions and the complicated nature of ice-structure interaction process.

From the view point of mechanics, ice-structure and ice-vessel interaction (except at very low rates) is characterized by ice fracture and ice damage processes. The fracture usually initiates from flaws and irregularities in the ice and results in discrete pieces of ice spalling off. Consequently, the contact area between ice and structure is reduced and the pressure on the ice-structure interface is redistributed. In addition, the stress within the ice mass is redistributed, which causes additional spalls. The pressure in the reduced contact areas, especially towards the center, is very high and the ice is subjected to severe damage.

These high pressure regions (termed critical zones) correspond to the areas on the structure where localized ice loads occur. The critical zones are important in the estimation of ice loads and structural design and are the focus of the present research.

The fracture trajectories dictate sizes and geometry of spalled ice pieces and therefore govern the formation, number, sizes and intensities of critical zones. Fracture is random in nature due to the randomness of flaws and irregularities in ice. As a consequence, critical zones are also random. It has been observed from the ship ramming trials (e.g. Glen and Blount, 1984) and in medium scale indentation tests (e.g. Frederking et al., 1990) that high pressure zones constantly disappear and reappear, move from one place to another and change in intensity. The randomness of ice load and critical zones can be accounted for by a probabilistic analysis. Usually, the probability distribution of ice load can be derived from measurements of field tests and ship ramming trials. Such a distribution can then be used in the determination of the design ice load or the design resistance for the structure.

The structure of a ship's hull is a complex combination of plating, stiffeners and supporting frames. In practice, the strength of the ship structure is divided into three components. These are primary, secondary and tertiary (Paulling, 1988). The primary, or global, strength is associated with the hull girder. Loads affecting the hull girder are generally global impact loads. The secondary, or semi-local strength is concerned with the strength of a large plate panel (or grillage). The tertiary, or local, strength is concerned with the strength of plating between two stiffeners or two frames. This region must resist

localized ice loads, especially the critical zones that result from the ice failure mechanism. This region is the focus of the present study.

For a rule based design for ice, such as the Proposals for Arctic Shipping Pollution Prevention Regulations (*the ASPPR Proposals*, Melville Shipping Ltd., 1989), the plating is usually treated as a long plate, loaded by uniform lateral pressure. The plate may fail in one of three limit states, e.g. the three-hinge collapse, permanent set and ultimate rupture. The three-hinge collapse and permanent-set are usually associated with serviceability whereas ultimate rupture is concerned with safety. The long plate model is easy to implement. In reality, the ice loads on a plate are more complicated than the idealized uniform load. Critical zones moves from place to place, and change in intensity. Depending on the exact distribution of the load, the response of the plate could be quite different from one case to another. This results in an uncertainty in the design model of the structure.

The strength of a structure is also random. This is because of uncertainties related to structural size and material strength. As was learned from the review and verification of *The ASPPR Proposals* by Memorial University of Newfoundland (Carter et al. 1992), the ship structural strength might be affected by uncertainties in plate thickness, material strength, weld effect and heat-affected zones.

An optimal design of the structure should account for all uncertainties associated with the environmental loads and design model. Such a design can be viewed as a decision process. The designer must give due consideration to two conflicting objectives, i.e. safety and economy. Theoretically, there is no absolutely safe structure because of uncertainties of environmental load and structural resistance. The safety level of a structure can

be evaluated by the probability of structural survival. This probability can be obtained from the probability densities of the load and resistance. An optimal structure should have a probability of failure close to a target value which is accepted by the engineering practice. There are two methods in structural design, namely reliability method and code design method. For the first, the structural strength is selected based on the target reliability. In the second, the structure is designed according to a design rule. The rule has an intrinsic safety margin accepted by the profession. New rules are also calibrated by reliability analysis.

1.2 Scope of the Work

Mechanics of ice-structure interaction, statistics of ice loads and reliability analysis of structural strength are three important and interlinked aspects for the design of a structure. The proposed research presents an approach which integrates all three aspects. The focus of the research is critical zones (localized high pressure regions which are the key elements of ice loads). I will investigate how they form and how they affect the overall ice loads and the response of the structure.

First, I will investigate the ice-structure interaction process from the view point of mechanics. I will investigate existing fracture models and their applicability to the problems of spalling and formation of critical zones. I will investigate the propagation of small cracks in different stress zones within an ice sheet. I will also investigate the fracture damage interplay process by a numerical example.

Second, we propose a probabilistic approach to the estimation of ice loads. Extremal analysis and its application in evaluating design ice load is first discussed. Critical zones are quantified by parameters such as their spatial density, sizes and intensities. These parameters are calibrated using the ship ramming trial data of Louis St. Laurent. A probabilistic model of critical zones is proposed; which assumes that the ice load on a design area is applied through a random number of critical zones, each with a random force. This model is then used in deriving the probability distribution of extremal ice loads.

Third, we will investigate the strength of the structure. We will focus our analysis on the ship plating. The long plate model, which is used in practical design, will be reviewed and different failure mechansims will be investigated. The response of a plate to various realistic loads will be analyzed using a finite element method. A long plate model, which accounts for the non-uniform loads, will be developed. This model, together with the results from the finite element modelling of various load scenarios, will be used to analyze the uncertainty of the design model of the structure.

Finally, we will discuss the principles of design. These include a discussion on different design methods in practice and rationale in selecting the design loads and resistance. The principles are applied for the design of plating of a tanker for offshore Newfoundland waters. Plate thickness according to different design strategies are derived and the probability of failure for each design is evaluated.

Chapter 2

Ice-Structure Interaction Process

2.1 Introduction

Ice-structure and ice-vessel interaction (except at very low rates) is characterized by ice fracture and damage processes. The fracture usually occurs near the free edge bordering the actual contact area between the ice and the structure. Such fractures result in large pieces of ice spalling off and a reduction in the remaining contact areas. The pressure in these contact areas is very high, especially towards the center. The areas have been termed **critical zones**. Extensive damage to ice usually takes place in these zones. There is evidence that ice has been microfractured, broken into small pieces, subjected to pressure melting and sintered together in these zones (Jordaan, Xiao and Zou, 1993). These zones also carry most of the ice load and are crucial to the modelling of the global scale effect and to the analysis of local pressure. Spalling by fracture governs the variation of size, number and location of these zones during the interaction process. Figure 2.1 schematically illustrates an interaction with one critical zone and spalls.

Spalling by fracture has been analyzed, using finite element modelling, by Xiao and Jordaan (1991) in terms of the propagation of a flaw located near the ice-structure

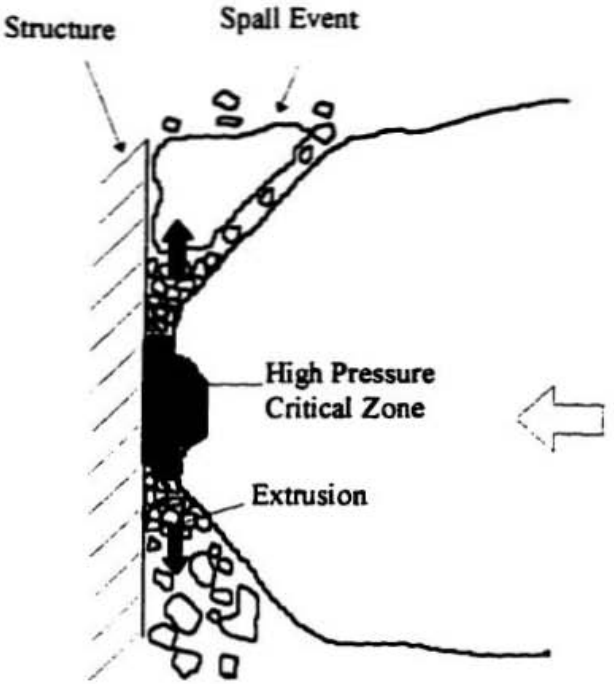

Figure 2. 1 Schematic Illustration of A Critical Zone with Spalls

interface. They found that the crack would propagate at loads about one tenth of those calculated using damage analysis only and that the propagation would result in a piece of ice spalling off and a reduction of ice force. Furthermore, they found that flaws propagate more readily in zones of low confining pressure. These zones are located near the free surface of the ice where spalls are often observed. A flaw may propagate in a tensile mode, a shear mode or a mixed mode. They also found that the tensile zones near the free edge of an ice sheet are often small. Zones with high shear stress tend to be larger, with a higher probability of containing a flaw. Fracture is unlikely to be initiated from cracks under high confining pressure.

Evans et al. (1984) proposed a semi-quantitative model for the spalling of edge-loaded ice sheets. The model was based on the plain-strain cavity expansion theory (Hill, 1950) and elastic plate bending theory. It confirmed that the forces required to propagate spall cracks are relatively small but the authors experienced difficulties in calibrating the parameters in the model by experiments.

Critical zones and spalls are random in nature. This has been demonstrated in medium scale indentation tests (i.e. Frederking et al. 1990) and ship trials (i.e. Glen and Blount 1984), where high pressure areas constantly disappear and reappear, move from one place to another, changing in intensity. The probabilistic nature of critical zones and spalls is associated with the randomness of flaws in ice, which lead to the initiation of spalling. Similar to other materials, ice contains many defects such as cracks, inclusions, pores, grain boundaries and other weakness. Both the size and the location of these are generally random. For this reason, a probabilistic analysis of existing flaws is needed. A probabilistic model has been proposed by Maes et al. (1986), by assuming that the cracks are randomly dispersed in a material volume according to a Poisson process. On the other hand, Kendall (1978) referred to the probabilistic approach as "dubious statistical arguments involving invisible flaws". He proposed a deterministic model, well known as "the double cantilever beam", which assumes that a centrally located crack divides a beam into two cantilevers and that the resulting bending moment on each cantilever results in crack growth. It has been found by Zou et al. (1996) that the basic assumption in Kendall's model, that is, treating two struts as elastic beam, is only valid for large crack lengths (ie. The thickness of an ice sheet). Cracks of such length and of such location can be rarely

be rarely found in nature. Although long central cracks have been observed in some indentation tests (Kārnā and Muhonen 1990), they are more likely formed as a result of the propagation of small cracks rather than being present as initial flaws. In addition, DeFranco and Dempsey (1990) found that the boundary condition in Kendall's model is not well defined, which may result in the fracture force estimated being close to one third of the real value. Therefore, the replacement of "invisible flaws" (for example grain boundaries) by a precisely located yet also invisible central crack is a questionable alternative, which will be investigated in detail in this section. In addition, a deterministic analysis of the propagation of cracks, with different lengths and located in different regions with different stress conditions, will be analyzed. Finally we will review some basic aspect of damage mechanics and the fracture damage interplay during the ice-structure interaction process. We begin our analysis from some basic aspects of ice fracture mechanics.

2.2 Ice Fracture

As described in Section 2.1, fracture of ice usually initiates from a flaw in the ice. According to linear elastic fracture mechanics (LEFM), a crack will begin to propagate when the stress intensity factor at the crack tip exceeds the fracture toughness. An equivalent criterion of stress intensity factor is strain energy release rate. The fracture toughness of fresh water ice ranges from 0.1 to 0.14 $MPa\ m^{1/2}$ and the corresponding critical strain energy release rate ranges from 1 to 2 J/m^2 (Timco and Frederking, 1986; Dempsey et al., 1989).

Once the fracture is initiated, its subsequent propagation depends on its stability. If the fracture continues to propagate, then the crack is unstable. If additional force is needed for continual crack growth, the crack is stable. The stability of a crack can be analyzed by the change of strain energy release rate G with respect to crack length a, $\frac{\partial G}{\partial a}$. The crack is unstable when the ratio is greater than zero. In an ice-structure interaction, an unstable crack may propagate into a compressive zone and become stable and not cause any catastrophic failure.

As already discussed in Section 2.1, a crack may propagate in a tensile mode, a shear mode or a mixed mode. The mixed mode fracture has been studied extensively, e.g., by Sih (1973), Palaniswamy and Knauss (1974), Conrad (1976), Cotterell and Rice (1980), Sih and Tzou (1983), Hutchinson and Suo (1992). There are three principal theories: first, that the crack will propagate at right angles to the maximum tensile stress, second, that it will propagate in the direction which corresponds to the maximum strain energy release rate (SERR), and third, the crack direction is that which corresponds to the strain energy density. The most fundamental of these is judged to be the maximum SERR. Indeed, Conrad (1976) quotes from Griffith: "the crack will grow in the direction along which the elastic energy release per unit crack extension will be the maximum and the crack will start to grow when this energy reaches to a critical value". For practical purposes, there is little difference between the first and the second criteria. This agrees with the results of Hutchinson and Suo (1992) who found no distinction between a criterion for crack kinking based on maximizing strain energy release rate or based on propa-

propagation in the direction in which $K_{II} = 0$. Figure 2.2 shows that the angle of crack propagation corresponds to the maximum SERR with respect to the ratio of K_I/K_{II}, where K_I and K_{II} are stress intensity factors of tensile and shear mode respectively. Figure 2.3 shows critical values of K_I and K_{II} at which the maximum SERR at the direction of crack propagation reaches the material fracture toughness. Values of K_I and K_{II} are normalized with K_{IC} and plotted together with the results of mixed mode fracture tests on ice by Shen and Lin (1986). The closed form formulae of the relationships in Figure 2.2 and 2.3 are derived and given below for the convenience of analysis:

$$\frac{K_{II}}{K_{IC}} = [-0.007373(\frac{K_I}{K_{IC}})^2 - 0.6642\frac{K_I}{K_{IC}} + 0.671]^{1/2} \ , \tag{2.1}$$

$$-\theta = \exp[-0.00003318(\frac{K_I}{K_{II}})^3 + 0.01665(\frac{K_I}{K_{II}})^2 - 0.3191\frac{K_I}{K_{II}} + 4.3097] \ . \tag{2.2}$$

A crack may also propagate when the crack tip is under a shear stress and a confining pressure. The propagation in this case is more difficult than for the case of mixed mode tensile and shear cracks as indicated by the studies of Hallam (1986), Kachanov, (1993) and by Smith and Schulson (1991).

2.3 *Analysis of Kendall's Double Cantilever Beam Theory*

Kendall's double cantilever beam is shown in Figure 2.4. The beam is fixed at one end and free at the other. A centrally located crack at the free end divides the beam into two struts. A punch at the free end causes the struts to 'bend and shear outward'.

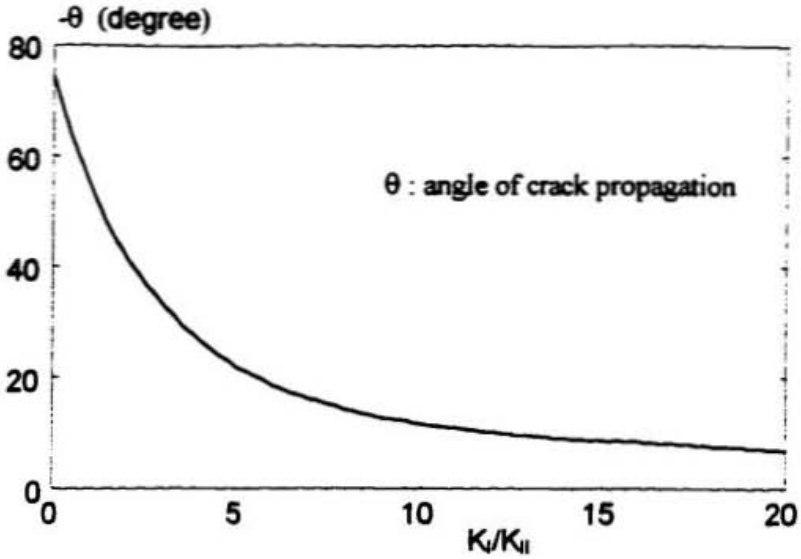

Figure 2. 2 Angle of Crack Propagation (Palaniswamy and Knauss, 1974)

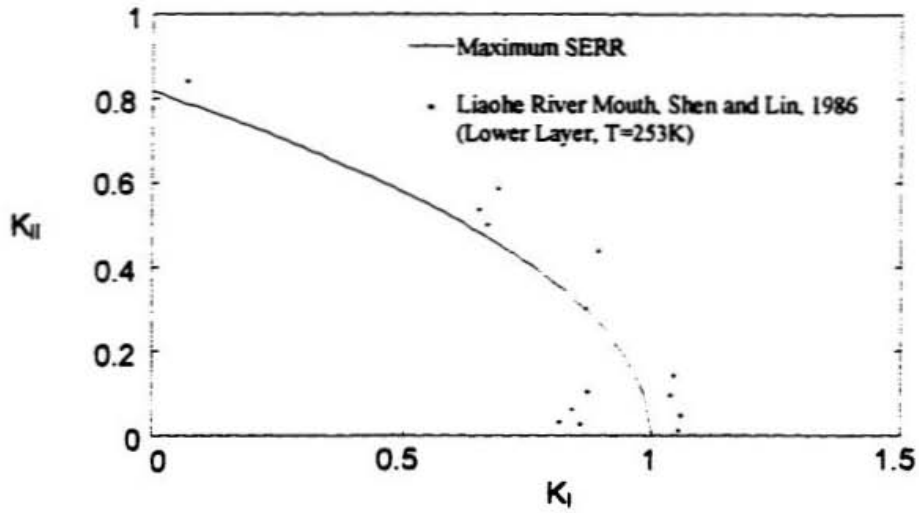

Figure 2. 3 Data of Shen and Lin (1986) Fitted to the Maximum SERR Analysis of Palaniswamy and Knauss (1974). Data Normalized with K_I=0.107 MPa $m^{1/2}$

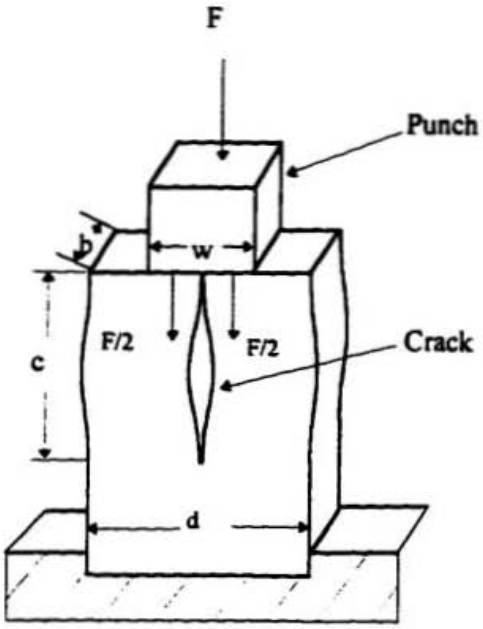

Figure 2. 4 Kendall's double cantilever beam

Kendall simplified the force of the punch as two concentrated forces on the free end (see Figure 2.4).

According to the law of energy conservation, the total strain energy of the system (U_T) does not change with the crack length c for a stable crack growth.

$$dU / dc = 0 \tag{2.3}$$

The strain energy due to the punch has two major components: compression, corresponding to forces $F/2$ applied along the axes of the struts, and a bending moment caused by the eccentricity of the force $F/2$. The compressive component is assumed not to

change with the crack length and therefore disappears from equation (2.3) The bending component for the simple beam geometry can be derived as:

$$U_b = \frac{3}{2} F^2 (d-w)^2 c / Ebd^3 \tag{2.4}$$

and the total energy of the system (excluding the compressive component) is given by:

$$U_T = -\frac{3}{2} F^2 (d-w)^2 c / Ebd^3 + Rbc \tag{2.5}$$

where R is the surface energy. Applying the above equation to equation (2.3) Kendall derived the fracture driving force for a stable crack propagation:

$$F = \frac{b}{(1-w/d)} \left(\frac{2}{3} ERd\right)^{\frac{1}{2}} \tag{2.6}$$

With the same principle described above, Kendall also derived the force required to propagate a crack which is not located at the center of the beam (see Figure 2.5a) result shows that the force required to propagate the crack is minimum when the crack is located at the center (see Figure 2.5b). Hence he concluded that "there will be a preference for cracks to travel on the central plane".

Some of Kendall's assumptions are now discussed. First, in Kendall's model, there is no lateral restraint on the free end of the struts. This means that the struts are free to run into each other as shown in Figure 2.6, which does not correspond to the intended idealization in Figure 2.4. In reality, there is a reaction on the end of each strut causing an

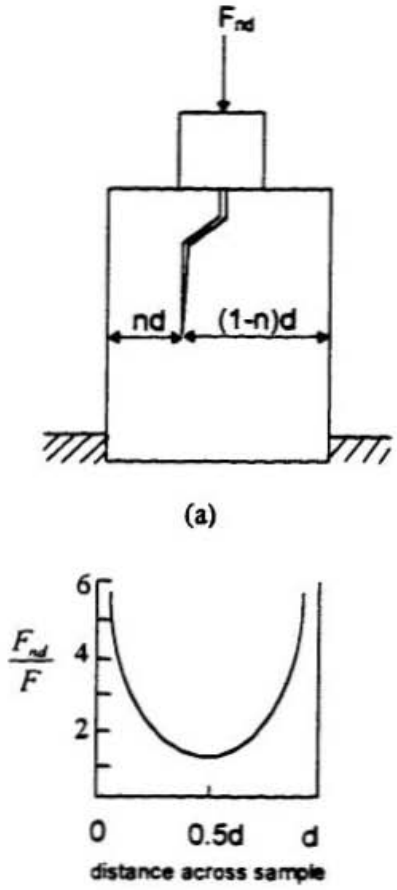

Figure 2. 5 Kendall's model for the crack off the center line (from Kendall 1978)

additional bending on the beam. Assuming that the 'free ends' are completely restrained, DeFranco and Dempsey (1990) derived the value of fracture driving force:

$$F = \frac{b}{(1 - w/d)} \left(\frac{16}{3} ERd\right)^{\frac{1}{2}} , \tag{2.7}$$

Figure 2. 6 Struts with no constrains at free ends

which is close to three times the value in Kendall's theory (see Figure 2.7). In a practical case, the end condition may be between free and completely restrained depending on the conditions of the interface, which, for the ice-structure interaction, may involve friction, pressure melting and sintering. Second, the simplification of the deflection of the struts as pure bending is not appropriate for the case of small crack lengths. In this case compressive stress is not a constant throughout the beam, especially in the region near the indentor where compressive stress dominates. In fact this high compressive stress may cause the crack to close when the crack is very short. To demonstrate this, the following numerical analysis on a double cantilever beam is carried out using a finite element modelling package ABAQUS.

Figure 2.8 shows an ice beam with a central crack at the free end, subjected to an indentor of one meter width. The indentation speed in this case is assumed high enough so that ice can be treated as an elastic material.

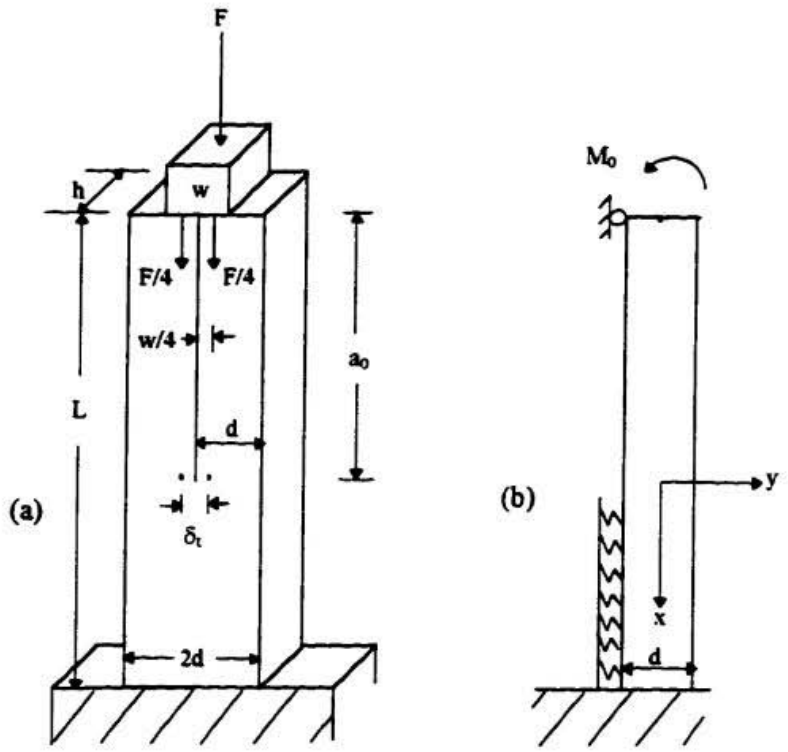

Figure 2. 7 Double Cantilever Beam with restrained ends from DeFranco and Dempsey (1990)

The simplification of indentor force as two concentrated forces in Kendall's theory is not accurate for the analysis of small crack lengths and is not applied here. For the ice-structure interaction, the pressure distribution on the interface is complicated. A damage analysis by Xiao and Jordaan (1996) shows that the distribution is an inverse parabola in shape when ice is initially in an elastic contact, then it changes to a uniform and a parabolic shape as the ice damages near the interface. The distribution is further complicated by spalls and the formation of critical zones. For the purpose of comparison, a uniform pressure distribution is used in this analysis. Values of strain energy release rate

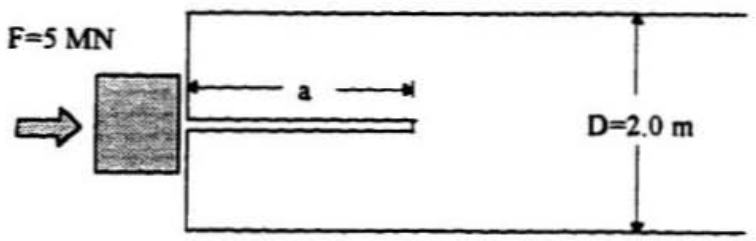

Figure 2. 8 An ice sheet with a central crack, loaded by an indentor

G at crack tips of different crack lengths were evaluated. The crack will propagate when G reaches a critical value G_c. The value of G_c for ice is in the range of 1~2 J/m^2 (Timco and Frederking (1986). In this study a value of G_c as 1 J/m^2 is used. The results are presented in Figure 2.9 (a) together with values obtained from Kendall's theory and DeFranco and Dempsey (1990), where the crack length is presented in a non-dimensional form with respect to the ice thickness a/D. Figure 2.9 (a) shows that G increases with crack length. The rate of increase diminishes when the crack length a/D is 0.8 and G gradually reaches a constant value which corresponds to a stable crack growth. The constant is close to the value predicted by DeFranco and Dempsey (1990) and one eighth of the value in Kendall's theory. A more detailed plot (Figure 2.9 (b)) shows that G is equal to zero for crack lengths a/D less than 0.22. This is in agreement with the stress analysis which shows that the crack tip is under high compressive stress. Figure 2.9 (b) also shows that G reaches G_c when the crack length a/D is 0.3, which corresponds to a 60 cm crack in a 2 meter thick ice sheet. This is a long flaw and is unlikely to be found.

Thirdly, the extension of the centrally located crack model to the non-central located crack model presents difficulties. This is because in the first case the shear strain energy component is not considered, which may be predominant in the second case. To investigate this further, the same double cantilever beam is analyzed with the crack located in different lateral positions (see Figure 2.10). The crack length is fixed as 0.5 *m* and values of G of crack at different locations were evaluated. The results are presented in Figure 2.11 together with Kendall's prediction. The results show that G increases when the crack is off the central plane in contrast to the Kendall's conclusion.

In conclusion, Kendall's model is only valid for long cracks. The model as modified by DeFranco and Dempsey (1990) gives a good prediction of G for large crack lengths. The extension of the model with a centrally located crack to one with a non-centrally located crack presents difficulties. The double cantilever beam theory has been applied to the analysis of ice spalling by a number of researchers. The application may be suitable for the analysis of a large splitting ice feature but not suitable for the analysis of ice spalling, since in a real field situation spalling may result from the propagation of cracks of various locations. An alternative beam model was proposed by Hutchinson and Suo (1992) which considers a mixed mode crack. This approach may provide a good approximation to ice spalling and is given in next section.

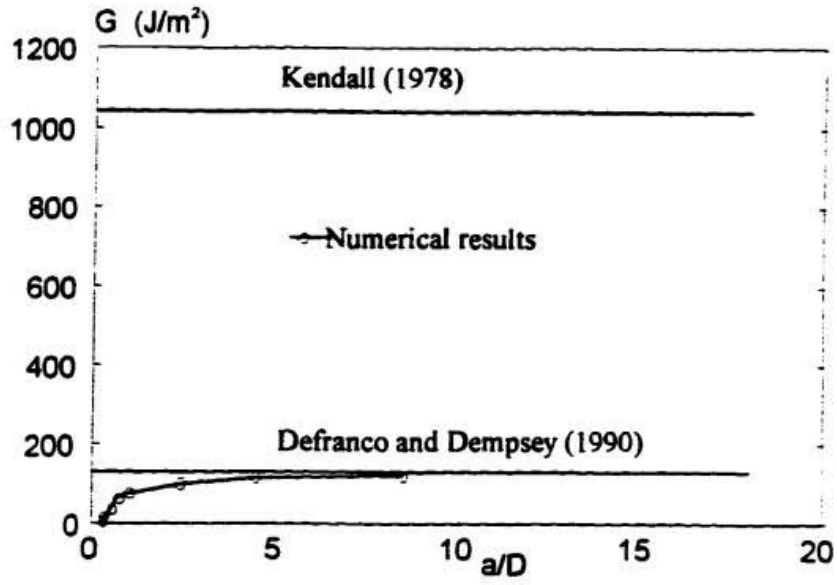

(a)

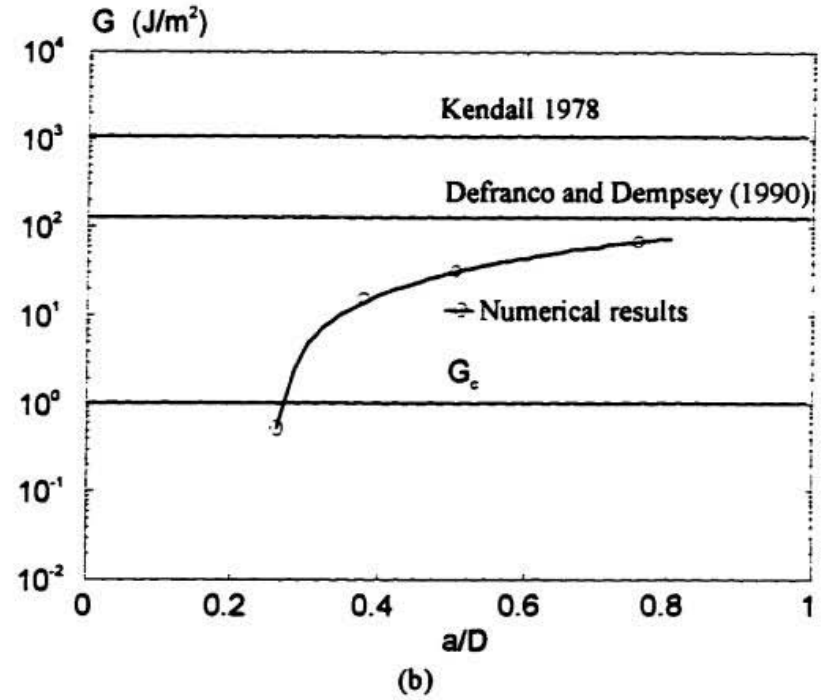

(b)

Figure 2. 9 (a) Results of strain energy release rate, (b) detail of figure (a)

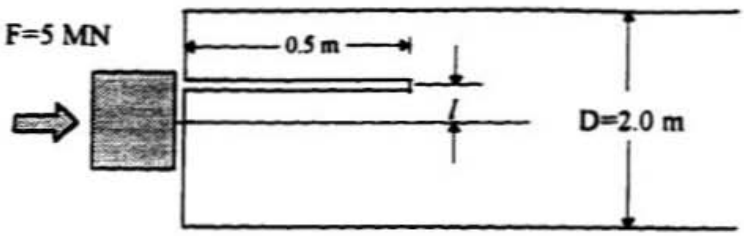

Figure 2. 10 An ice sheet with crack in different vertical locations

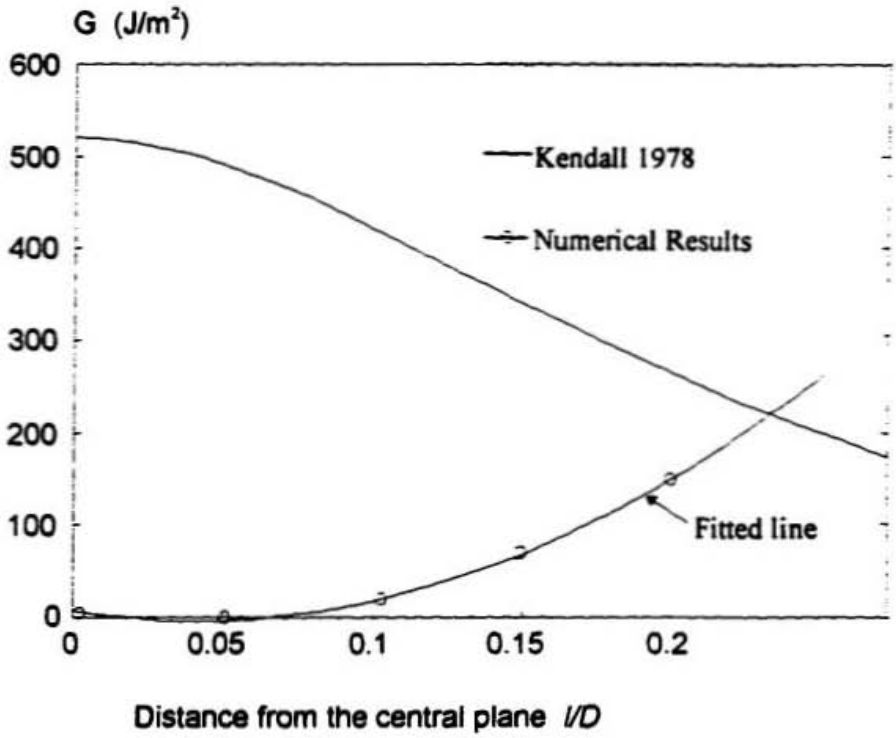

Figure 2. 11 G values for cracks at different locations

2.4 Analysis of Beam Model By Hutchinson and Suo

Hutchinson and Suo (1992) described a beam model originally developed by Suo (1990), which is similar to that of Kendall but includes the effect of compressive stress (see Figure 12). The strain energy release rate at the crack tip, G, was derived as:

$$G = \frac{1}{2\overline{E}}\left[\frac{P_1^2}{h} + 12\frac{M_1^2}{h^3} + \frac{P_2^2}{H} + 12\frac{M_2^2}{H^3} - \frac{P_3^2}{h+H} + 12\frac{M_3^2}{(h+H)^3}\right] \tag{2.8}$$

where $\overline{E}$ is the effective Young's modules, P_1, P_2, P_3, M_1, M_2, M_3, h and H are defined in Figure 2.12.

The strain energy release rate in Equation (2.8) was further separated into opening and shearing components by Hutchinson and Suo (1992) using linearity and dimensionality. Consequently, the stress intensity factors take the form:

$$\begin{aligned} K_I &= \frac{P}{\sqrt{2hU}}\cos\omega + \frac{M}{\sqrt{2h^3V}}\sin(\omega+\gamma), \\ K_{II} &= \frac{P}{\sqrt{2hU}}\sin\omega + \frac{M}{\sqrt{2h^3V}}\cos(\omega+\gamma), \end{aligned} \tag{2.9}$$

where P and M are linear combinations of the applied loads:

$$P = P_1 - C_1P_3 - C_2M_3/h, \quad M = M_1 - C_3M_3, \tag{2.10}$$

$$C_1 = \frac{1}{1/\eta+1}, \quad C_2 = \frac{6/\eta}{(1/\eta+1)^3}, \quad C_3 = \frac{1}{(1/\eta+1)^3}, \quad \eta = h/H; \tag{2.11}$$

and U, V and γ are geometric factors described as below:

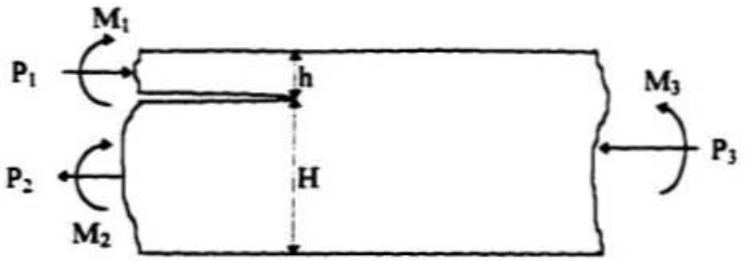

Figure 2. 12 A Beam Model by Suo (1990)

$$\frac{1}{U} = 1 + 4\eta + 6\eta^2 + 3\eta^3, \quad \frac{1}{V} = 12(1 + \eta^3), \quad \frac{\sin\gamma}{\sqrt{UV}} = 6\eta^2(1 + \eta). \tag{2.12}$$

Accurate determination of ω of Equation (2.9) is very complicated. The elasticity problem was solved rigorously with the help of numerical solutions of an integral equation by Hutchinson and Suo and the results are presented in an approximate formula:

$$\omega = 52.1^{\circ} - 3^{\circ}\eta. \tag{2.13}$$

Further, Hutchinson and Suo presented a criterion for mixed mode crack propagation by:

$$G_{cn} = \overline{F}(\psi, \xi = 0)\Gamma \tag{2.14}$$

where G_{cn} is the critical energy release rate, $\overline{F}$ is the factor depending on the ratio of K_I to K_{II}. In Equation (2.14), ψ is the direction of crack propagation, ξ is a parameter related to traction at crack tip and Γ is the fracture toughness. $\overline{F}$ in Equation (2.14) is equal or less than 1, which means the mixed mode crack will propagate at an "apparent strain en-

energy release rate" less than the fracture toughness. This is in agreement with the results of Palaniswamy and Knauss (1974).

The preceding approach by Hutchinson and Suo provides a better treatment of beam than Kendall by accounting for the compressive component of the strain energy. In the following, we will use this model to investigate the fracture strength of an ice sheet shown in Figure 2.13. We assume that a long crack exists and is parallel to the ice sheet. The end of the ice sheet is loaded by a patch load with a width of w, and has a parabolic pressure distribution. This patch load is similar to a critical zonal force. We define an equivalent fracture strength of the ice sheet as the mean pressure over the thickness of the ice at which the crack propagate:

$$p_{ef} = \frac{\int_{w} p(x)dx}{D} \quad , \tag{2.15}$$

where $p(x)$ is the pressure distribution corresponding to the propagation of the crack. Tentatively, we assume it has the form:

$$p(x) = p_0(1 - \frac{(x - x_0)^2}{(w/2)^2}) \quad , \tag{2.16}$$

where p_0 is defined in Figure 2.13.

Factors affecting the fracture strength include the position of the crack relative to the center of the ice sheet, l, the width of the patch load, w, and the location of the load x_0, (see Figure 2.13). In the following we analyze these factors.

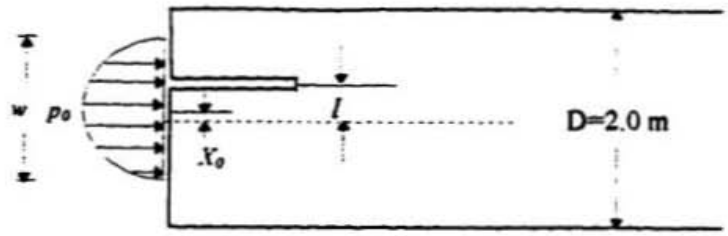

Figure 2. 13 An Idealized Ice-Structure Interaction

To investigate the effect of l, we examine the case when $w = D$, $x_0 = 0$ and l varies between 0 to $D/2$. For each value of l, Equations 2.9 to 2.13 are used to calculate K_I and K_{II} for the case when $p_0 = l$. The amplitude of p_0 which causes crack propagation is then derived based on minimum SERR criterion (Equation (2.1)). The fracture strength is then calculated from Equation (2.15). The results are presented Figure 2.14. The strength is normalized with p_{cf}^0, which is the fracture strength when $l = 0$. Note that the fracture strength is lower when the crack is off the center. This is consistent with the result from our finite element analysis (see Figure 2.11).

Next, we investigate the effect of the width of the loaded area, w. We examine the case when $l = 0$, $x_0 = 0$ and w varies between $0.2D$ to D. The fracture strength for each w is derived from the same method used in analyzing the effect of l. The strength is normalized with respect to p_{cf}^0 and is presented in Figure 2.15. Note that the strength decreases with the load width, implying that the more concentrated loads make the fracture propagation easier.

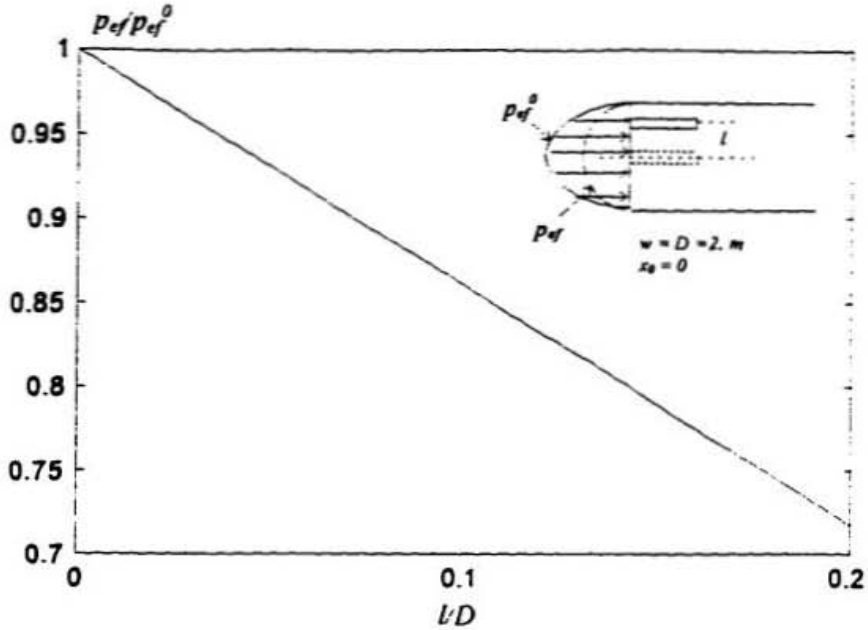

Figure 2. 14 Analysis on the effect of location of the crack

Finally, we examine the effect of x_0. We vary x_0 between 0 to $D/4$ for the case that $w = D/2$, $l = 0$. and we derive that strength from the same method described before. Strength against x_0 are presented in Figure 2.16 in terms of normalized form. Note that the strength decreases with respect to x_0.

Note that in the above analysis we only dealt with some special cases of a complicated combination between l, w and x_0. In reality, this combination could be random, which results in the randomness of the fracture strength. To investigate this, we perform the following Monte Carlo simulations.

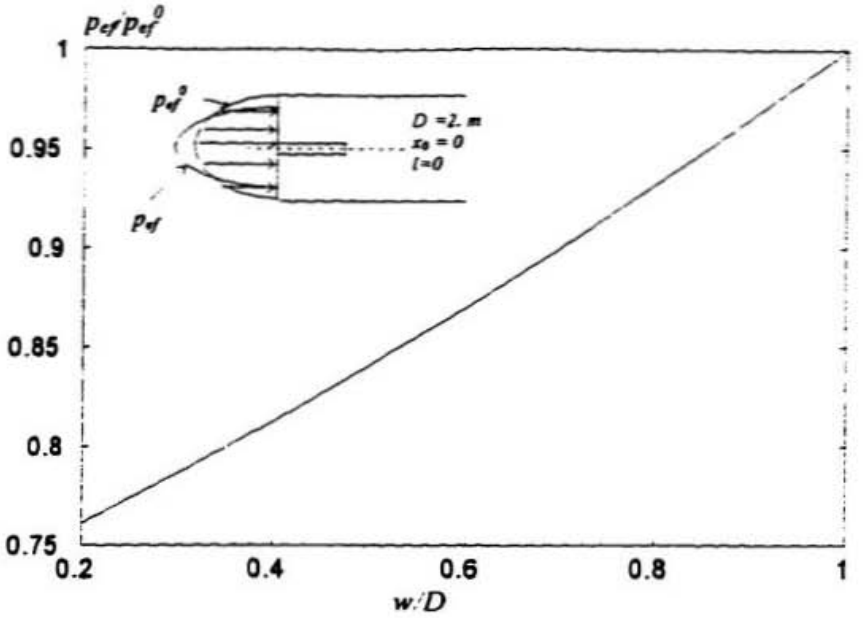

Figure 2. 15 Analysis on effect of w

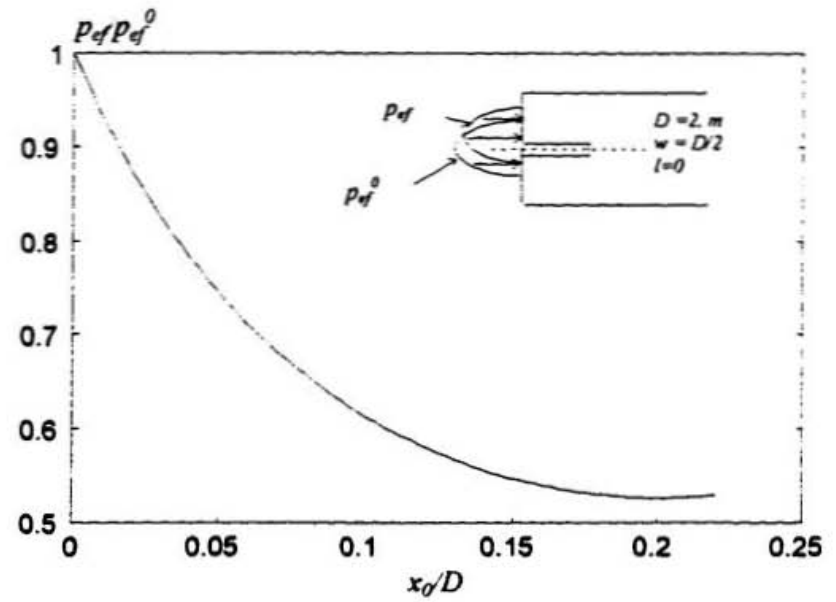

Figure 2. 16: Analysis on the effect of x_0

In each simulation, we randomly select w between 0 and D. Then, we randomly select x_0 between 0 and (D-w). We also randomly choose l between 0 and D/2. For the selected combination of l, w and x_0, we calculate the strength. All these parameters are selected following a uniform distribution. A total of 5000 simulations were performed. The results of p_{ef} are ranked and presented in terms of probability of exceedance in Figure 2.17. The simulated results indicate that p_{ef} is scattered within the range from 165 Pa to 35 MPa with a mean value of 0.2 MPa. The results indicate the fact that ice failure by crack propagation can occur at any load level depending on the load configuration and the location of crack. It should be realized that only fracture failure is considered in the simulation. The ice sheet may fail by other mechanism such as damage.

The preceding analysis shows that an open crack parallel to the ice sheet may propagate at a random load level depending on the location of the crack and the load profile. In reality, the fracture strength of the ice is even more complicated since cracks in nature are usually smaller and their propagation is more complicated. They can be located in a random location with a random orientation. The propagation of these cracks is more difficult to predict. This is illustrated by a deterministic analysis of close form cracks given in the following section.

2.5 *Analysis of Small Cracks at Different Locations*

The large open cracks of Kendall's model are rarely found in ice fields. Instead, small cracks have a high probability to exist. With a favorable location and orientation, these cracks may propagate and result in discrete ice pieces spalling off.

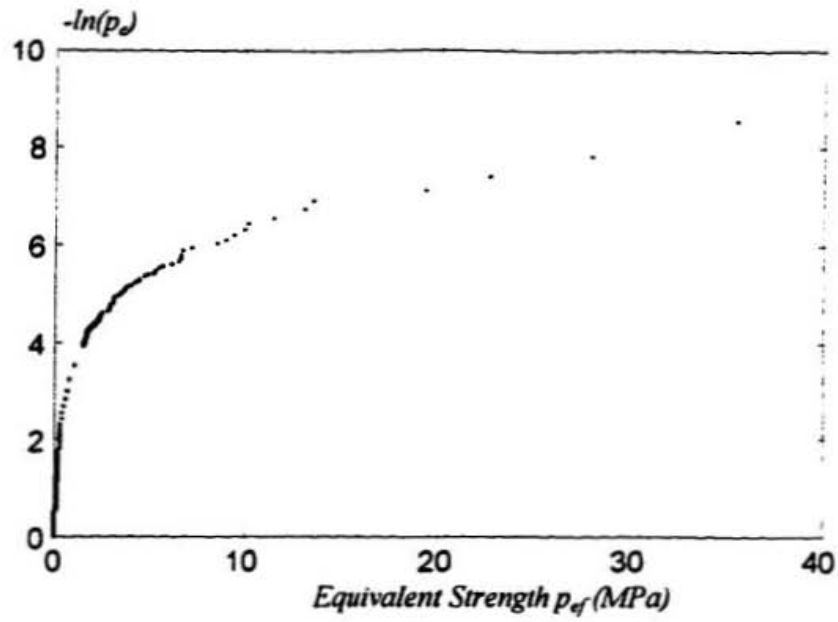

Figure 2. 17 Results of Monte Carlo Simulations

In the following, we shall investigate these cracks at different locations in an ice sheet of two meters thickness loaded by an indentor at its end (see Figure 2.18). The indentor force is assumed to have a parabolic distribution following a damage analysis by Xiao and Jordaan (1991). The interaction rate considered here is high enough that damage to the ice only occurs near the interface and the response of the rest of the ice sheet is assumed elastic.

The stress distribution in the ice sheet has been analyzed. A tensile zone has been found near the center of the ice sheet (see Figure 2.18). The direction of the tensile stress is mainly perpendicular to the ice sheet. This suggests that the cracks parallel (or close to parallel) to the ice sheet are more likely to propagate. Cracks with other orientations may

be subjected to compressive stress and are more difficult to grow. The shear stress parallel to the crack plane will also cause the crack to propagate. Zones of such shear stress parallel to the ice sheet are identified and are plotted in Figure 2.18.

Cracks at three different locations are investigated. The cracks are assumed to be parallel to the ice sheet for simplicity. Cracks of different orientations can be considered later. Cracks at location 1 are mainly subjected to shear stress, cracks at location 2 may cause mixed mode fracture and cracks at location 3 will cause tensile fracture. Values of strain energy release rate have been evaluated for different crack lengths and are plotted in Figure 2.19. The result shows that G increases with crack length. G_{IC} and G_{IIC} are critical strain energy rates for tensile and shear crack modes respectively, which are derived from K_I and K_{II} discussed in Figure 2.3. $G_{IIC} \approx 0.6\, G_{IC}$ is used in this study. A mixed mode crack will propagate with the value of G between G_{IC} and G_{IIC} depending on the ratio of tensile and shear stress intensity factors as discussed earlier. While Figure 2.19 shows that the mixed mode crack at location 2 has the highest G value, it also shows that cracks at all locations can propagate for very small crack lengths. Suggested crack trajectories following Conrad (1976) are also plotted in Figure 2.18. Cracks at location 1 and 2 may result in discrete ice pieces spalling off. Cracks at location 3 will cause splitting of the ice feature. Such a splitting has been reported by Kärnä et al. (1990). It is also noted that depending on the location of the crack, the size of the spalled piece is different; subsequently, the size of critical zones (remaining contact areas) is also different. Since

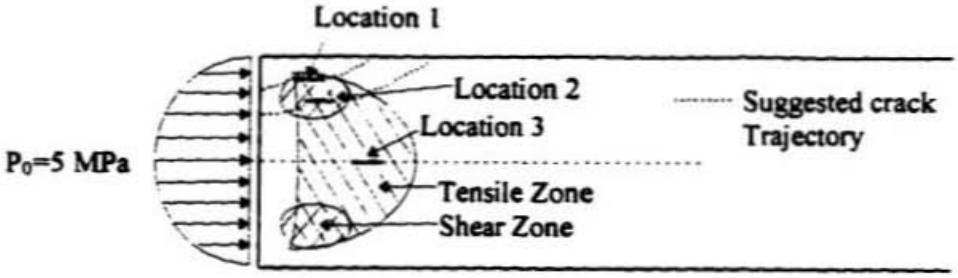

Figure 2. 18 Tensile Stress Zone and Shear stress Zones

the location, sizes and orientations of flaws in nature are random, the trajectories of fracture propagation are also random. This leads to the fact that locations, sizes and intensities of localized high pressure zones are also random.

The preceding example demonstrates how a spall can be initiated from a flaw in an ice sheet. The spall intensifies the pressure in the remaining contact area. The intensified pressure will form a larger shear zone, hence causing subsequent spalling. In the mean time, in the reduced contact area, ice is subjected to highly localized pressure and severe damage. Some basics of ice damage mechanics are described in the next section.

2.6 Ice Damage

As spalling occurs, the remaining contact area is reduced. This will cause the high stress concentration and severe ice damage. Damage mechanics may offer the insight look at the failure process and a method to estimate of the forces on the structure.

Most of the early work on damage mechanics was based on the idea that the damage to a structure can be measured by a scalar factor, which equals either the ratio of the

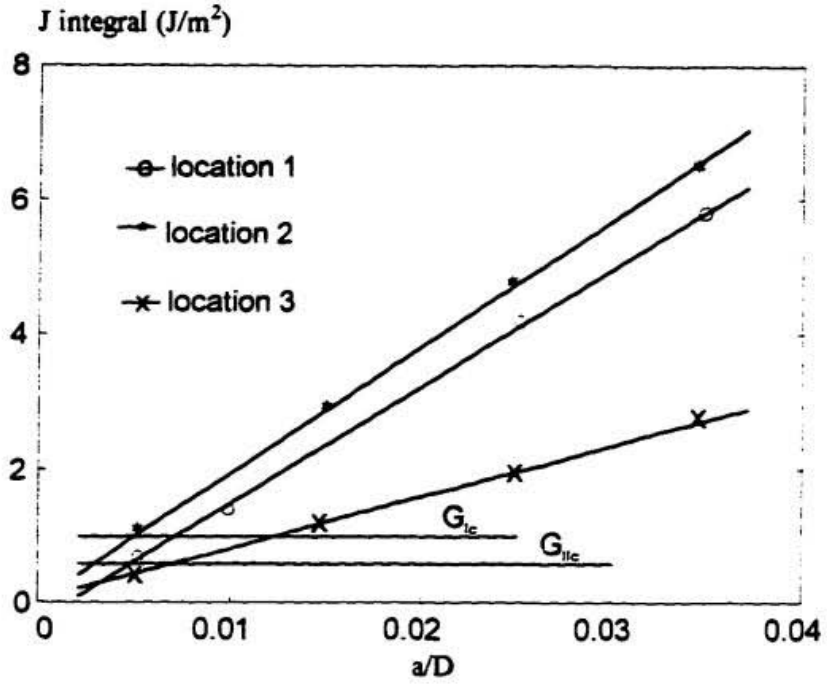

Figure 2. 19 G Values of Different Crack Lengths

area of voids to the whole cross section, or a function of the density of microcracks and voids which would permanently affect either the elastic modulus or shear modules. The importance of this kind of model is the establishment of a rational damage law which defines the rate of damage accumulation in terms of current values of state variables and internal variables.

Damage mechanics has been applied to ice by Jordaan and McKenna (1988), McKenna et al. (1989), Karr and Choi (1989) and others. An isotropic damage model with a single scalar damage parameter has been developed, by Jordaan and McKenna (1988) based on rate theory, and has the form:

$$\dot{N} = \dot{N}_0 (\frac{\sigma - \sigma_c}{\sigma_0})^m \quad \sigma > \sigma_c \ ,$$

$$\dot{N} = 0 \quad \sigma \le \sigma_c \ , \tag{2.17}$$

where σ_c is the threshold stress, σ_0 is a unit stress, m is a constant and $\dot{N}_0$ is a reference rate. The damage, D_N, due to microcracking is defined in the form:

$$D_N = a^3 N \tag{2.18}$$

where a is the radius of crack.

It should be noted here that it is not appropriate to use crack density as the only measure for the damage. For example, in the cases of crushed ice in the critical zones, the crystal structure of intact ice has been broken down to fine grains. Under high confining pressure, the crushed ice may be sintered into a solid but microstructurally modified ice mass due to pressure melting or recrystallization.

The approach taken by Schapery (1981,1991) offers a rigorous solution to a class of problems involving cracking and damaging viscoelastic materials. It includes a proper treatment of energy flux into the crack tip zone, a thin layer of damage material in the re-

region of the crack tip, and damage in the parent material. The damage measure given by Schapery is :

$$S = \int_0^t s^q d\tau \ , \tag{2.19}$$

where q is a constant and S is the damage parameter.

From experiment, especially compressive creep tests, it has been found that the presence of cracks and damage significantly enhances the creep strain. The creep strain of damaged ice is 5 to 10 times that of intact ice. An exponential factor for creep strain rate was introduced to capture the behavior for both low and high crack densities, which has the form: *exp(BS)*, where B is a damage enhancement parameter.

2.7 Fracture and Damage Interplay in Ice-Structure Interaction

As we described in section 2.1, failure of ice during the ice-structure interaction is characterized by fracture and damage process. The fracture usually causes pieces of ice spalling off and the reduction of the contact area. Extensive damage of ice takes place in the reduced area and results in the reduction of the total indentation force. This interplay process plays a key role in the appearing and disappearing of critical zones. Following we illustrate this process by a numerical example given in Jordaan, Xiao and Zou (1993).

In Figure 2.20 (A), an ice sheet 2 m thick is loaded by a rigid indentor at its end at a rate of 100 mm/s. For illustrative purpose, two flaws are assumed to exist in the ice sheet at the locations shown in Figure 2.20 (A). The propagation of these two cracks are

modelled by applying maximum SERR principle and by using finite element package ABAQUS. The propagation of the cracks eventually causes spalls at instant *B* shown in Figure 2.20 (B). The spalls result in the reduction of contact area and pressure redistribution. Figures 2.20 (B) to (F) show the pressure redistribution process within remaining contact area. The pressure in the remaining area is very high initially, and the distribution quickly changes from a reversed parabolic to a parabolic shape. The amplitude of the

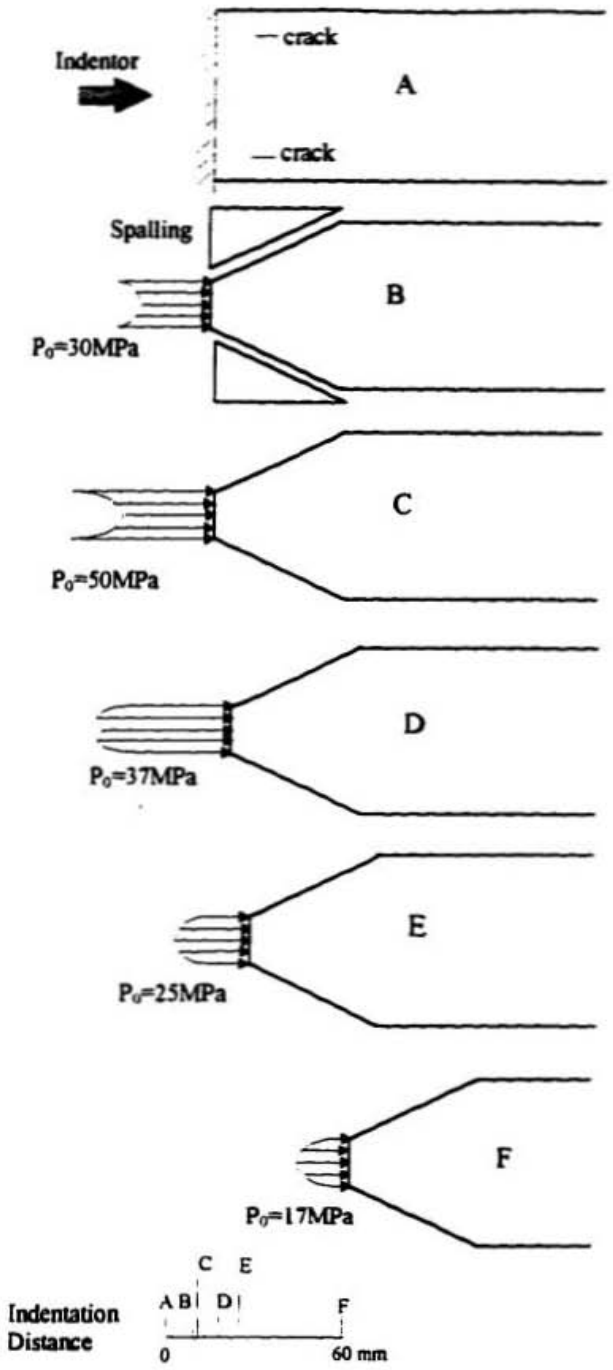

Figure 2. 20 Schematic Illustration of Pressure Variation During the Interaction Process

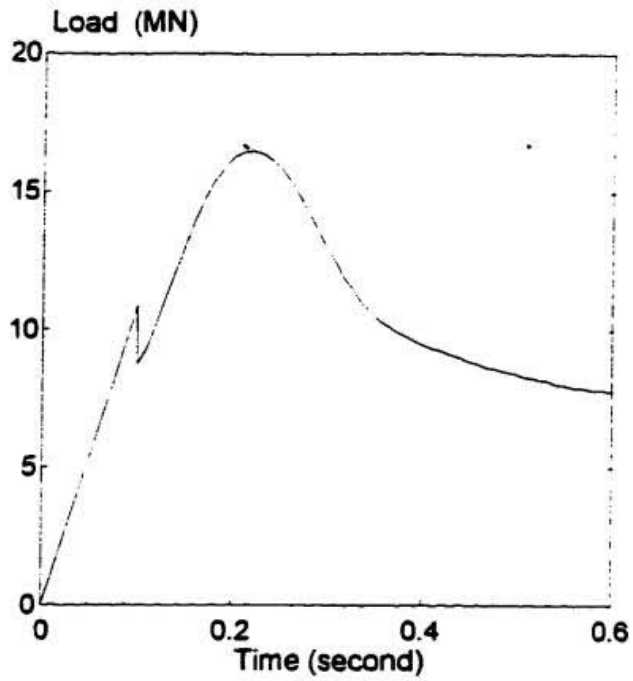

Figure 2. 21 Effect of Spalls on Total Force

pressure decreases as the indentation proceeds. The decrease is caused by the damage of the ice near the ice-indentor interface. The pressure will eventually decrease to a very small value when the ice is completely damaged and extruded. The whole process corresponds to the formation and disappearance of a critical zone. Figure 2.21 shows the force -time curve; the peak obtained and subsequent decline in load results from the damage process in ice. The peak load in Figure 2.21 should be contrasted with the value about 40 MN that occurs in the absence of spalling.

2.8 Conclusions

Ice-structure interaction was analyzed in terms of ice fracture and ice damage processes. The fracture causes pieces of ice spalling off and formation of localized high pressure regions (critical zones). In these regions ice is subjected to sever damage and results in the decline of total indentation force. Critical zones are key elements in estimation of local ice pressure and fracture trajectory governs the sizes, locations and intensities of these zones.

Two beam models for fracture, namely Kendall's double cantilever beam and the model of Hutchinson and Suo, were analyzed. Both models are limited to the case of long open cracks. The model of Hutchinson and Suo provides a better alternative which also considers the compressive component of strain energy and can be used for mixed mode fracture. This model was subsequently used in analyzing the fracture strength of an ice sheet with an open crack. Monte Carlo simulations were carried out, in which factors such the location of the crack and the load configuration were chosen randomly. Results show that uncertainties in these factors cause significant variations in fracture strength.

Initial analysis of small closed cracks at three different locations shows that shear cracks and mixed mode cracks are the likely candidates for spall development. The location and the orientation of the crack dictate the trajectory of crack propagation hence also govern the size and location of critical zones. Because of the randomness of flaws in nature, the critical zones are also random. A probabilistic approach to these critical zones and ice loads is necessary, which is investigated in the next chapter.

Chapter 3

Probabilistic Analysis of Ice Loads

3.1 Introduction

As discussed in Chapter 2, ice-structure interaction is characterized by spalls and critical zones as the result of fracture and damage process. This affects three distinct regions of pressure in a design area. The first region is the critical zone where intense local pressures and pressure gradients exist. These are caused by the spalls and may also be attributed to the forced extrusion of damaged ice in a very narrow layer between solid ice and the structure. Measurements in the medium scale indentation tests (Frederking et al., 1990) and in ship trials (Glen and Blount 1984) indicate that the pressure in this region may reach up to 70 MPa over a fairly small area. In the second region, lower pressures are present. This region may be likened to an area of "background pressure". Such pressure is associated with the ejection of granular ice in wide spaces and is much lower than those in critical zones. The third region is one in which pressure is approximated by zero. This region is associated with areas of spalls where ice is no longer in contact with the structure. These three regions are shown schematically in Figure 3.1. Among the three regions, the critical zones are most important in estimating the ice loads and are the key elements in the approach presented in this chapter.

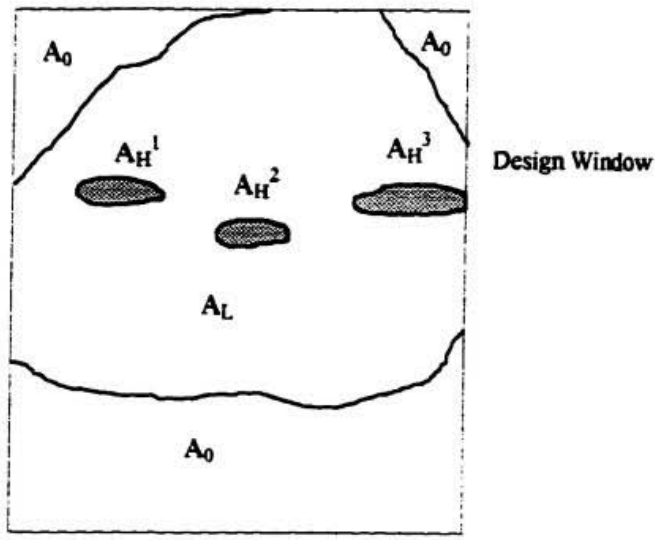

A_H: Critical Zone of High Pressure
A_L: Area of Low Pressure
A_0: Spall Area

Figure 3. 1 Schematic View of Three Regions of Pressure within a Design Window.

Figure 3.2 shows pressure measurements taken onboard CCGS Louis St Laurent during a ramming test (Blount et al., 1981). Each frame in the figure represents the pressure distribution on the instrumented panel at a point in time. The transducer marked with the dark color is the one with the maximum pressure while the ones marked by light color are active transducers. Indicated at the lower right corner of each frame is the value of the maximum pressure. The maximum pressure during the ram reached 51 MPa. The shaded areas in the figure approximate the critical zones. As indicated in the figure, these critical zones appear to be random, move from place to place, and change in intensity and

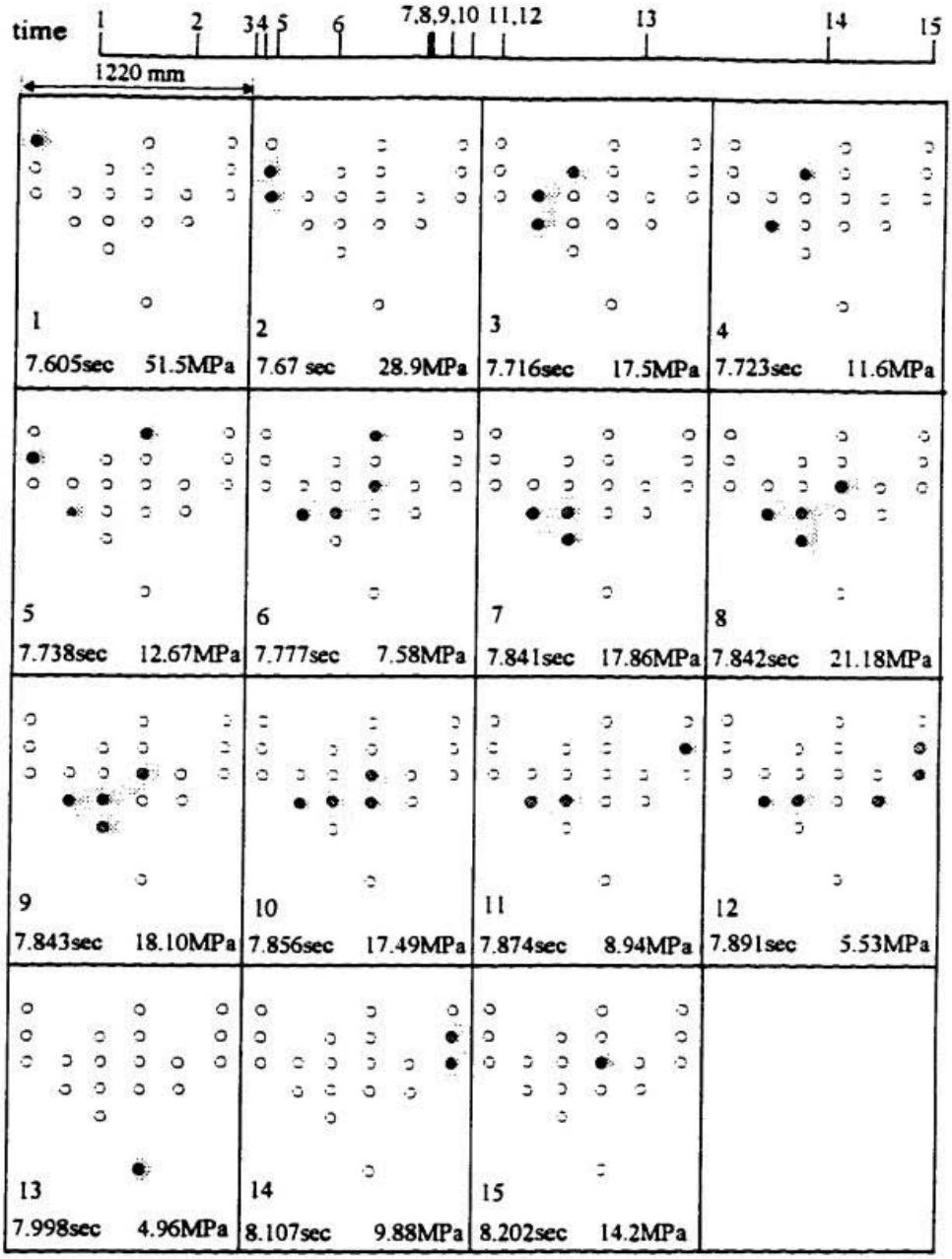

Figure 3. 2 Critical Zone Activity Within the Contact Area. (based on Blount et al., 1981, Case I)

size. This randomness of critical zones can be attributed to the probabilistic nature of fracture, which is associated with the randomness of flaws in ice.

Johnston (1993) performed an extensive analysis on critical zones based on several sets of test data including the medium scale indentation tests conducted at Hobson's Choice Ice Island (Frederking et al., 1990), the ship trials of the Louis St. Laurent (Blount et al., 1981), the CanMar Kigoriak (Dome Petroleum ltd., 1982) and an ice event experienced by the offshore structure "Moliqpak" (Jefferies, 1988). Fundamental properties of critical zones such as average size, total force within the zone and spatial density were quantified. The author found that critical zones, which are of the order of 0.1 m^2, and that the forces range from 0.1 to 4 MN. The author also found that the best data set for the analysis of the critical zones is the ship trial data of Louis St. Laurent. For other data sets, the area that a pressure sensor represents is of the same order of magnitude as that of a critical zone and in some cases more than one critical zone may exist on a single sensor.

Jordaan , Xiao and Zou, (1993) proposed a probabilistic treatment of critical zones in estimating the local ice loads. In this approach, the load on a design area is applied through a random number of critical zones, each with a random force. The number of critical zones was suggested to be modelled as a birth and death process and the critical zonal force was suggested as gamma distributed. Further work was performed by Johnston (1993) by treating the load as a compound Poisson process in which the number of critical zones was modeled by a Poisson process and the zonal force was modeled by a

gamma distribution. Monte Carlo simulations were performed to simulate this process. The approach was applied to the analysis of the trial data of Louis St. Laurent. Discrepancies were found between measured and simulated results, in part because of the limited number of simulations. A similar approach, treating the critical zones as a compound Poisson process, was proposed by Kujala (1994) but no application was given in the work.

The present approach is based on the works of Jordaan. Xiao and Zou, (1993) and Johnston (1993). First, a statistical analysis on critical zones is carried out based on the ship trial data of Louis St Laurent. Due to the limitations in size of the instrumented panel and the spatial resolution of the pressure sensors, difficulties exist in interpreting the measured data. For example, for those sensors located near the border of the instrumented panel, the measurement may present only a portion of a critical zone which extend beyond the border. To explore the uncertainty in this, different assumptions are made in the analysis. Probabilistic formulations of critical zones in two scenarios are proposed, and the corresponding probability distributions of the pressure on the design area are derived using a Monte Carlo simulation scheme.

Once the probability distribution of the pressure is derived, extremal statistics are used to estimate the extreme value of ice load which a structure is likely to experience. The key issue in extremal analysis is exposure. Exposure defines the extent that the structure of ship may experience ice hazards. For instance, an arctic vessel may experience thousands of impacts by multiyear ice during one year, whereas a ship in the offshore

offshore Newfoundland water may encounter an iceberg impact once a year. The extreme pressure for the first would be much greater than the latter.

The probabilistic formulation of critical zones, together with the extremal analysis accounting for different exposure, yields an algorithm for the estimation of the design ice load.

Before proceeding with our approach, we review of the fundamentals of extremal analysis and the previous experience in statistical analysis of ice loads.

3.2 Extremal Analysis

For the purpose of formulating a design code for a certain standard, one needs to know the largest probable environmental load which a structure may encounter. Extreme value statistical analysis has been developed for this purpose. An extreme value is defined as the largest value of a random quantity expected to occur in a certain number of observations or in a certain period of time, i.e. a return period. For ice loads, this could be the maximum ice load during an ice navigation season or the "one hundred year load" for an iceberg collision. In the following, the extreme value of a general natural phenomena is examined.

The random nature of a phenomenon can be characterized by a probability density function (*pdf*) of one (or more) random quantities, X, which describe the intensity of the event. For example, an ice ramming event can be described by the ice load and the duration of the interaction. The *pdf*, $f_X(x)$, is essentially valid for a specific site at any point in

in time, and frequently a considerable amount of prior analysis is required in order to derive f_X. The distribution, F_X, is usually called the parent distribution.

During a design lifetime, the structure may experiences a number n of consecutive events. For instance, a ship in the arctic region may experience hundreds of multiyear impacts each year; a ship in the offshore Newfoundland waters may encounter an iceberg impact every other year. In each case, we need to analyze the maximum, Z, among a number n of random quantities X:

$$Z = \max(X_1, X_2, \ldots X_n). \tag{3.1}$$

According to order statistics, and assuming that X_i, ($i = 1, \ldots n$), are independent and have identical *pdf*, we can derive the probability distribution of Z from the parent distribution F_X :

$$F_Z(z) = F_X^n(x) \tag{3.2}$$

where $F_Z(z)$ and $F_X(x)$ are cumulative distribution functions (*cdf*) of Z and X, respectively. The distribution $F_Z(z)$ is called an extremal distribution and it is valid for a specified number of events or a period of time.

As shown by Maes (1985), this procedure can be extended to cases where X_i ($i = 1, \ldots n$), are not independent and do not have identical densities. If n is also random, the *cdf* of the extreme value Z can be described as:

$$F_Z(z) = \sum_{n=0}^{\infty} F_X^n(z) p_N(n) \tag{3.3}$$

where $p_{N(n)}$ is the probability of the number of event, n. If n follows a Poisson process, F_Z can be expressed as:

$$F_Z(z) = \exp(-\lambda t(1 - F_X(z))) \tag{3.4}$$

where λt is the expected number of events.

If the parent distribution describing the natural phenomenon is known, the extreme value can be evaluated exactly by applying order statistics. Unfortunately, the parent distribution is usually difficult to obtain. In this case, one has to use an approximate method or an asymptotic formulation.

A very popular asymptotic formulation is the double exponential distribution with the form:

$$F_Z(Z) = \exp(-\exp(-(z - z_0)/\alpha)) \tag{3.5}$$

where F_Z is the cumulative distribution. α and z_0 are the dispersion and characteristic largest value respectively and can be obtained from:

$$\alpha = \frac{\sqrt{6}\sigma_z}{\pi} \tag{3.6}$$

$$z_0 = m_z - \frac{\sqrt{6}}{\pi} 0.577\sigma_z \tag{3.7}$$

where m_z and σ_Z are the mean and standard derivation of the extreme value, respectively. The double exponential distribution is also called Gumbel I distribution or the Fisher-Tippett distribution.

Another approximation to the extremal problem is the parent distribution with an exponential tail. Consider the tail of an arbitrary unbounded *pdf*, $f_X(x)$, in Figure 3.3. The shaded area under the tail is equal to $1-F_X(x)$, and it decreases with increasing x. At the same time, however, $f_X(x)$ decreases. It can be shown that the shaded area under the tail (called the probability of exceedance) has an exponential distribution for most of the distributions used in engineering practice, with the following form:

$$P_e = 1 - F_x = \exp(-(x - x_0)/\alpha) \tag{3.8}$$

The distribution with an exponential tail is useful in cases when we are only interested in the region which has a small probability of exceedance. This type of distribution is used in a number of places in this chapter.

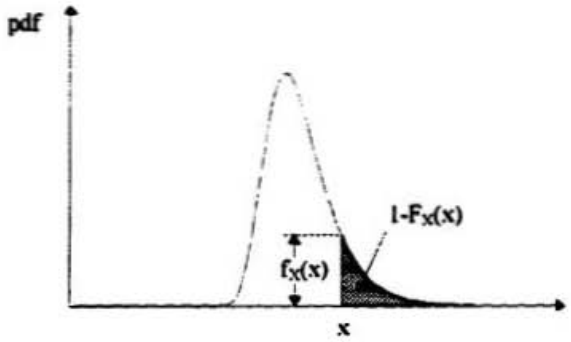

Figure 3. 3 The Tail of a Distribution

3.3 Previous Experience in Statistical Analysis of Ice Loads

3.3.1 Overview

According to current literature, Kheysin (1973a, b) was the first to use a probabilistic approach to ice loads on ships. He used a Poisson distribution for the number of impacts in an arbitrary interval of time, based on measurements by Likhomanov (1973). Maes et al., (1984) performed a study on probabilistic methods for fixed structure in ice and the methodology has been reviewed by Nessim et al., (1987), Nessim and Jordaan (1991), and Blanchet (1990). Daley and his co-workers formulated the ASPEN model over several years and this culminated in the publication by Daley et al. (1991). Kujala (1991) used the results of probabilistic methods to study the safety of ships in the Baltic Sea with respect to ice induced loads. Jordaan et al. (1993a) presented a probabilistic approach to the local ice pressure based on test data of ship ramming trials. This approach provided a framework for the treatment of extremal values and exposure for the present study. The approach is described in the following section.

3.3.2 An Approach Based on Data of Ship Ramming Trials

This section describes a probabilistic analysis of local ice pressure by Jordaan et al., (1993a). Two main data sets for ship-ice interaction are used, the USCGC Polar Sea (Daley et al., 1986) and the MV CanMar Kigoriak (Dome Petroleum Ltd., 1982). The pressure data from the Polar Sea were collected during an April 1983 deployment of the vessel in the North Chukchi Sea. This data set consists of 513 impacts with multiyear and

heavy first-year ice features recorded on an instrumented panel of 9.1 m^2 located in the bow of the ship. This panel was subdivided into 60 subpanels of 0.1516 m^2. For each collision, the highest pressure on a single subpanel was recorded (Appendix A of Daley et al., 1986). The data were ranked in descending order. The probability of exceedance, P_e, was calculated, where $P_e = i/(n+1)$, i is the rank and n is the number of data points. The pressure data are plotted against the log of P_e in Figure 3.4. Since there are 60 instrumented panels exposed, the maximum reflects to a $60n$ exposure of a panel. Figure 3.4 also shows the data re-plotted, adjusted for the reality of this exposure. The result is a vertical shift of the best fit line giving a lower probability per panel. The data are characterized by an exponential tail discussed earlier.

The pressure data from the Kigoriak were collected during August and October, 1981 deployments of the vessel. The August tests were conducted primarily in thick first-year ice and second-year ice while the October tests were conducted in multi-year ice. During these tests, 397 rams were recorded and the loads on two instrumented areas *A1* (1.25 m^2) and *A2* (6.00 m^2) were measured. The two data sets were combined and the panel pressures ranked in descending order for each area. The probability of exceedance was calculated as before, where n is the number of rams producing pressure greater than zero on the instrumented panels. There were 120 such rams for *A2* and 181 for A1.

For most practical cases, the tail of a distribution can be represented by the exponential distribution given in Equation (3.8). Analysis of plots similar to Figure 3.4 for various data sets shows that the parameter α in Equation (3.8) is a function of the fixed

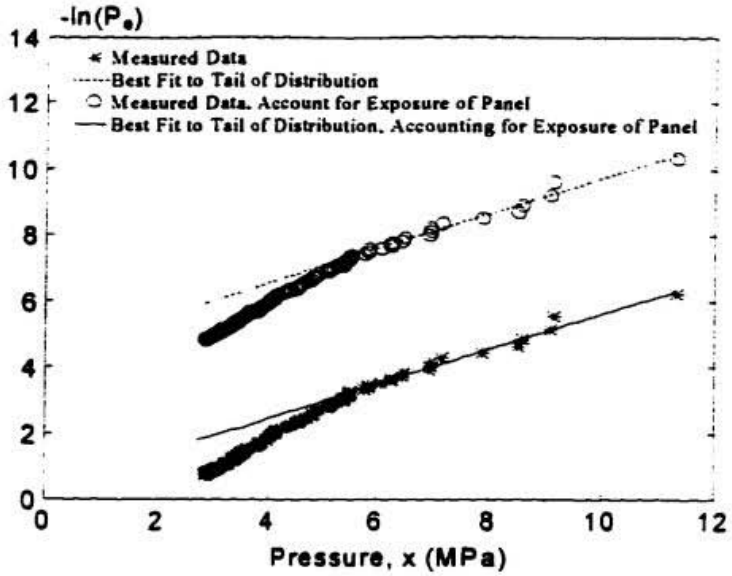

Figure 3. 4 Ranked Data on Local Pressure Measured Onboard the USCGC Polar Sea.

(Jordaan et al. 1993a)

area and $x_0 < 0.2$ MPa. A tentative curve of α for use in design was presented, (see Figure 3.5), given by:

$$\alpha = 1.25a^{-0.7} \tag{3.9}$$

where a is the area in m^2. The results are supported by the more detailed analyses of Maes and Hermans (1991) and Brown (1993).

One important factor in deriving the extreme ice loads is the occurrence rate of impacts. The analysis has been performed on the basis of the total number of rams per year. Each ram could also have two possible outcomes, namely "hits" and "misses". Here we will take a single panel in a fixed location. Those rams or interactions for which

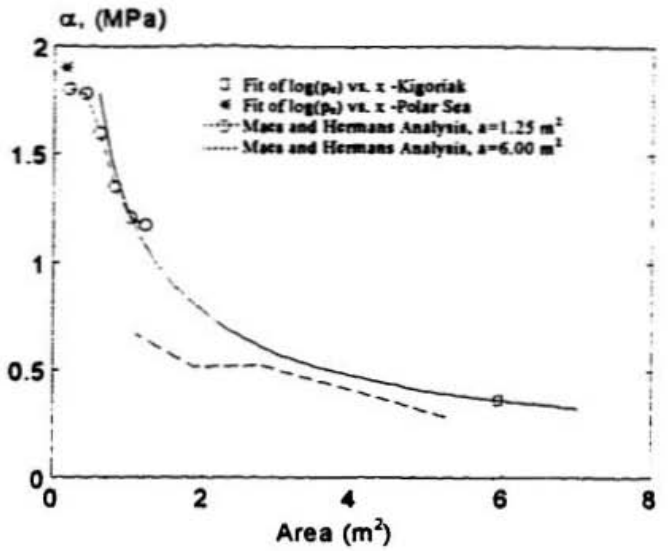

Figure 3. 5 Results of α for ln p_e vs. x Plots (Jordaan et al., 1993a)

no contact with the panel is made are omitted, only "hits" are included. In considering n events in future interactions, let r be the proportion of hits, we then need to consider only the number of "hits":

$$m = rn \tag{3.10}$$

where m is the number of hits, or in the case where m and n are random (noted as M and N),

$$\mu = r\gamma \tag{3.11}$$

where μ and γ are the expected number of events with hits and the expected number of events, respectively, per unit time.

If equation (3.8) applies, then the distribution of the maximum of Z can be obtained based on Equation 3.2 as:

$$F_Z(z) = (1 - \exp(-(z - x_0)/\alpha))^m \tag{3.12}$$

If the number of events is fixed and large, Equation (3.12) can be approximated by:

$$F_Z(z) = \exp\{-\exp[-(z - x_0 - x_1)/\alpha]\} \tag{3.13}$$

where $x_1 = \alpha(\ln n + \ln r)$.

If M is binominally distributed, with m trials per time interval, and the probability of an event per trial is given by p, then:

$$F_Z(z) = \{1 - p[1 - F_X(z)]\}^m \tag{3.14}$$

and Equation (3.8) provides possible distributions for F_X.

In the case of a Poisson process, substituting Equation (3.8) into (3.4) yields

$$F_Z(z) = \exp\{-\exp[-(z - x_0 - x_1)]\} \tag{3.15}$$

where $x_1 = \alpha(\ln \gamma + \ln r)$ and γ is the expected number of impacts. Note that Equations (3.13) and (3.15) have the same format except that n is a fixed large number and γ is an expected value.

As an example application, we consider a design area of 1.25 m^2, with α = 1.07 MPa, x_0 = 0 MPa and r = 0.46. The resulting probability distributions for pressure are

shown in Figure 3.6 for various exposures. For small μ, a "spike" of probability, of value $e^{-\mu} = e^{-\gamma\gamma}$ appears at the origin.

A design value can be chosen from Figure 3.6. If we choose a value z_e corresponding to a given exceedance probability, $[1-F_Z(z_e)]$, then

$$z_e = x_0 + \alpha\{-\ln[-\ln F_Z(z_e)] + \ln\gamma + \ln r\} \tag{3.16}$$

The value at 1% exceedance, the "100-year load" is

$$z_{0.01} = x_0 + \alpha(4.6 + \ln\gamma + \ln r) = 9.1 MPa \tag{3.17}$$

Note here that when x_0 is small, it does not affect the value of z_e significantly.

3.4 Statistical Analysis of Critical Zones

3.4.1 Definition of the Problem

To determine a design ice load, we need to know the total force on the design area. This force can be approximated by contributions from a number of critical zonal forces superimposed on a background pressure. As noted in Figure 3.1, a critical zone may be located on the border of the design window, with only a portion of the zonal force acting on the design area. To account for this uncertainty, we divide the critical zones into two groups, those fully located within the design window and those partially located inside the window. Two approaches are proposed to model these critical zones. In *approach A*, we assume that all critical zones are located within the design area. This is schematically illustrated in Figure 3.7 (a). In *approach B*, we consider the critical zones

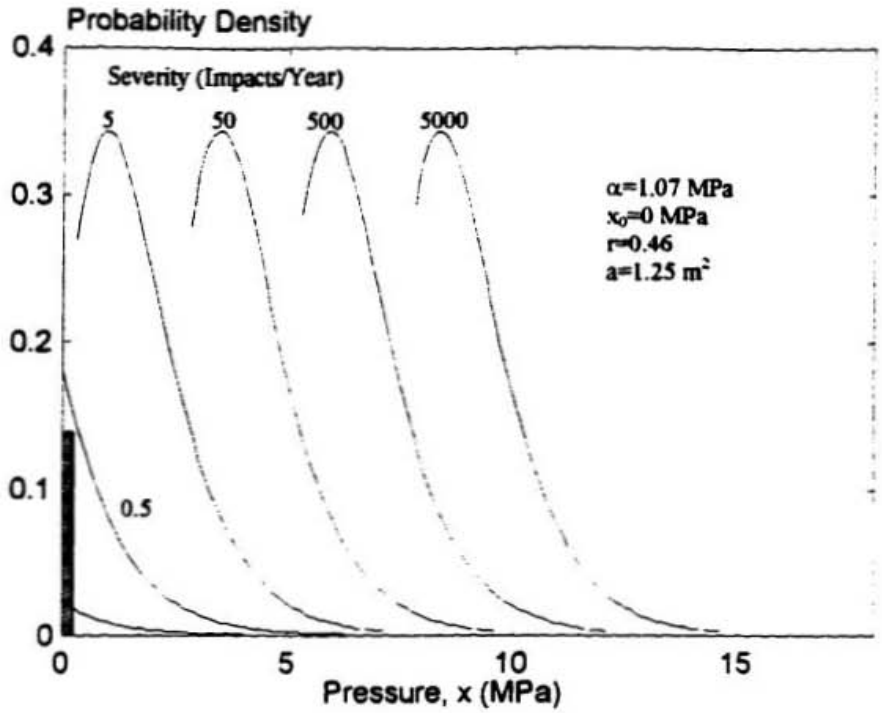

Figure 3. 6 Probability density of extreme pressure (Jordaan et al., 1993a)

which are located within the window and those on the border separately. For critical zones on the border, the proportion of the zonal force inside the window is considered when calculating the total force on the design area. This is illustrated in Figure 3.7(b). Parameters of critical zones are calibrated based on the analysis of ship ramming data of Louis St. Laurent.

3.4.2 Analysis of Ship Trial Data of Louis St. Laurent

In November 1980 the Canadian Coast Guard conducted impact tests on multiyear ice with CCGS Louis St. Laurent. These tests were the first direct measurements of ice

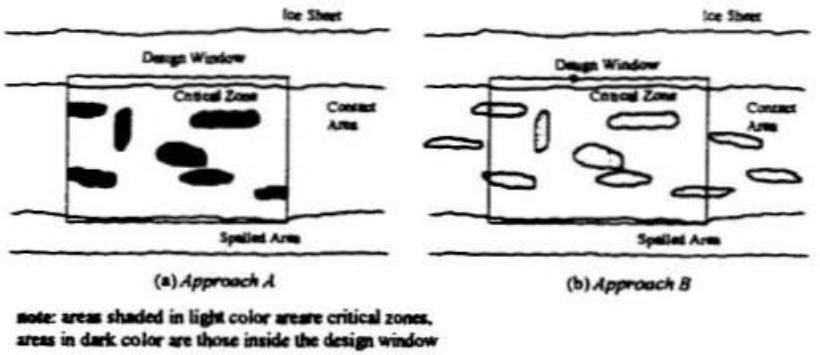

Figure 3. 7 Schematic Illustration of Contact Area, Critical Zones and Design Windows

pressure in the high arctic (Daley and Riska, 1990). The principal objective of the 1980 trials was to measure the pressure generated in the impact zone between the ship and ice. For this purpose, an array of 25 pressure sensors and 12 strain gauges were installed in the bow thruster compartment. The location of the pressure sensors are illustrated in Figure 3.8. During the ramming tests, five pressure sensors were inactive reducing the contact height of the ice sheet to 1.38 meters and the 'active window' to 1.62 m^2. Note that, due to the limit in spatial resolution of pressure sensors, the "effective instrumented area" could be smaller (1.25 m^2) as indicated in Figure 3.8. The pressure distribution on the instrumented panel was plotted at various points in time and the critical zones were approximated in a way similar to Figure 3.2. Because the spatial resolution of the pressure sensors is limited, care is needed in determining the zonal area and force. For instance, ice forces may exist between sensors L6, L9 and L10; L33 and L34 which were not measured. In addition, the pressure measured by sensors on the border of the 'active window' may extend beyond the border. To consider the uncertainties due to the limit in size of

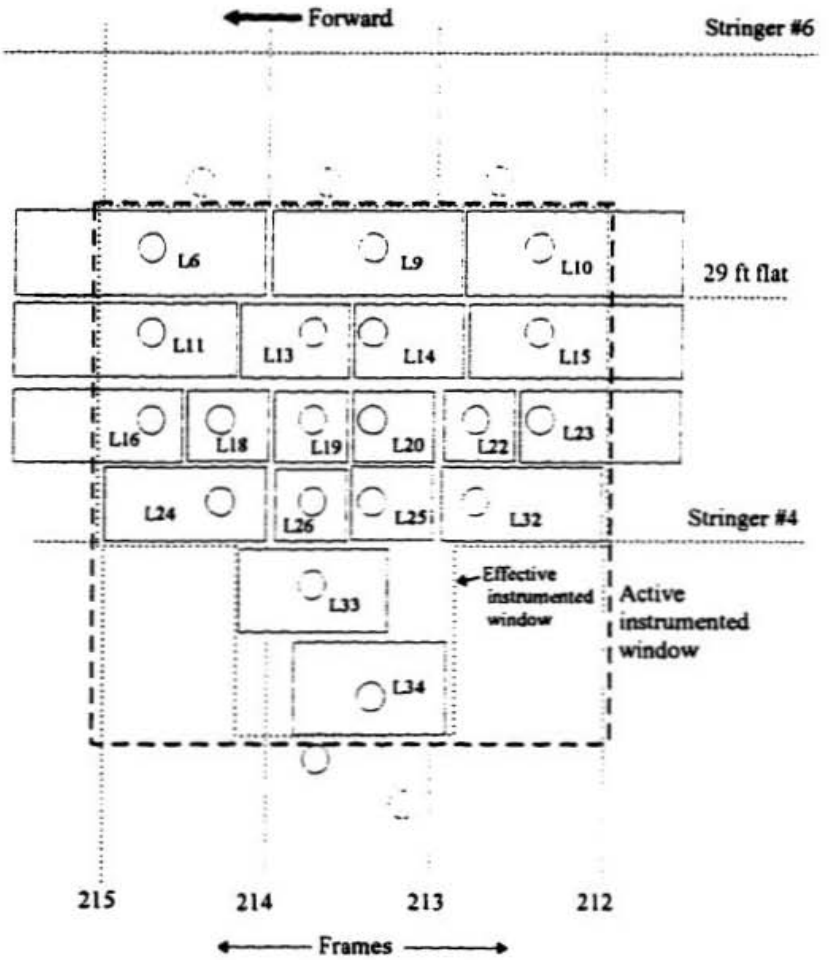

Figure 3. 8 Location of Various Pressure Sensors (dashed circles indicate sensors in inactive region, each rectangular in solid lines indicates the area a pressure sensor represents in approach B)

the instrumented panel and spatial resolution of the pressure sensors, we made two assumptions: first, each sensor on the panel represents an area of 0.0472 m^2. Ice forces beyond this area (i.e. the gap between sensors L6 and L9) is negligible. We refer this as *assumption A*. *Assumption A* is consistent with the analysis by Johnston (1993) and Blount et al., (1981). Second, each sensor represents a 'weighted area' as shown in Figure 3.8 by rectangular solid lines. For those sensors located near the edge of the instrumented window, the weighted areas extend beyond the border. Accordingly, critical zones measured by these transducers are located on the border of the window. We refer this as *assumption B*. In both cases, the pressure measured on a sensor represents the uniform pressure on the designated area. Figure 3.9 illustrates how the pressure distribution is approximated. As shown, *assumption A* considers only the area within the window, while *assumption B* accounts for the area beyond the boundary. In the figure, the shaded areas are active. Adjacent loaded areas are considered as one critical zone. In each case, the number of critical zones are counted and the zonal force is approximated as:

$$F = \sum_{i=1}^{n} p_i A_i \tag{3.18}$$

where F is the zonal force, n is the number of active pressure sensors in the zone and p_i is the pressure on *ith* sensor. A_i is the area that the *ith* sensor represents. In *assumption A*, $A_i = 0.0472\ m^2$ for all sensors, for *assumption B*, A_i is listed in Table 3.1. Note that areas assigned to sensors L6, L10, L11, L15, L16, and L23 are obtained under the assumption

Table 3. 1 Area assigned for each pressure sensor

Sensor	A_i (m^2)	Sensor	A_i (m^2)	Sensor	A_i (m^2)	Sensor	A_i (m^2)
L6	.1416	L14	.0708	L20	.0472	L25	.0472
L9	.118	L15	.118	L22	.0472	L32	.0944
L10	.118	L16	.0944	L23	.0944	L33	.0944
L11	.118	L18	.0472	L24	.0944	L34	.0944
L13	.0708	L19	.0472	L26	.0472		

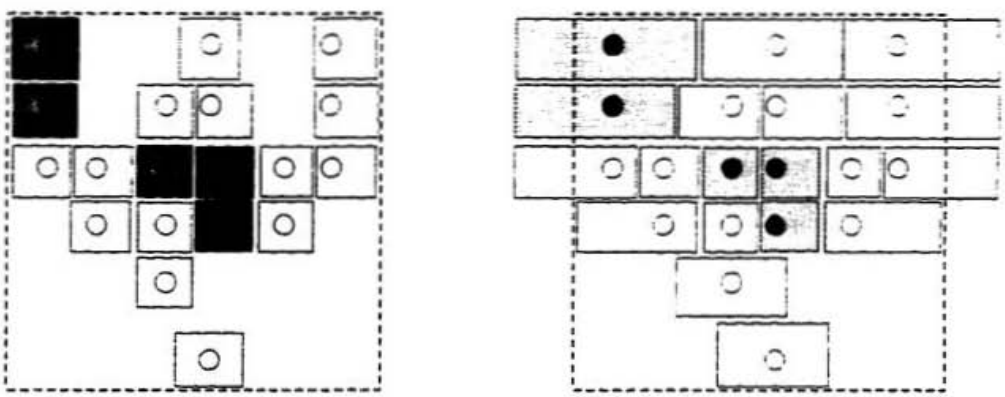

(a) *Assumption A*

(b) *Assumption B*

Figure 3. 9 Approximation of Critical Zones

that the weighted area extend beyond the boundary for an additional area of 0.0473 m^2. This assumption is not accurate and is only for the purpose of comparison.

Controlled impact tests were conducted on November 12 and 13, 1981 with large multi-year floes off Bylot Island. These impacts consisted of backing and ramming into a selected portion of a multi year floe with the starboard side of the ship. The target area on the ship was the instrumented hull in the starboard bow thruster compartment. Control of the impact was difficult because of high winds and the need to avoid damage to propellers.

Initial analysis of the data by Blount et al. (1981) shows that only twenty impacts are significant enough for further analysis. These impacts had a 'clean' impact on or close to the instrumented area. 'Of 20 impact cases identified, one, case 10, while indicating strains, showed no response on the pressure transducers'. This reduced the number of cases to 19.

Johnston (1993) selected 9 cases which 'demonstrated well defined impact to the panel of pressure transducers' with crushing accompanying the interaction. In fact, a 'good impact' as defined by Blount et al. (1981) corresponds to these cases. A 'good impact' is determined through the visual record as one which ' hits all instrumented panels simultaneously or from front to rear, with ice-crushing present'. Impacts not included in the 'good' category are those which had 'no definite visual impact', 'with the broken ice passing the panel of pressure transducers' , with 'no ice-crushing present' , in which 'the ice sheet probably impacted fore or aft of the panel of pressure transducers'.

It was noticed by Johnston (1993) and by the author of the present study that some of the 'poor' impacts produced significant pressure on the panel. Therefore all 19 cases have been included in the analysis of the critical zones, since they provide a complete data base for different impact scenarios. This does not imply that the previous analysis by Johnston (1993) based on 9 cases is invalid, but care must be taken in applying the results. The results should be modified such that the effect of exposure is considered. The results of Johnston (1993) are based on 9 'good impacts' out of 19 cases, therefore, when applying the results, a proportion of 9/19 should be considered.

In estimating ice loads, we are interested in the peak value of the pressure. Figure 3.10 shows the time traces of pressure from active transducers. 'Time slices' which correspond to pressure peaks (points A to I in the figure) are chosen for analysis. At each time slice, a pressure distribution similar to that in Figure 3.9 is constructed and the critical zones are approximated. A total number of 266 time slices are selected and the results are presented in terms of zonal area, spatial density and zonal force of critical zones. The zonal area and spatial density are presented in Table 3.2. The number of time slices used in each ram is also counted and the mean value is given in Table 3.2. Note that the spatial density of the critical zones is derived from the area of the "active instrumented window" shown in Figure 3.8. The densities correspond to the "effective instrumented area" were also given in the table for comparison.

Table 3. 2 Mean zonal Area and the Spatial Density

	Assumption A	*Assumption B*	
		within the window	on the border
Spatial Density ρ	0.8927 zones/m^2	0.6183 zones/m^2	0.1674 zones/m
Spatial Density ρ^*	1.16 zones/m^2	0.80 zones/m^2	
Mean of Zonal Area	0.0809 m^2	0.136 m^2	
mean number of time slices used in analysis for each ram: 9			

(**Note**: ρ^* corresponds to the "effective instrumented area" of 1.25 m^2)

The zonal forces are ranked in descending order and the probability of exceedance is calculated according to $P_e = i/(i+1)$, where i is the rank and n is the number of the time slice. The results of both approaches are presented in Figure 3.11.

The lines fitted to the data indicate that the distributions of the zonal force can be well represented by an exponential distribution as given by Equation (3.8). The parameters fitted to Equation (3.8) are listed in Table 3.3, where $\gamma = 1/\alpha$. Notice that x_0 is very small and the distribution can be approximated by the following equation:

$$f_X(x) = \gamma e^{-\gamma x} \tag{3.19}$$

Table 3. 3 Parameters of exponential distribution of critical zonal force

	Assumption A	*Assumption B*
γ	1.2876	0.7235
x_0	0.07235	0.0793

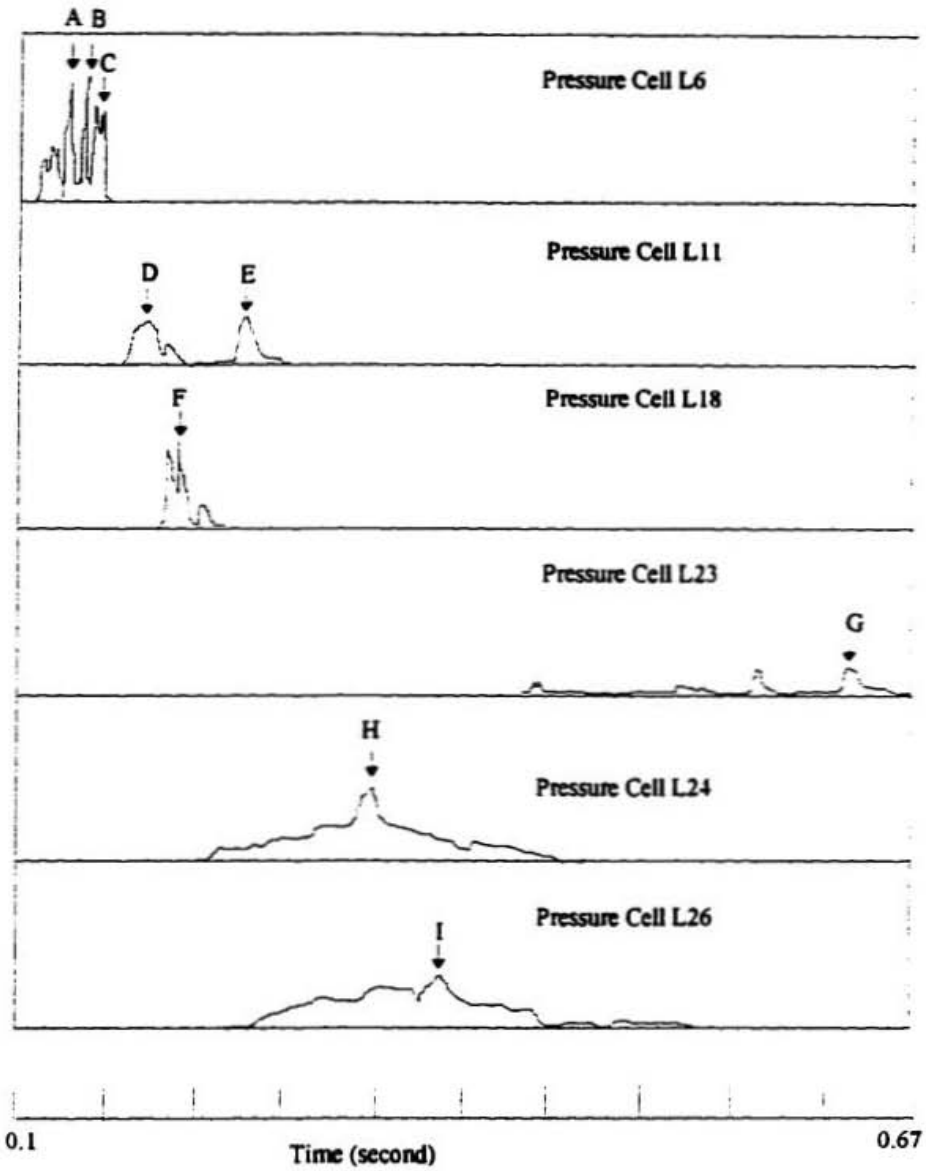

Figure 3. 10 Time Slices Correspond to Peak Pressures

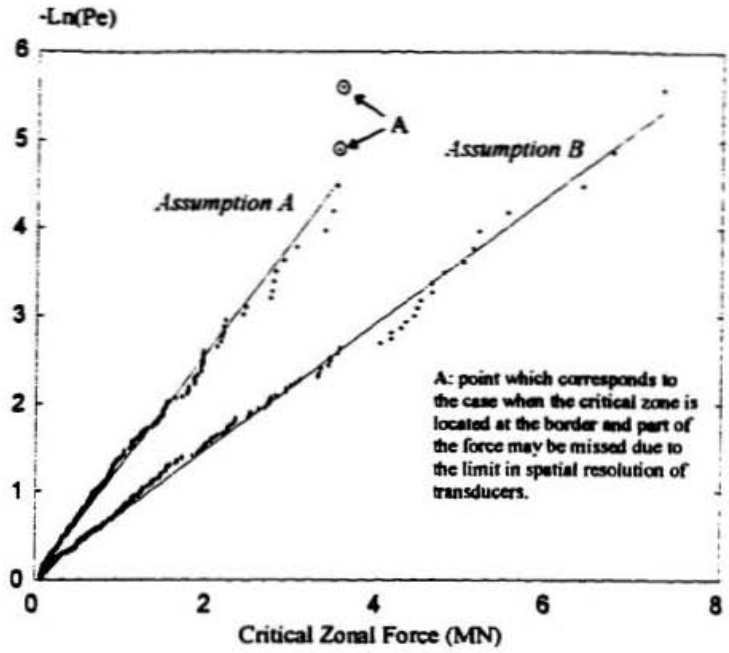

Figure 3. 11 Probability of Critical Zonal Force

Compared with the results of Johnston (1993), the spatial density of critical zones from *assumption A* is higher while the mean area and the force of critical zones are lower. This is because, in the approach of Johnston (1993), critical zones with zonal pressure of 2 MPa were considered as background pressure and were not included in the analysis. The present analysis included all the cases. As a result, the present analysis included more "small critical zones" which have lower values of zonal area and zonal forces.

3.4.3 The Probabilistic Model

Approach A: in this case all the critical zones are located within the design area. We assume that the total force on the area is acted through a number of critical zones, each with

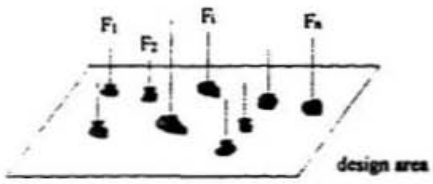

Figure 3. 12 Schematic View of A Design with The Critical Zones

a random force (see Figure 3.12). Background pressure is assumed small here and can be treated separately elsewhere.

We approximate the critical zonal force in general by a Gamma distribution:

$$f_X(x) = \frac{1}{\Gamma(\nu)} \beta^{\nu} x^{\nu-1} e^{-\beta x} \tag{3.20}$$

where β is the scale parameter and ν governs the shape of the distribution,

$$\beta = \frac{E(X)}{Var(X)} , \tag{3.21}$$

$$\nu = E(X)\beta , \tag{3.22}$$

where $E(X)$ and $Var(X)$ are the mean and variance of the zonal force, respectively.

The total load on a design area, Y, is the sum of the critical zonal forces:

$$Y = \sum_{i=1}^{n} X_i \ , \tag{3.23}$$

where n is the number of critical zones.

If the number of critical zones, n, is fixed, the total load Y has a density function similar to that given by Equation (3.20). Thus

$$f_Y(y) = \frac{1}{\Gamma(\nu_1)} \beta_1^{\nu_1} y^{\nu_1 - 1} e^{-\beta_1 y} \ . \tag{3.24}$$

The mean and variance are given as:

$$E(Y) = nE(X) \ , \tag{3.25}$$

$$Var(Y) = nVar(X) \ , \tag{3.26}$$

where β_1 and ν_1 are defined as in Equations (3.21 and 3.22).

Assuming that the number of critical zones n is proportional to the design area:

$$n = \rho a \ , \tag{3.27}$$

where ρ and a are the spatial density of critical zones and the design area, respectively. The design pressure on the area is also a Gamma distribution. With a change of scale, the mean and the variance can be derived as:

$$E(P) = \rho E(X) \ , \tag{3.28}$$

$$Var(P) = \rho Var(X) / a \ , \tag{3.29}$$

Note that the mean pressure does not change with respect to the design area and the variance decreases when the design area increases.

If the number of critical zones is random and follows a **Poisson process**, the ice pressure follows a **compound Poisson** process with mean and standard deviation (Ochi, 1990):

$$E(P) = \rho E(X) \ , \tag{3.30}$$

$$Var(P) = \rho[Var(X) + E^2(X)] / a \ . \tag{3.31}$$

If the critical zonal force follows an exponential distribution (a special case of Gamma distribution with $\nu = 1$ in Equation (3.20)), and the zonal force has mean and variance given by:

$$E(X) = \frac{1}{\gamma} \ , \tag{3.32}$$

$$Var(X) = \frac{1}{\gamma^2} \ , \tag{3.33}$$

equations (3.30) and (3.31) become:

$$E(P) = \frac{\rho}{\gamma} \ , \tag{3.34}$$

$$Var(P) = \frac{2\rho}{a\gamma^2} \ . \tag{3.35}$$

***Approach B*:** in this case, some critical zones are partially located within the design area, and the total force is:

$$Y = \sum_{i=1}^{n^1} x_i^1 + \sum_{j=1}^{n^2} \delta x_j^2 \ , \tag{3.36}$$

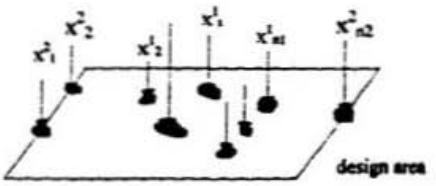

Figure 3. 13 Modelling of Critical Zonal Forces

where Y is the total force, n^1 and n^2 are number of critical zones within the area and on the border, respectively. x^1 and x^2 are random forces and δ is the proportion of a zonal force within the design area. δ may be random. Tentatively, a value of 0.5 is used for δ in the present analysis. This is consistent with the calibration of the spatial density of the zones on the border. The above approach is schematically illustrated in Figure 3.13. The probability distribution of ice pressure due to the zones within the area and on the border can be derived respectively in a way similar to that used in *approach A*. Assuming that both numbers for the critical zones located within the design area and on the border follow Poisson processes and the zonal forces follow exponential distributions, and assuming that the proportion of the zonal forces inside the design area is 0.5 for those critical zones on the border, the mean and variance of the pressure can be derived as follows:

$$E(p) = \frac{1}{\gamma}(\rho_1 + \frac{l}{2a}\rho_2) \ , \tag{3.37}$$

$$Var(p) = \frac{1}{a\gamma^2}(2\rho_1 + \frac{l}{2a}\rho_2) \ , \tag{3.38}$$

where γ is the parameter of the exponential distribution of the zonal force, ρ_1 and ρ_2 are the spatial density of critical zones within the border and on the border respectively and a is the design area.

3.4.4 Monte Carlo Simulation of Critical Zones

If the number of critical zones in a design window follows a Poisson process, the probability distribution of ice pressure can be derived using a Monte Carlo simulation scheme described below.

First, we simulate the scenario of *approach A* (Figure 3.12). For a given design area, the probability of the number of critical zones is calculated using:

$$P_N(n) = \frac{1}{n!}(\rho a)^n e^{-\rho a} \quad , \tag{3.39}$$

where n is the number of critical zones, ρ is the density of critical zones, a is the design area. In each simulation, the number of critical zones is selected randomly from the probability distribution calculated from Equation (3.39). For each critical zone, the zonal force is selected randomly from the probability distribution from Equation (3.19). The total force on the design area is then obtained by summing all zonal forces (Equation 3.23). The design pressure is the total force divided by the design area. A similar scheme is used for *approach B*, in which the number of critical zones in the design window and on the border are selected randomly, and the total force is calculated using Equation (3.36). The length of the border is assumed as $(a/1.5)^{1/2}$, where a is the design area.

Simulations using the schemes described above are carried out for design areas ranging from 0.4 to 6 m^2. For each design area, a number of 10000 simulations are carried out and the results of the pressure are ranked. Figures 3.14 and 15 show the probability of exceedance of ice pressure on an design area of 0.8 m^2 from *approaches A* and *B* respectively. The tails of these distributions can be well represented by an exponential distribution. By fitting the tails to the exponential distribution described in Equation (3.8), parameters α and x_0 for different design areas are obtained and presented in Figures 3.16 and 3.17. Also plotted in Figure 3.16 is the design curve proposed by Jordaan et al. (1993a). As indicated in the figure, the results of the present models, *approach A* in particular, agree well with the proposed design curve. Note that for design areas less than 0.59 m^2, the design value for α becomes a constant while those from the present analysis continue to increase with the decrease of the design area. This is because the present analysis assumes that critical zones are point loads, which is not accurate when the design area is very small.

Simulations using the densities of critical zones from the "effective instrumented area" have also been carried out and the results are included in Figures 3.16 and 3.17. Note that there is no significant change in result due to the change of density from active instrumented area to the effective area.

Results from Figures 3.14 to 3.17 suggest that the probabilistic distribution of local pressure can be approximated by an exponential distribution with parameters α and x_0 as given in Figures 3.16 and 3.17. Appropriate consideration of exposure is needed in

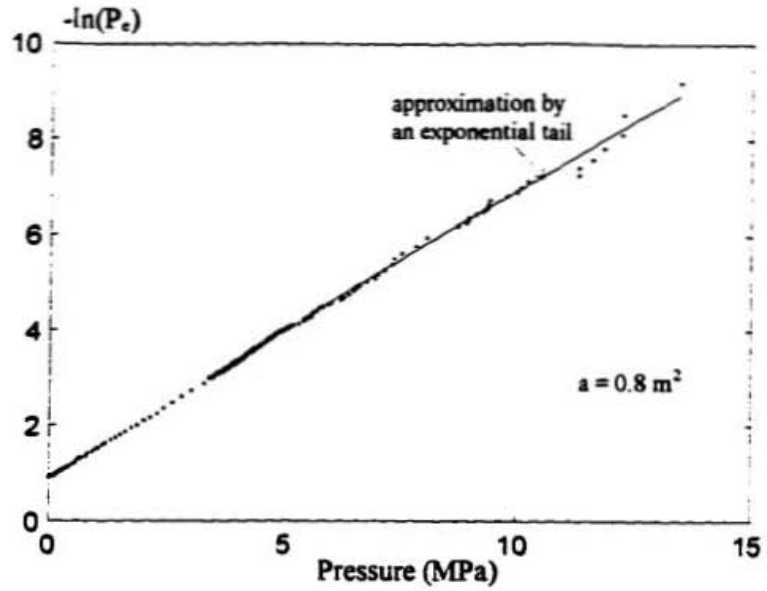

Figure 3. 14 Probability of Exceedance of Local Pressure (Approach A)

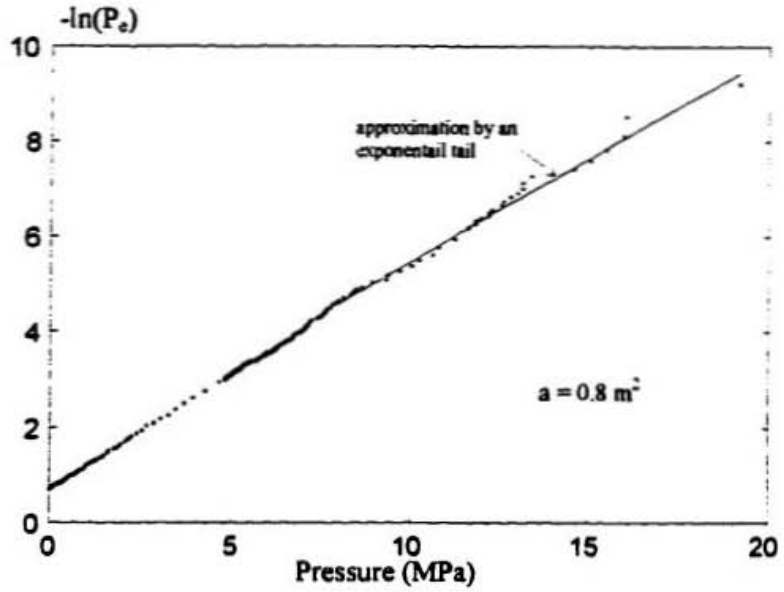

Figure 3. 15 Probability of Exceedance of Local Pressure (Approach B)

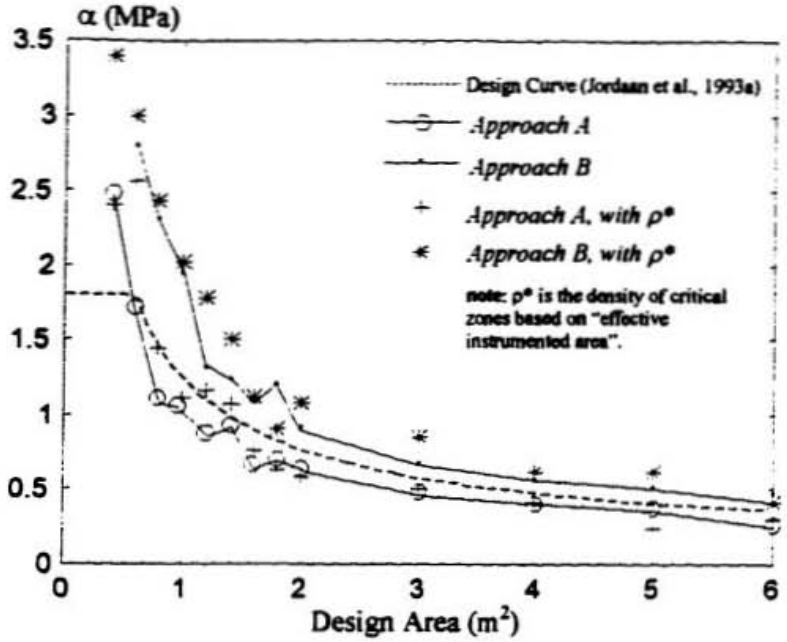

Figure 3. 16 Results of α Values

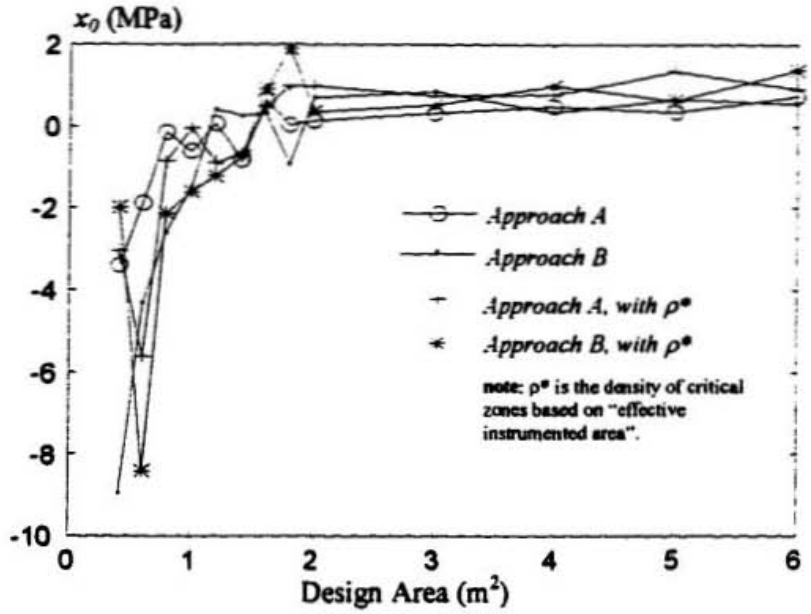

Figure 3. 17 Results of x_0 Values

applying the above results to a design problem. As mentioned previously, the above analysis is based on time slices corresponding to peak pressures during a ram. In choosing the design load, we are interested in the maximum pressure for a certain return period. To be consistent with the previous analysis on the ramming data of the Kigoriak and the Polar Sea by Jordaan et al., (1993a), we will use a ram as the base for our maximum pressure. The probability distribution of the maximum pressure during a ram can be derived from its parent distribution (pressure for each time slice) using the procedures described in Section 3.3. Assuming that the number of peak pressures for each ram follows a Poisson distribution with a mean number of 9 peak pressures per ram (see Table 3.2), the probability distribution of the maximum pressure per ram yields a similar form to that described in Equation (3.8) with a modification to x_0:

$$x_0^* = x_0 + \alpha \log(9) \ .$$

Values of x_o^* are presented in Figure 3.18.

Results presented in Figures 3.16 and 3.18 together with Equation (3.8) give the probability distribution of the maximum pressure per ram. In general, the results from *approach A*, with the parameters of critical zones calibrated from *assumption B*, are closer to the proposed design curves, whereas *approach B* gives more conservative results. Note that the proposed design curve was derived mainly from the data set of the ramming trial of Kigoriak, in which the pressure was measured by shear gauges and forces near or on the edges of the instrumented panel were not picked. From the view point of structural response, forces near the edge (support) have little effect on structural

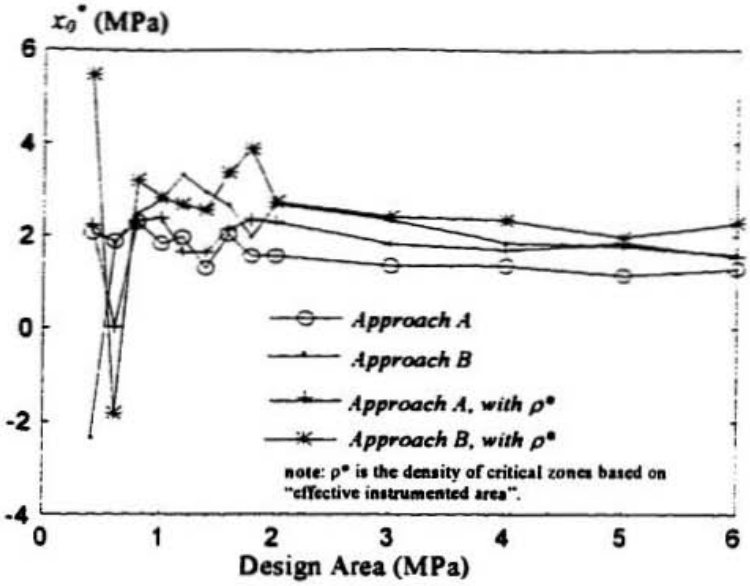

Figure 3. 18 Modified Values of x_0 for Maximum Pressure Per Ram.

response compared with those near the midspan and therefore can be neglected. To be consistent with the previous analysis on Kigoriak by Jordaan et al. (1993a), we recommend to use *approach A* in modelling the critical zones.

The design pressure corresponding to different rams can be modeled according to the extremal analysis presented in Section 3.3.

3.5 Exposure

In their approach to the local ice loads, Jordaan et al., (1993a) indicate that the key issue in extremal analysis is the exposure. It is important to examine the extent to which the structure is exposed to a natural hazard. For a ship structure interacting with ice, the exposure includes the duration of interaction, the area of contact, the position on the ship and the number of rams or the period of interactions. The present section investigates the

effect of duration of the interaction. This is achieved by a comparison between the ship ramming with multi-year ice in the Canadian Arctic and the icebreaking in the Baltic Sea. The effects of contact area, position on the ship and the number of rams are discussed later in Chapter 6.

The duration of the interaction is, in general, the length of an individual event. Figure 3.19 illustrates the two extreme cases of durations. In the first case (Figure 3.19 a), the duration of the impact may be a few seconds, whereas in the second case (Figure 3.19 b) the interaction is continuous and may last for a few days. In both cases, we are interested in finding the maximum load during the event. In the first case, the maximum load, x_{max}, is the maximum value among x_1 to x_3, while in the second case the maximum load, y_{max} is the extreme value among y_1 to y_7. The probability distribution for x_{max} and y_{max} can be derived from their parent distributions (distributions of x and y), respectively. Since y_{max} is the extreme value from a larger number of random quantities, its probability distribution tends to be more peaked, with smaller variance. This is illustrated schematically in Figure 3.19 (c). To further investigate these two cases, we examine the probabilistic characteristic of the ice ramming force for ships in the Canadian Arctic and the ice pressure on ships of the Baltic. An ice ram in the Arctic usually lasts a few seconds and is represented by the first case in Figure 3.19. The probability distribution of the maximum pressure per ram is analyzed in Section 3.3. The icebreaking for a ship in the Baltic sea might last a few days. For instance, a trip for an ice tanker from Baltic Proper to the Bothnia Bay takes two days. The probabilistic distribution of the maximum icebreaking pressure per trip is analyzed in the next subsection.

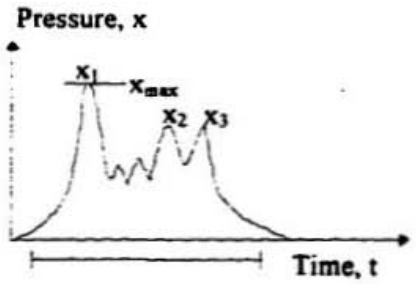

a) Ram, lasting several seconds

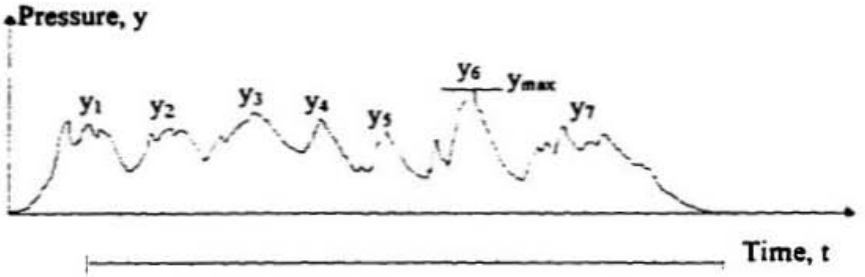

b) Continuous Interaction,lasting several weeks

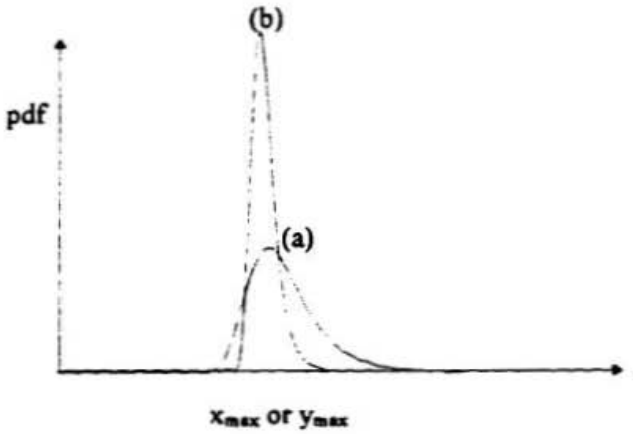

c) Load distribution corresponds to a) and b)

Figure 3. 19 Schematic Diagram Showing Time Traces for a) a Ram and b) a Continuous Interaction(from Jordaan et al., 1993a)

3.5.1 Statistics of Ice Loads in The Baltic

The statistical nature of ice loads on the ship hulls in the Baltic has been studied by a number of researchers, including Varsta (1983) and Kujala (1991, 1994). This analysis uses the results of an approach by Kujala (1991). The approach was based on the full-scale empirical data. Gumbel I distribution was used to fit the daily maximum ice force measured during one winter in various sea areas. The parameters of the asymptotic distribution are assumed to be related to the winter maximum ice thickness, also taking into account the equivalent thickness of ridges. Based on this relationship, the life time load characteristics are evaluated on the basis of the published data of maximum ice thickness during a long time period. The approach was applied to the chemical tanker M/S KEMIRA of ice class IA Super. The most probable extreme forces for the bow frame as a function of return period were presented in Figure 14 of the original paper, and are shown here in Figure 3.20.

In order to compare the icebreaking data with those of the Canadian arctic ships, conversion of the probability distribution to the same format (i.e. the *pdf* of yearly maximum) is needed. We begin this by examining the return period T, curve for the Bothnia Bay. The curve can be represented by the following:

$$T = \frac{T_0}{1 - F(y_n)} , \tag{3.40}$$

where

$$F(y_n) = \exp(-\exp(-c(y_n - u)) , \tag{3.41}$$

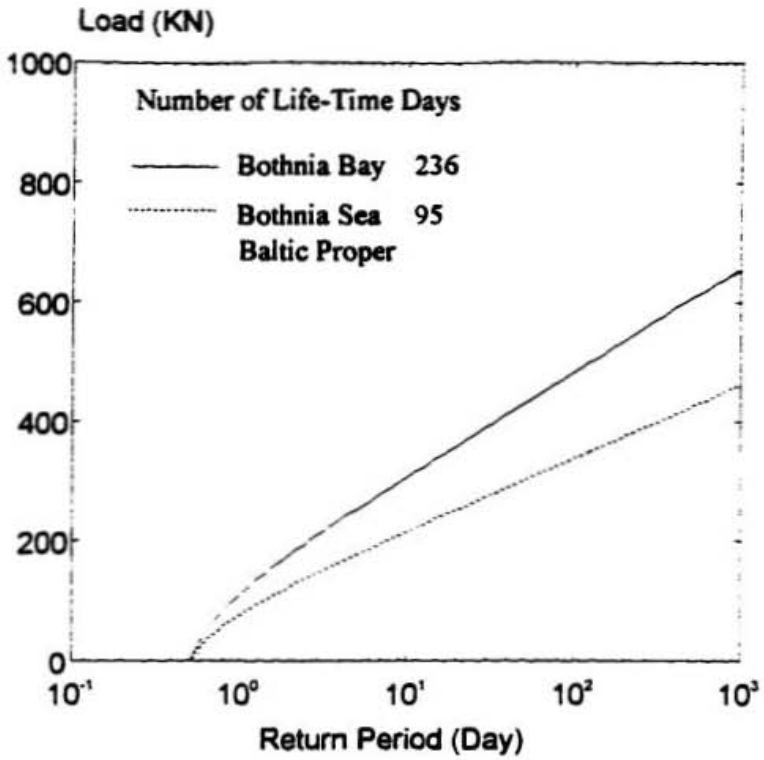

Figure 3. 20 The most probable extreme loads obtained as a function of days in ice in various sea area for the bow frame (FFR2) (From Kujala, 1991, Figure 14)

and T_0 represents the unit time for measured maximum load, a half day (0.5) was used in Kujala (1991). In Equation (3.41) u is a characteristic largest value and c is an inverse measure of the dispersion of the measured maxima. In the present analysis, c and u are calibrated based on the curves presented in Figure 3.20. Choosing two points on the curve, ($T=1000$, $y_n=660$) and ($T=1$, $y_n=105$), substituting them in to Equation (3.40) with manipulations yields:

$$c = 0.0130, \tag{3.42}$$

$$u = 76.88 \ . \tag{3.43}$$

In the following, we transform the distribution of maximum force y_n, (Equation (3.41), into the distribution for the maximum local pressure x_n . Assuming that ice and ship hull contact through a continual ice belt of a height h (0.3 m was used in Kujala, 1991), the local pressure can be expressed in terms of the maximum force:

$$x_n = \frac{y_n}{1000hs} \quad \text{(MPa)} \tag{3.44}$$

where $s = 0.35m$ is the frame spacing and the constant 1000 converts pressure unit kPa to MPa. Note that the local pressure described above is the design pressure, which is different from the pressure measured in critical zones. The latter is much higher and is confined to much smaller area. Substituting Equation (3.44) into Equation (3.41) with manipulation yields:

$$F(x_n) = \exp(-\exp(-(x_n - x_0)/\alpha)) \ , \tag{3.45}$$

where

$$\alpha = \frac{1}{1000shc} \ , \tag{3.46}$$

$$x_0 = \frac{u}{1000sh} \ . \tag{3.47}$$

Equation (3.45) gives the maximum local ice pressure on a half day basis. Assuming that the ship travels in the Bothnia Bay for a number of n unit times (half days) in a year, the yearly maximum pressure can be then derived, according to the extremal theory, as:

$$G(z) = F(z)^n = \exp(-\exp(-(z - x_0 - x_1)/\alpha)) \tag{3.48}$$

where $G(z)$ is the *cdf* of z and z is the yearly maximum pressure and $x_1 = \alpha \log(n)$.

3.5.2 Comparison of the Different Duration of Interactions

In the following, we compare the probabilistic distributions of ice loads for the icebreaking in the Baltic and the ship ramming with arctic multiyear ice. The yearly maximum ice pressure derived above was plotted in terms of probability density in Figure 3.21 for different values of n for a contact area of 0.1 m^2. Note that the number of ice navigation days for the life time (20 years) in Figure 3.20 for Bothnia Bay was 236, which suggests that the yearly ice navigation time is 11 days, yielding n = 22. The probability distributions for a similar ship in the Arctic are calculated using the results reviewed in Section 3.3 and are plotted in Figure 3.21. The variance of local pressure on Canadian arctic ships is much higher than that of the Baltic ships. This result is consistent with the arguments presented in Figure 3.18. The design ice loads according to the Finish Rules and for the *ASPPR Proposals* are also plotted in Figure 3.21. The local pressure for the Canadian Arctic Class ships is much higher than that of the Baltic ships.

3.6 Concluding Remarks

Critical zones were considered as essential elements in the ice-ship interaction process. The total ice force on a design area was assumed to be applied through a number of critical zones, superimposed on a background pressure. Some critical zones could be

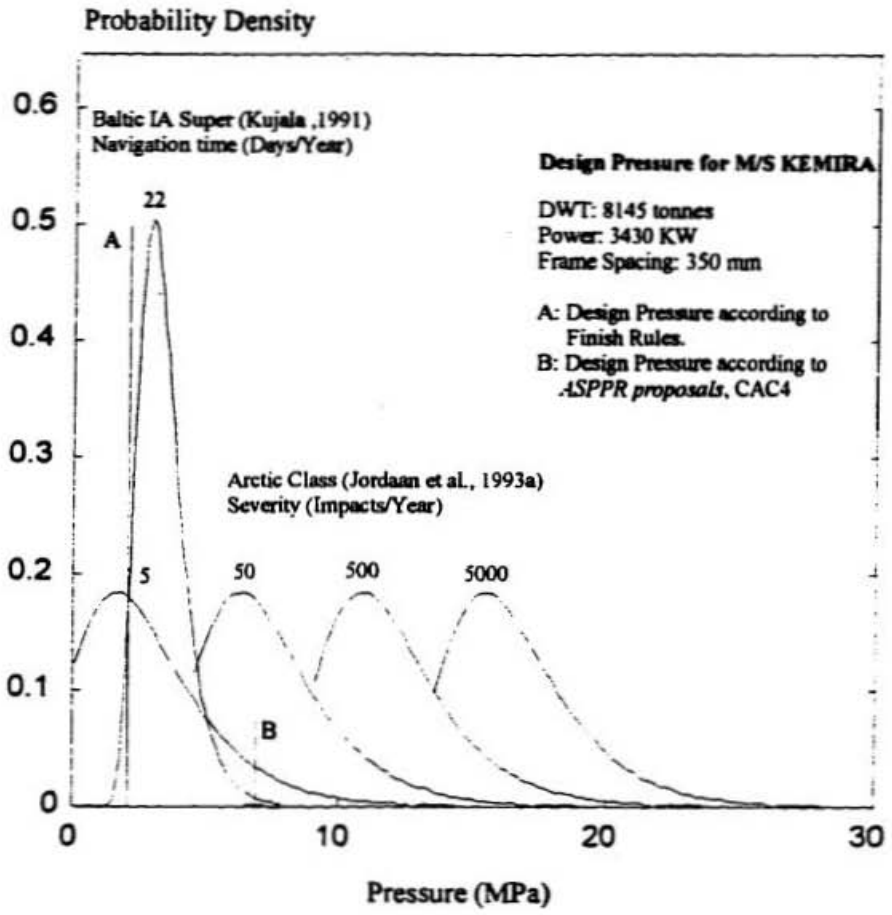

Figure 3. 21 Comparison Between Canadian Arctic Class and Baltic Class

located on the border of a design window and only a portion of its force is inside the design window. To investigate this uncertainty, two approaches, namely *approaches A* and *B*, were proposed. Calibration of the parameters of critical zones from ship trial data was also difficult due to the limit in size of instrumented panel and the spatial resolution of pressure sensors. Two assumptions were made in the calibration. Since the force near the edge is negligible from the view point of structural response, and to be consistent with the

previous analysis by Jordaan et al. (1993a), *approach A* is recommended for the modelling of critical zones.

Probabilistic models are proposed for the critical zones. Assuming that the total force on a design area is a compound Poisson process with an exponentially distributed zonal force, the probability distributions of the ice pressure are derived, using Monte Carlo simulations, for different design areas. The tails of the distributions are well approximated by the exponential distribution and the parameters for this distribution are derived. The probability distribution for the maximum local ice load per ram is derived from the results of the model of critical zones.

The spatial resolution of the pressure sensors and the size of the instrumented panel for the Louis St. Laurent data are limited. A further analysis of ramming data from other ships such as the Polar Sea would be beneficial to the present analysis. This is beyond the scope of present work. The ice pressure for certain design conditions (number of rams per year) can be obtained following a procedure employed in a previous analysis by Jordaan et al., (1993a).

Effects of exposure are discussed with emphasis on the length of the interactions. The probabilistic distributions of the local ice pressure for two extreme cases, namely the ice ramming in the Canadian Arctic and the icebreaking in the Baltic, are examined. The ice pressure for the ice ramming in the arctic is much higher, with a larger variance, than those of the Baltic ships.

Chapter 4

Structural Strength

4.1 Introduction

The structure of a ship's hull is a complex combination of plating, stiffeners and supporting frames. The plating together with the stiffeners make up a stiffened plate. The stiffened plate together with the supporting frames and stringers compose a larger panel (or a grillage). Consequently, the complete vessel can be modelled structurally as a collection of interconnected and interacting panels. In general, there are two kinds of ship structures, namely transverse and longitudinal structures, which have transverse and longitudinal frames, respectively.

There are three levels of loading and responses associated with a ship structure. First, the plating deflects relative to the stiffeners and transfers the load to stiffeners; second, the stiffeners act as beams to carry the load to the boundaries such as supporting web frames or stringers; third, the supporting web frames and stringers yield and the entire panel deflects, transferring the load to the bulkheads and decks.

The complex structural combination and the associated response to the applied load make it desirable to divide the structural strength into three components. These are primary, secondary and tertiary (Paulling, 1988). The primary, or global, strength is con-

concerned with the hull girder. For this classification, the hull is treated as a free-free beam. The major strength members of the hull girder are longitudinal members extending over half of the ship length such as the main deck and the keel. Loads affecting the hull girder are generally global impact loads. An example is the maximum bow force resulting from the collision between the ship hull and an ice feature. The secondary, or semi-local strength is concerned with the strength of a large plate panel (or grillage), generally taken between two stringers or bulkheads or deep web frames. The tertiary, or local, strength is concerned with the strength of plating between two stiffeners or two frames. This region must resist localized ice loads, especially the critical zones that resulted from the ice failure mechanism described in Chapters 2 and 3. This region is of importance in the design of plating and is the focus of the present study.

Figure 4.1 schematically shows a transverse structure subjected to ice impact loads. The ice loads are highly localized within critical zones, which move from place to place and change in intensity. The responses of the structure are very complicated. The figure also shows two idealized cases. First, the ice load is uniformly distributed between two frames. The plating can be modelled as a long plate loaded by uniform pressure (referred to as the long plate model). This idealization is used in *the ASPPR Proposals*. Second, the ice load is applied through an "ice belt", within which the ice pressure are uniform (here, referred to as the patch load model). The second idealization is close to reality when the ice features are first year. This is used in the formulation of the Finish-Swedish Ice Class Rules (1989).

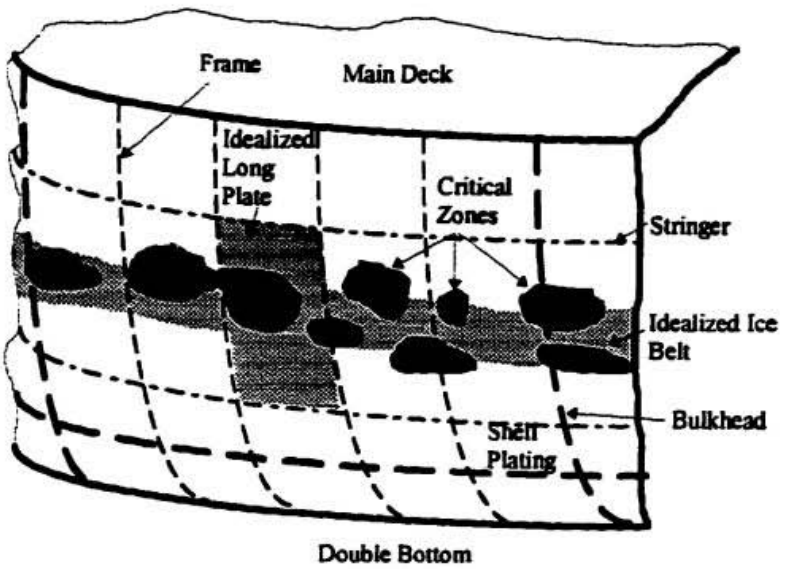

Figure 4. 1 A Ship Panel Subjected by Ice Impact Loads

The long plate model and patch load model are easy to implement in design. Since the realities are much more complicated, there are uncertainties associated with these two models. First, the design loads are different from real ones; second, the modelled responses are different from the real structural deformations. Understanding of these uncertainties are vital in calibrating a design rule such as *the ASPPR Proposals*.

In this chapter, the long plate model is reviewed in detail. In particular, three failure mechanisms, i.e., three-hinge mechanism, permanent set and rupture, will be analyzed. The patch load model will be analyzed using the yield-line theory. This analysis is limited to plastic collapse. Other mechanisms are considered later in a finite element analysis. A

analysis. A plate panel, loaded by critical zonal forces is analyzed using the finite element method. Typical load cases are analyzed. More loading scenarios will be generated from the statistics of critical zones and be analyzed using the finite element method (FEM) in Chapter 5. The design strategy for plating is discussed, with focus on associating the design ice load in the design model to the yearly maximum ice load, which can be predicted by the method presented in Chapter 3.

We begin our analysis with the long plate model.

4.2 The Long Plate Model

We define the long plate model as a long plate loaded by uniform pressure. Usually, this plate fails in three limit states, namely plastic collapse, permanent set and ultimate rupture. The plastic collapse is defined as the formation of three hinge mechanism and results when the plate is assumed to have no in-plane resistance against the load. With fully supported, ductile steels, this mechanism is the onset of minor denting. Permanent set is defined (Hughes, 1988) as the deflection of a plate involving plastic bending strain along its boundaries, i.e., frames and stringers. The edge hinges are responsible for the commencement of the permanent set. Plastic collapse and permanent set relate to the serviceability of the ship. Ultimate rupture is defined as reaching the maximum membrane capacity of the plate. This relates to the safety of the ship. There is considerable reserve of strength beyond the three hinge limit in steel plating provided membrane effects can occur. Reliance on membrane action assumes that the adjoining

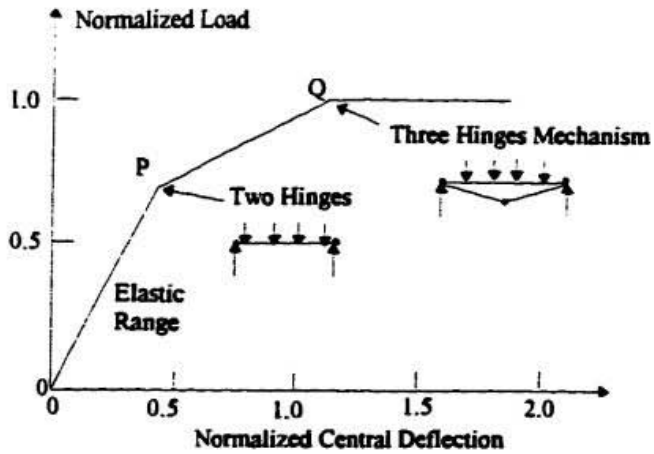

(a) Formations of Two Hinges and Three Hinges

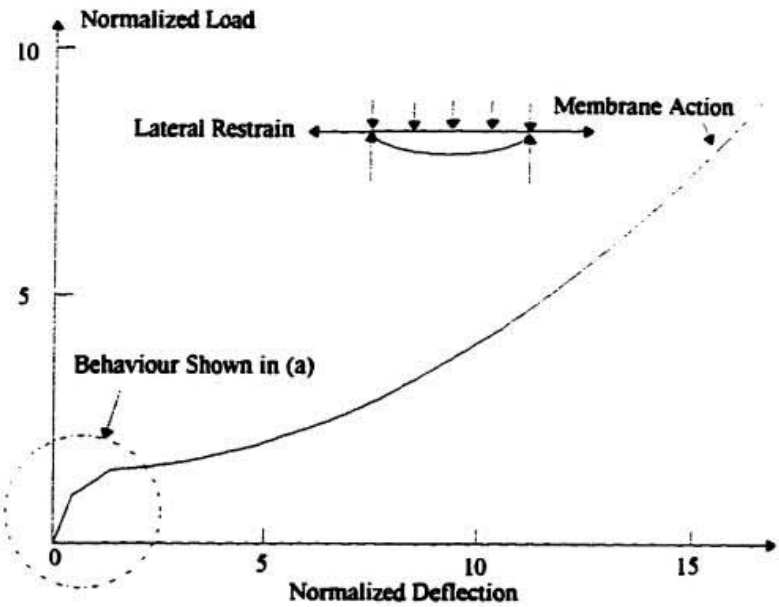

(b) Membrane Action

Figure 4. 2 Schematic Illustration of Plastic Failure Mechanism (based on Carter et al., 1992).

structure provides adequate lateral restraint. This is schematically illustrated in Figure 4.2. We begin our analysis with two-hinge and three-hinge failure.

4.2.1 Two-Hinge and Three-Hinge Failure

Two-Hinge Failure: Figure 4.3 shows a long plate, which is fixed at both ends and loaded by uniform lateral pressure. The plastic hinges form when the bending moments at the edges reach the plastic bending moment:

$$M = -\frac{P_{2H} s^2}{12} = -M_p \ , \tag{4.1}$$

where P_{2H} is the critical pressure for edge hinges, t and s are defined in Figure 4.3 and M_p is the plastic bending moment. For a long plate, using the Hencky-von Mises yield criterion, M_p can be expressed as:

$$M_p = \frac{\sigma_y}{\sqrt{1 - \nu_p + \nu_p^2}} \frac{t^2}{4} \ , \tag{4.2}$$

where σ_y is the yield stress and ν_p is the plastic Poisson's ratio. For steel with $\nu_p = 0.5$, P_{2H} can be derived from equations (4.1) and (4.2) as:

$$P_{2H} = 3.464 \sigma_y \left(\frac{t}{s}\right)^2 \ . \tag{4.3}$$

The corresponding deflection at the midspan, δ_{max}, is:

$$\delta_{max} = \frac{P_{2H} s^4 (1 - \nu^2)}{32 E t^3} \ , \tag{4.4}$$

For $\nu_p = 0.5$ Equation (4.6) becomes:

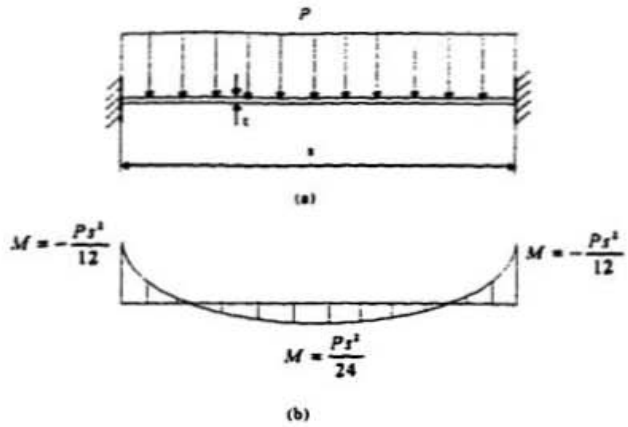

Figure 4. 3(a) Schematic Diagram of a Plate With Fixed Ends and Loaded by Lateral Pressure, (b) Distribution of Bending Moment.

where ν is the Poisson's ratio in elastic range.

Three Hinge Mechanism: Once two edge hinges form, the plate continues to bend until the third plastic hinge forms at the midspan as shown in Figure 4.4. Considering the straight bar mechanism and neglecting the membrane force, the virtual work equation gives:

$$-M_p\frac{\delta}{s/2}-M_p\frac{\delta}{s/2}-M_p\frac{2\delta}{s/2}+2\frac{sP_{3H}}{2}\frac{\delta}{2}=0\ , \tag{4.5}$$

which yields:

$$P_{3H}=\frac{16M_p}{s^2}=\frac{4\sigma_y}{\sqrt{1-\nu_p+\nu^2}}\left(\frac{t}{s}\right)^2\ . \tag{4.6}$$

$$P_{3H}=4.62\sigma_y\left(\frac{t}{s}\right)^2\ . \tag{4.7}$$

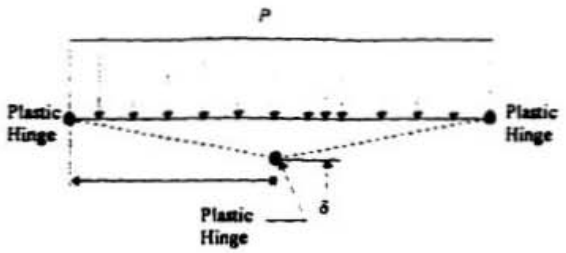

Figure 4. 4 Schematic Diagram of Three Hinge Mechanism.

Serviceability: The deflection at midspan, δ_{max}, can be used as the criterion for the serviceability of the plate. Ayyub et al. (1989) assumed that $\delta_{max} = 2t$ is a reasonable limit for plating. Daley et al. (1991) suggest that $\delta_{max} = 0.1s$ is a reasonable limit state. Brown (1993) showed that using $\delta_{max} = 2t$ results in plate thicknesses that are too thin for stiff (high t/s ratios) plates while taking $\delta_{max} = 0.1s$ results in thin plate thickness for less stiff plates. As a result, a blended function was proposed. For simplicity, the three-hinge collapse (Equation 4.7) was used as the limit state of serviceability in the present study. This is consistent with a study by Nessim et al. (1992) but it could be conservative as suggested by Brown (1993).

4.2.2 Membrane Action and Ultimate Rupture

Once three plastic hinges form, the plate begins to collapse. This collapse is, however, restrained by the membrane force due to the fixed boundaries. Ignoring the flexural stiffness of the plate (assuming pure membrane action), the equilibrium condition gives (see Figure 4.5):

$$\frac{Ps}{2}x - \frac{Px}{2} - \delta_x F_H = 0 \ , \tag{4.8}$$

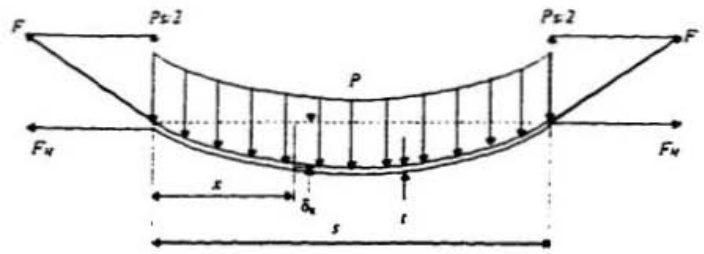

Figure 4. 5 Schematic Diagram of Membrane Action

where δ_x and F_H are the deflection at x and the horizontal component of the membrane force, respectively (see Figure 4.5). The maximum deflection at midspan can be obtained by substituting $x = s/2$ into Equation (4.8):

$$\delta_{max} = \frac{Ps^2}{8F_H} . \tag{4.9}$$

Based on Equations (4.8) and (4.9), Ratzlaff and Kennedy (1985) derived the load as a function of the deflection at midspan for elastic membrane action as follows:

$$P = \frac{64}{3}\left(\frac{\delta_{max}}{s}\right)^2 \frac{Et}{(1-\nu^2)} \frac{1}{\sqrt{s^2+(4\delta_{max})^2}} , \tag{4.10}$$

where ν is the Poisson's ratio.

When the load reaches the yield limit and the full plastic membrane action is developed, the relationship between the uniform pressure and the deflection at midspan can be derived as:

$$P = \frac{8\sigma_y t\delta_{max}}{\sqrt{1-\nu_p+\nu_p^2}} \frac{1}{s\sqrt{s^2+(4\delta_{max})^2}} . \tag{4.11}$$

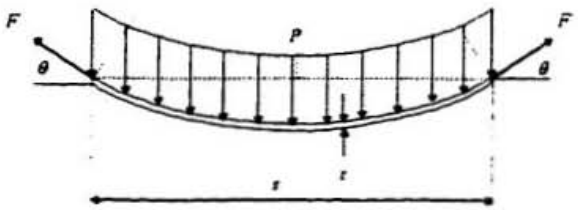

Figure 4. 6 Schematic Diagram of Membrane Action Failure Mechanism.

Assuming full plastic membrane action and that the deflected plate is a circular arc (see Figure 4.6), Nessim et al. (1992) derived the equilibrium equation as:

$$2F\sin\theta = Ps\,. \tag{4.12}$$

The shape of a circular arc gives:

$$\frac{\sin\theta}{\theta} = \frac{\pi}{180(1+\varepsilon_s)}\,, \tag{4.13}$$

where ε_s is the nominal membrane strain in the plate at rupture and ε_s=0.05 was suggested by Egge and Böckenhauer, (1991) and McDermott, et al., (1974). Substituting ε_s=0.05 into Equation (4.13) gives θ=31°. Substituting this value of θ into Equation (4.12) and rearranging gives:

$$P_u = \frac{2F_u\sin(31°)}{s} = \frac{1.03F_u}{s} \tag{4.14}$$

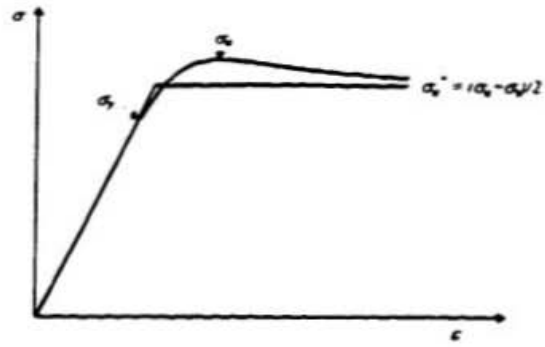

Figure 4. 7 Mechanical Properties of Material

where $F_u = \sigma_y^* t$ is the membrane force which corresponds to the ultimate rupture and $\sigma_y^* = (\sigma_y + \sigma_u)/2$ for an elasto-plastic material was suggested by Nessim et al., (1992) (see Figure 4.7). Substituting F_u into Equation (4.14) gives:

$$P_u = 0.515(\sigma_Y + \sigma_u)\left(\frac{t}{s}\right)^2 , \tag{4.15}$$

and the corresponding deflection at midspan:

$$\delta_{max}^* = 0.1679s . \tag{4.16}$$

Equation (4.15) was derived by Nessim et al. (1992) as the criterion for the ultimate strength of the plating.

4.2.3 Finite Element Analysis of A Long Plate

In the following we analyze the response of a long plate illustrated in Figure 4.3 (a), using the finite element method. Particulars of the plate are determined from a design in Chapter 6 and are given in Table 4.1.

Table 4. 1 Particulars of the plate beam

Plate Thickness (t)	32 mm
Plate Span (s)	600 mm
E	190 GPa
Steel Grade	EH 36
Yield Stress (σ_Y)	388 MPa
Ultimate Stress (σ_U)	537 MPa

The analysis was carried out using the finite element package ABAQUS. We assume that the material is bilinear as illustrated in Figure 4.7, and account for the membrane forces by fixing both ends of the plate. This boundary condition will ensure the membrane effect in both elastic and inelastic range. Figure 4.8 shows a section of the deformed plate when loaded by an uniform pressure of 33.6 MPa. The figure also shows the distribution of the principal strains. Rupture is most likely to occur near the support where the principal strain reaches 25%, a value suggested by Shackelford, (1988), for tensile failure of ductile steel. The average strain across the span is 5%. This value corresponds to the nominal membrane strain at rupture reported by Egge and Böckenhauer, (1991) and McDermott, et al., (1974). In the present analysis, we use 5% average strain as the criterion for ultimate rupture.

The pressure against the deflection at midspan of the plate was evaluated and plotted in Figure 4.9. For comparison, the plate with no lateral restraint at one end was also analyzed. The load-deflection curve is plotted in Figure 4.9. The figure shows that, when lateral restraints exist at both supports, rupture occurs at a pressure much higher

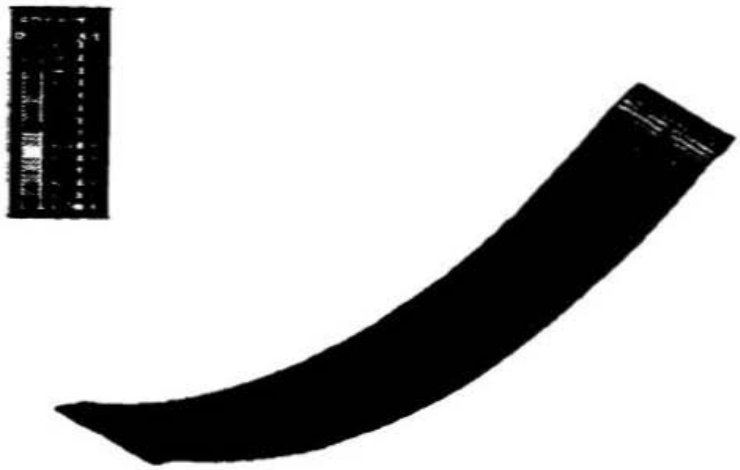

Figure 4. 8 A section of the deflected plate and the distribution of the principal strains.

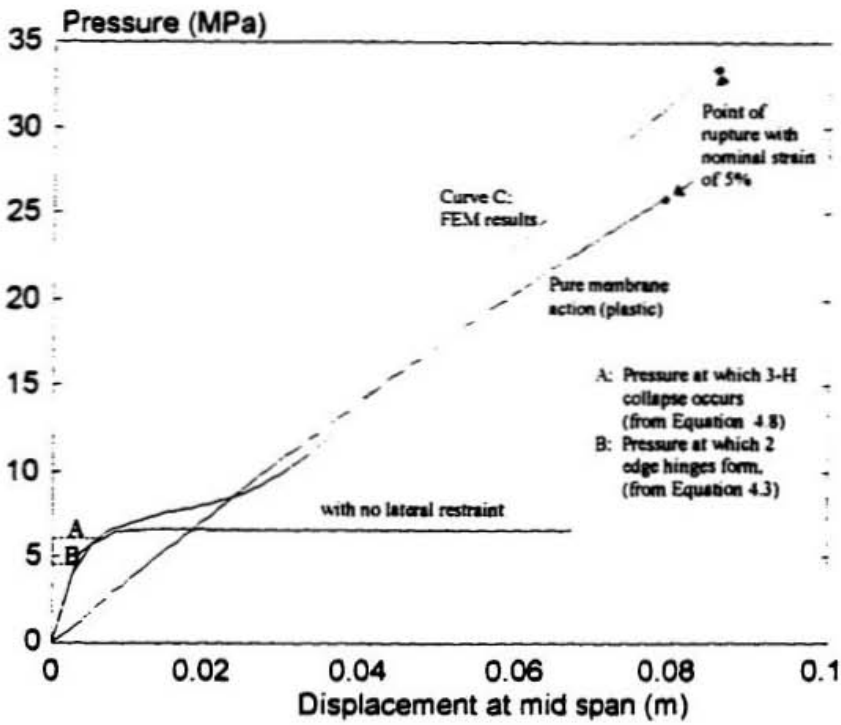

Figure 4. 9 Illustration of Different Failure Mechanism

than that of three hinge collapse. The figure also shows the pressure-deflection for the pure membrane action from equations (4.10) and (4.11). Note from the figure that the model of pure membrane action underestimate the pressure at rupture by a factor of 1.3. This is because the pure membrane action model ignores the flexural resistance. Figure 4.9 also shows the pressures at which 2-hinges and 3-hinges occur from equations (4.3) and (4.7), respectively. The pressure of 3-hinge collapse corresponds to a point on *Curve C* (results of FEM) with maximum curvature of the convex. This point is defined in our finite element modelling as the plastic collapse.

4.3 The Patch Load Model

In this section, I will analyze the response of plating under an idealized load, e.g. ice belt, which is shown in Figure 4.1. I will limit my analysis to the plastic hinge collapse. Membrane action and rupture will be considered later in a finite element analysis.

4.3.1 Model Development

I approximate the plating as a panel with fixed boundaries and loaded by a patch of lateral pressure. This is shown in Figure 4.10. The panel corresponds to the ship plating supported by intersecting stiffeners. The stiffeners can be beams, frames or stringers. I assume that these stiffeners are much more rigid than the plate (especially for a panel in the bow region) and provide sufficient lateral restraint and resistance to rotation at the plate boundaries. The loaded area in Figure 4.10 extends the entire frame spacing and has varying width.

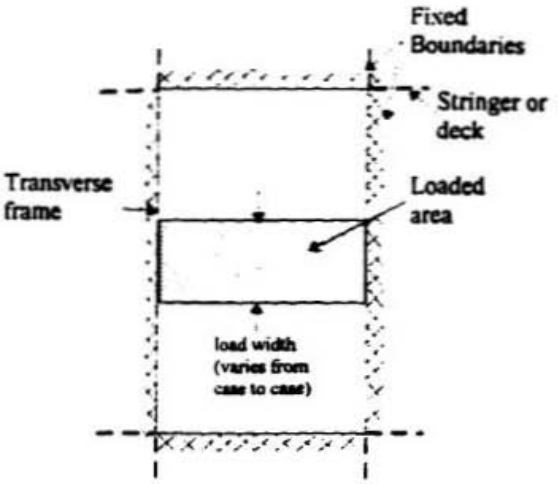

Figure 4. 10 An Idealized Plate Under Lateral Pressure.

Since I am mainly interested in the failure of the plate, I will consider the plate as a perfectly plastic body which does not undergo deformation before the yield condition is reached. The difference between perfect plastic and elasto-plastic behavior is schematically illustrated by the stress strain relations in Figure 4.11. I will use the upper-bound and lower-bound theorems of plasticity which can be enunciated as follows (Baker, 1956):

- Upper-bound theorem: If the work of a system of applied loads with an associated kinematically admissible displacement field (collapse mechanism) is equated to the corresponding internal work, then this system of loads will cause collapse of the structure.

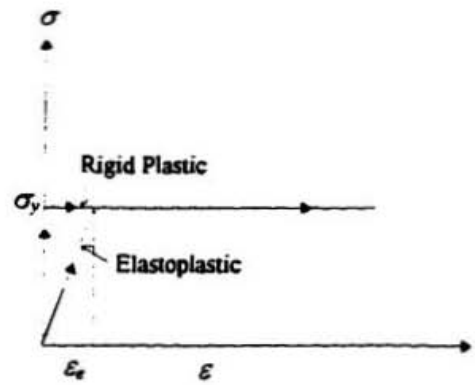

Figure 4. 11 Rigid Plastic Deformation and Elasto-plastic Deformation

- Lower-bound theorem: If a system of generalized stresses can be found that is in equilibrium with the applied loads and that nowhere violates the yield condition, then the structure will not collapse.

The limit analysis solutions can be obtained by either maximizing a lower bound or by minimizing an upper bound. The solutions are approximate ones and provide sufficient accuracy for engineering applications.

In the following, we will use the upper bound theorem to determine the strength of the plate shown in Figure 4.10. I will limit our analysis on the plastic collapse of the plate. I assume that the plate is perfectly plastic as we stated earlier and ignore elastic deformation in the plate. I assume that the panel deforms into a tent shape once the plastic limit is reached as suggested by Wood (1961). In the case that no lateral restraint exists at the boundaries, such a tent shape forms a mechanism of collapse. In our case, the lateral restraint is provided and the formation of a tent shape marks the beginning of large

Table 4. 2β values for different cases.

	β	
case	from	to
case 1	0	$\tan^{-1}((L-H)/s)$
case 2	$\tan^{-1}((L-H)/s)$	$\tan^{-1}(L/s)$
case 3	$\tan^{-1}(L/s)$	$\pi/2$

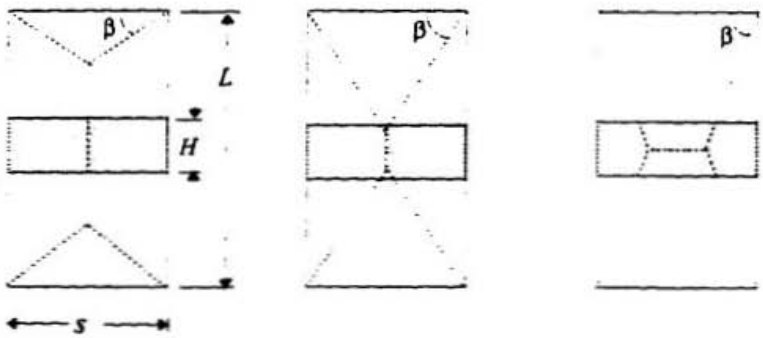

(a) Case 1 (b) Case 2 (c) Case 3

Note: Shaded area represent the uniform lateral pressure.
$l = L/s$, $h = H/s$

Figure 4. 12 Illustration of Three Possible Failure Patterns.

deformations. There are five yield lines inside the plate and four yield lines at the boundaries. Four of these yield lines initiate from the corner and intersect with the one located in the center of the plate. There are three possible failure patterns, designated as cases 1, 2 and 3 as shown in Figure 4.12. The three cases differ from each other by the patterns of the yield lines relative to the loaded area. This can be characterized by the range of β angle given in Table 4.2

Governing Equation: the governing equation for each case can be obtained, according to the upper-bound theorem, by equating the external work of the lateral load to the internal energy dissipated. Assuming that the plastic deformation is localized at n generalized hinge lines, this equation can be expressed as:

$$\int_A pW dA = \sum_{i=1}^{n} (M_0 \theta_i + N_0 \varepsilon_i) l_i \quad , \tag{4.17}$$

where p is the pressure, W is the vertical deflection, ε and θ represent the concentrated elongation and rotation along the hinge line l_i, respectively, and M_0 and N_0 are the full plastic moment and the axial force normal to the hinge line, respectively. For an isotropic plate, they are:

$$M_0 = \frac{1}{4}\sigma_y t^2 \qquad \text{and} \tag{4.18}$$

$$N_0 = \sigma_y t \, , \tag{4.19}$$

where σ_y is the yield stress and t is the thickness of the plate.

Internal Energy: the internal energy due to the deflection of the plate can be derived following Wiernicki (1987). For case 1 and 2, the result is:

$$D = W_0 \left\{ 8M_0 \left[l + \frac{1}{\tan(\beta)} \right] + 2W_0 N_0 \left[2l - \tan(\beta) + \frac{1}{\tan(\beta)} \right] \right\} \quad , \tag{4.20}$$

where D is the total internal energy, $l = L\,s$, W_0 is the maximum deflection at the central hinge line. For case 3, the total energy is:

$$D = W_0\left\{8M_0\left[\frac{1}{l}+\tan(\beta)\right]+2W_0N_0\left[\frac{2}{l}+\tan(\beta)-\frac{1}{\tan(\beta)}\right]\right\} \quad , \tag{4.21}$$

where the parameters are defined as before.

External Work: the external work by the lateral pressure can be obtained by evaluating the integration term in the left hand side of Equation (4.17) and can be derived as:

for case 1,

$$U = pW_0s^2\frac{h}{2} \quad , \tag{4.22}$$

for case 2,

$$U = pW_0s^2f_2(h,l,\beta) \quad \text{and} \tag{4.23}$$

for case 3,

$$U = pW_0s^2f_3(h,l,\beta) \quad , \tag{4.24}$$

where U is the total external work, W_0 is the maximum deflection at the middle hinge line, p is the uniform pressure in the loaded area, s and β are defined in Figure 4.5. Parameters $h = H/s$ and $l = L/s$ in Equations 4.7 to 4.8 are normalized dimensions shown in Figure 4.5 and $f_2(h,l,\beta)$ and $f_3(h,l,\beta)$ are functions of h,l and β and are given below:

$$\begin{aligned} f_2(h,l,\beta) = \quad & \frac{1}{\tan^2\beta}\left\{\frac{1}{6}(\tan\beta-l+h)^2\left[\tan\beta+2(l-h)\right]+\frac{1}{2}(l-h)^2h+(l+h-\tan\beta)\right. \\ & \left.(\tan\beta-l+h)\left[\frac{(\tan\beta-l+h)(2l+h-2\tan\beta)}{6}+\frac{1}{2}(b-h)\right]\right\} \end{aligned} \tag{4.25}$$

$$f_3(h,l,\beta) = \frac{h}{l\tan\beta}\left\{\frac{1}{2}(l-h)^2 + h\left(\frac{l}{2}-\frac{h}{3}\right) + (2\tan\beta - 2l + h)\left[\frac{1}{6}\frac{h(3\tan\beta - 3l + 2h)}{(2\tan\beta - 2l + h)} - \frac{1}{2}(l-h)\right]\right\} \quad (4.26)$$

Solutions: by equating the external work to the internal energy, the pressure for plastic collapse can be derived as:

for case 1:

$$p = \frac{2}{s^2 h}\left\{8M_0\left[l + \frac{1}{\tan(\beta)}\right] + 2W_0N_0\left[2l - \tan(\beta) + \frac{1}{\tan(\beta)}\right]\right\}, \quad (4.27)$$

for case 2:

$$p = \frac{1}{s^2 f_2(h,l,\beta)}\left\{8M_0\left[l + \frac{1}{\tan(\beta)}\right] + 2W_0N_0\left[2l - \tan(\beta) + \frac{1}{\tan(\beta)}\right]\right\}, \quad (4.28)$$

and for case 3:

$$p = \frac{1}{s^2 f3(h,l,\beta)}\left\{8M_0\left[\frac{1}{l} + \tan(\beta)\right] + 2W_0N_0\left[\frac{2}{l} + \tan(\beta) - \frac{1}{\tan(\beta)}\right]\right\}. \quad (4.29)$$

Once the expressions of pressure at collapse (Equations 4.27 to 4.29) are obtained, the actual pattern of plastic collapse can be derived by minimizing p with respect to β:

$$\frac{\partial p}{\partial \beta} = 0, \quad (4.30)$$

and the corresponding minimum pressure causes the collapse of the plate. Tentatively we designate this pressure as the strength of the plate, p_s.

A theoretical evaluation of Equation (4.30) is very tedious and sometimes impossible. Instead, a numerical evaluation is more convenient. In the present study, Equations (4.20) to (4.30) were implemented in a computer program using **matlab** and the results are presented in the following section.

4.3.2 Results

In the following, we use the model developed in the preceding section to examine the response of a plate with different aspect ratios ($l = L/s$) and with different width of loaded area ($h = H/s$). The pressure, p, is normalized with respect to the frame spacing and the full plastic moment (ps^2/M_0). Figure 4.13 shows the variation of normalized pressure against β values at $l = 2$ and $h = 1.8$. As indicated by the figure, the pressure is minimum in case 2 and corresponds to a β value of 52 degrees. This minimum pressure corresponds to the solution of Equation (4.30) and is designated as strength p_s. In Figure 4.14, values of p_s for different aspect ratios and different load widths are presented. As shown in the figure, p_s converges to the one way action of three hinge mechanism (equivalent to a plain strain beam). To investigate the effect of membrane force, we impose a deflection , W_0, at the midspan. This deflection provides a membrane effect therefor increase the strength of the plate. The strength p_s against W_0 (normalized with respect to plate thickness) are plotted in Figure 4.15.

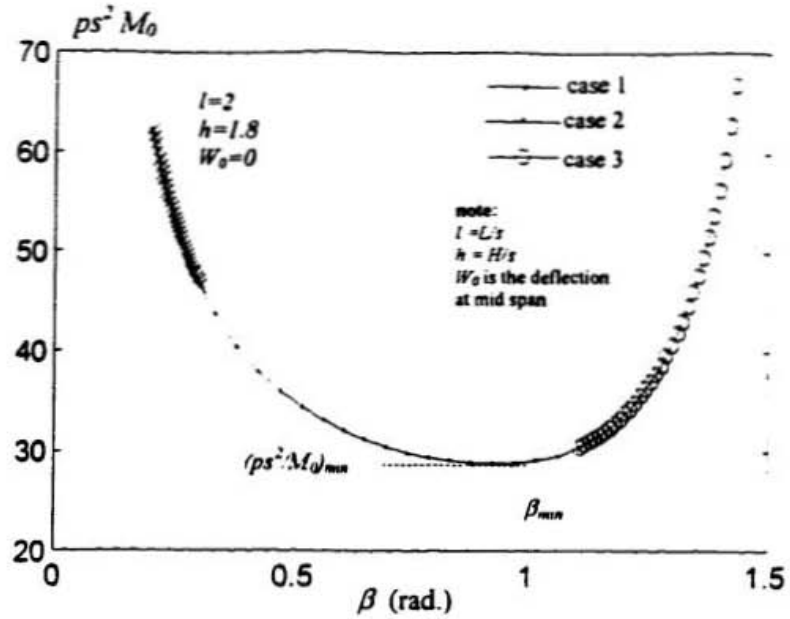

Figure 4. 13 Variation of Normalized Pressure at Collapse against β

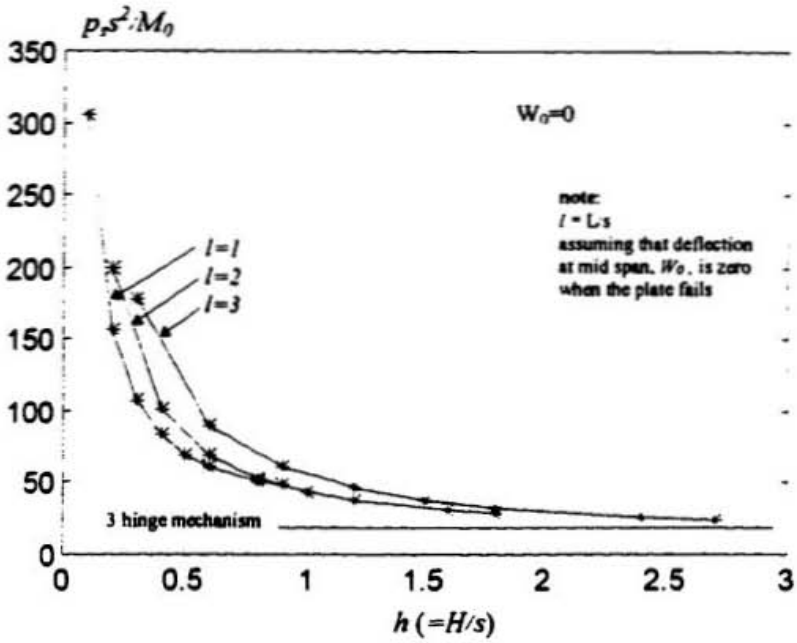

Figure 4. 14 The Normalized Strength of the Plate with Different Loaded Width.

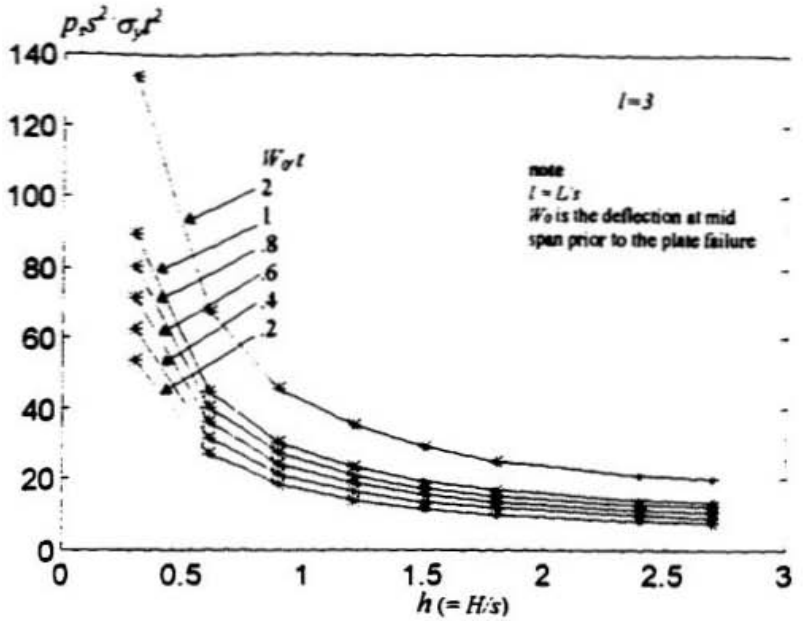

Figure 4. 15 Normalized Strength for Different Deflections at Midspan Prior to Failure

4.3.3 Finite Element Analysis

In this section I analyze the plate panel of Figure 4.10 using the finite element method. Particulars of the panel are chosen based on an example design in Chapter 6; they are : $s = 0.6$ m, $L = 1.2$ m and $t = 32$ mm. Four load widths are used in the analysis. They are: $H = 0.2$, 0.3, 0.5 and 1.2 m, respectively. Figure 4.16 shows the deformed panel at plastic collapse for $H = 0.3$ m. Note the deformation of the plate is more localized in the central region compared with the roof shape suggested in Figure 4.12. Pressure against displacement at midspan are plotted in Figure 4.17. Pressures at plastic failures are identified. These loads are plotted together with the results from the yield line model (Equations 4.27 to 4.30). The results are shown in Figure 4.18. Note that the pres-

pressure predicted by yield line theory is higher than that of the finite element results. This is because the yield line model assumes that the deformed shape of the panel is a roof shape, which over-estimated the true deformation. The real deformation of the panel is more localized in the central region.

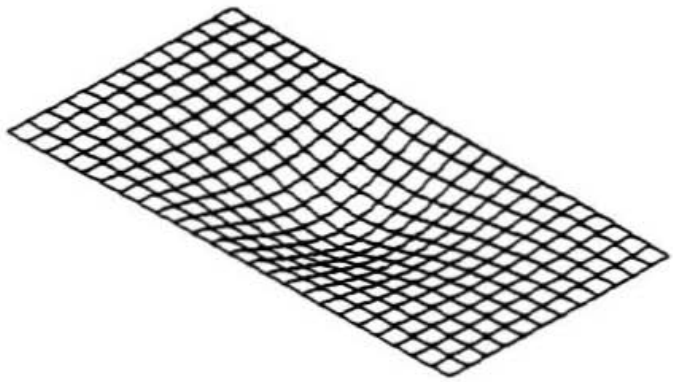

Figure 4. 16 Deformed panel (H = 0.3 m)

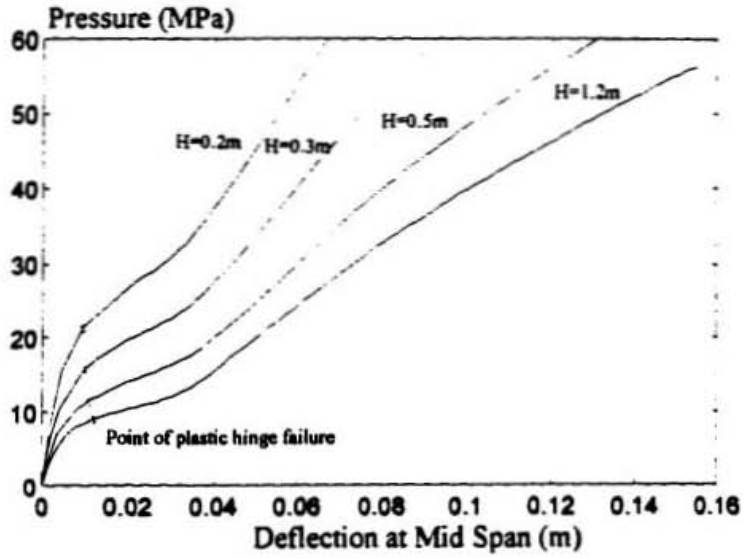

Figure 4. 17 Pressure vs. displacement at midspan

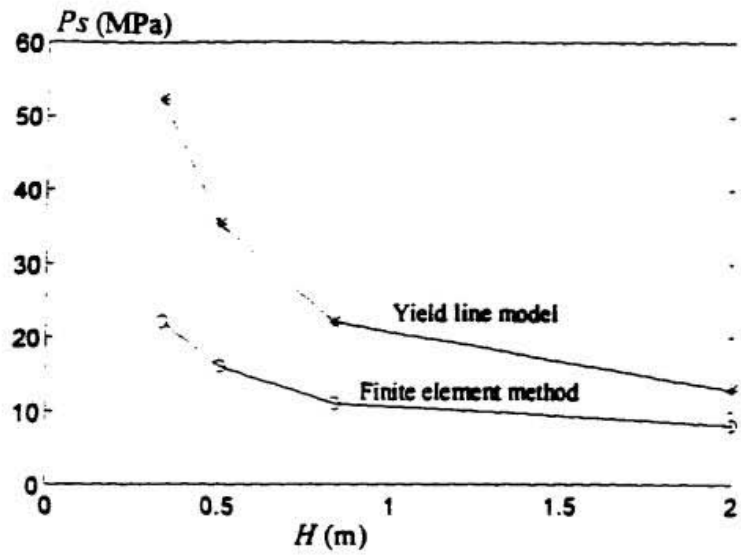

Figure 4. 18 Strength at various load widths

4.4 *Structural Response to Critical Zonal Forces*

In this section, we use the finite element method to analyze the response of a plate panel to critical zonal forces. The panel is shown in Figure 4.19. Particulars of the panel are: s = 0.6 m, L = 1.2 m and t = 32 mm. Material properties of the steel are given in Table 4.1. The loads on the panel are applied through a number of critical zones, which are modelled using squares of uniform pressure. They are shown schematically in Figure 4.19. The number of critical zones could be one, two or many. In this section, we investigate typical cases with one, two and three critical zones. More load cases are generated in Chapter 5 from statistics of critical zones and analyzed by the finite element method.

First, we examine the case in which one critical zone, with an area of 0.09 m^2, is located at the center of the panel (Case 1 in Figure 4.20). Figure 4.21 shows the deformed panel when the pressure in the critical zone reaches 72 MPa. The figure also

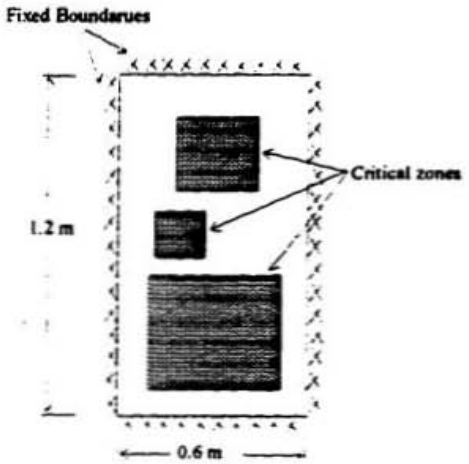

Figure 4. 19 A plate Panel Loaded by Critical Zonal Forces

shows the distribution of the principal strains. Note that the maximum deformation occurs at the mid section (A-A), when the average membrane strain reaches the limit of 5%. This is the section where plastic collapse and rupture initiates and is referred to, in the present analysis, as the **dominant section**. Such a section fails in a way similar to that of a long plate, loaded by strip loads (e.g., see Case 4 in Figure 4.20). We refer to this plate as the equivalent long plate. An equivalent long plate, (Case 4 in Figure 4.20) is also analyzed. The width of the strip is the same as that of the critical zone. The maximum strain occurs near the support, which is the same as the dominant section of the panel. The average strain over the span reaches 5% at a pressure value of 46 MPa, which is lower than that of the dominant section. The difference is caused by the lateral supports of the panel. The

pressure against the displacement at midspan is plotted in Figure 4.22 for both cases. Plastic hinge collapse occurs at 16 MPa and 8 MPa for the dominant section and the long plate, respectively. To simplify analysis, the dominant section of Case 1

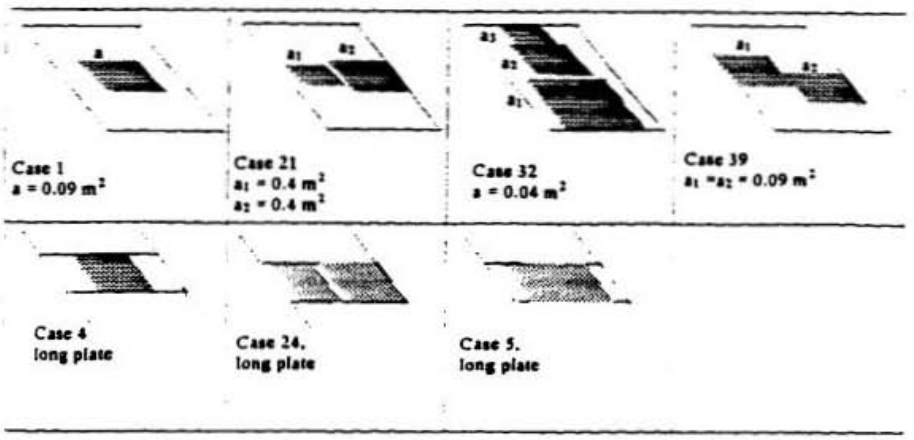

Figure 4. 20 Selected Load Cases

can be analyzed by the long plate model, Case 4, with modification factors accounting for lateral support. Factors affecting the lateral support include the size and the location of critical zone, which are investigated in more details in Chapter 5.

For the case of two critical zones or more, the structural response is more complicated. Critical zones may be aligned on the dominant section (Case 21), along the frames (Case 32) or adjacent to, or overlap each other (Case 39). Figures 4.23 to 4.25 show the deformed panel and distribution of principal strains for Case 21, Case 32 and Case 39, respectively. For Case 21, the plate fails at the dominant section. The dominant section may be approximated by the long plate in Case 24. For Case 32, the dominant section is located within the critical zone a_1. In addition to lateral support, the failure of the section is also affected by the presence of other critical zones a_2 and a_3. Such effects are investi-

are investigated in detail in Chapter 5. Case 39 is more complicated. It can be approximated in the way of Case 21 or 32, depending on the extent of overlap, which is also investigated in details in Chapter 5.

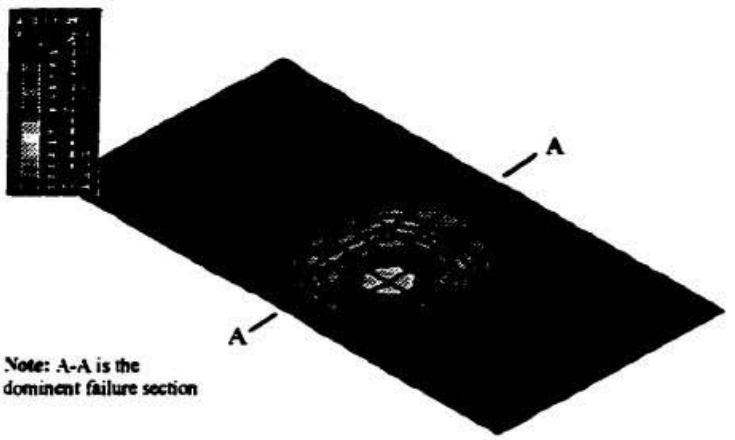

Figure 4. 21 Deformed panel, showing contours of principal strains (Case 1)

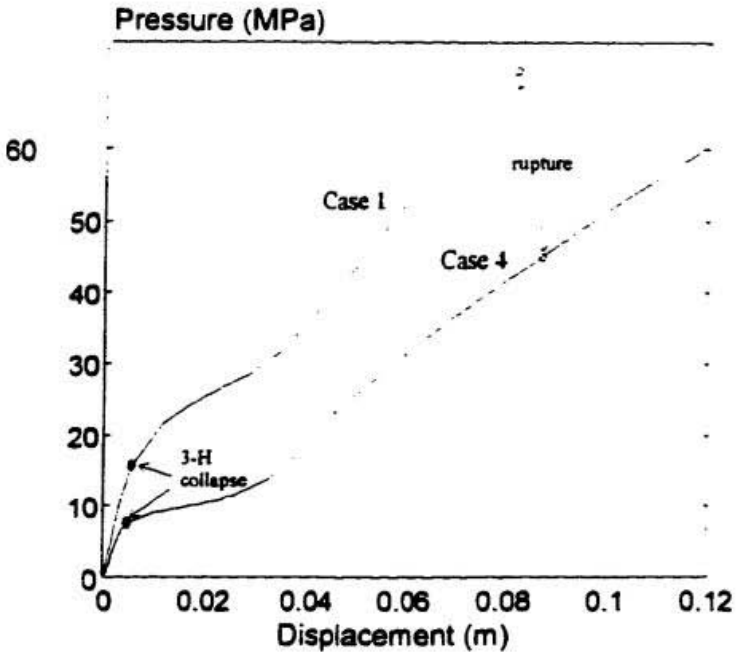

Figure 4. 22 Pressure vs. Displacement at midspan

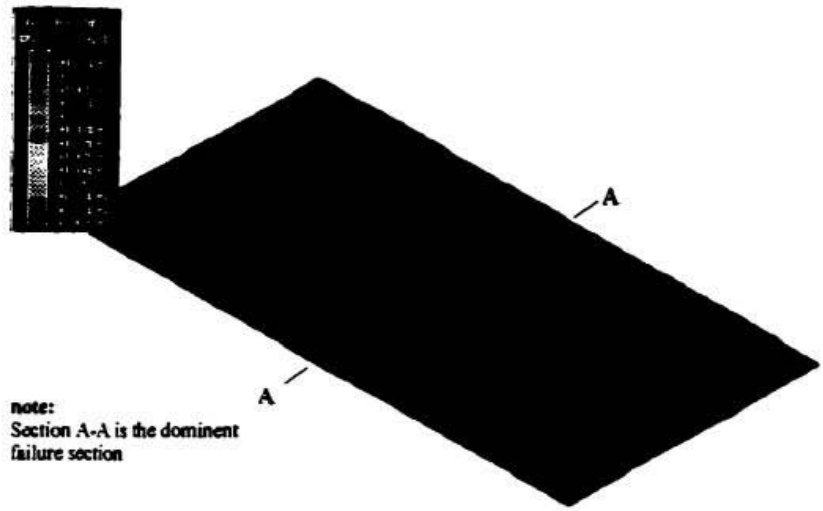

Figure 4. 23 Deformed panel and distributions of principal strain (Case 21)

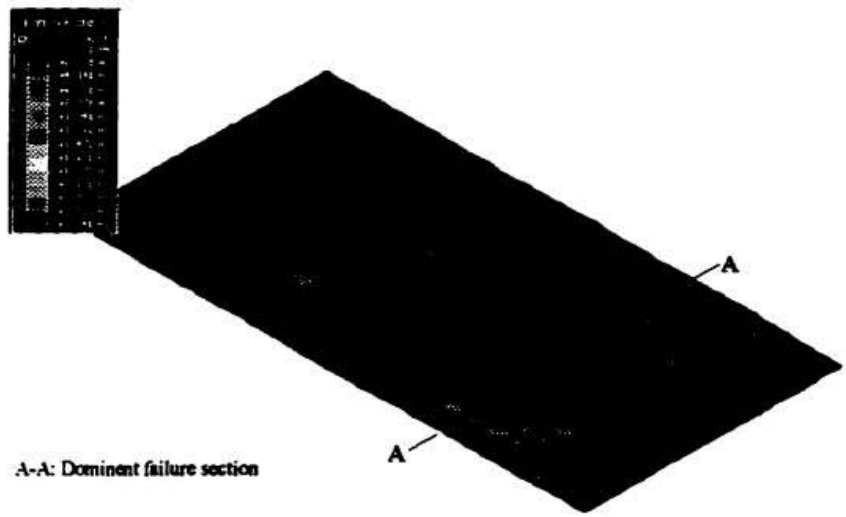

Figure 4. 24 Deformed panel and distributions of principal strain (Case 32)

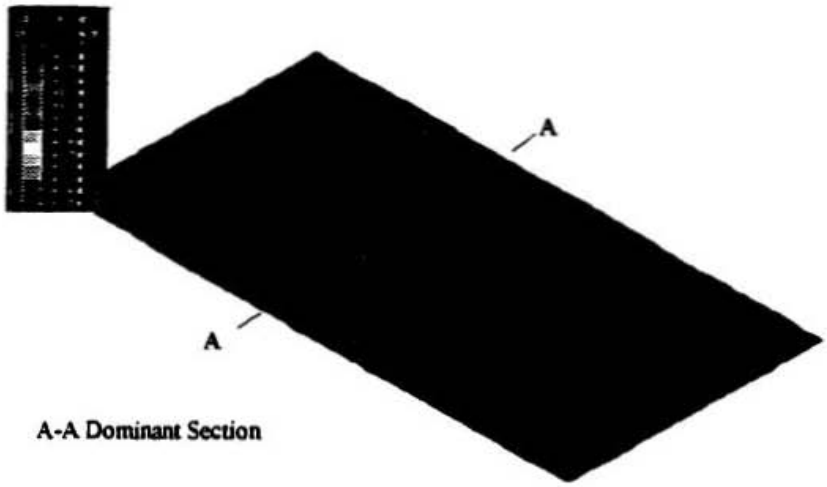

Figure 4. 25 Deformed panel and distributions of principal strain (Case 39)

4.5 *Design Strategy*

In the preceding section we concluded that a plate usually fails in a dominant section, which can be approximated by a long plate. For simplicity, in practical design, the load is considered uniform. This results in uncertainties in the design model, which will be investigated in Chapter 5. The long plate model is easy to implement in a rule based design and was used in design codes such as the *ASPPR Proposals*. In the *ASPPR Proposals*, the plate thickness was derived based on the two-hinge mechanism. The most recent revisions to *ASPPR Proposals* (Carter et al., 1996) proposed a design ice load as:

$$DPP = AF \times CF \times OF \times (6.4 + (0.044 \times (D^{0.7} + D^{0.48} \times P^{.33}))) / s \qquad (4.31)$$

where DPP is the design pressure in MPa, AF, CF and OF are area, class and frame orientation factors, respectively. In Equation 4.31, D is displacement in kilotonnes, P is the engine power in megawatts, and s is the frame spacing. The most sensitive parameter for

for design pressure is the frame spacing. Design pressures against frame spacing for three arctic class CAC1 ships are plotted in Figure 4.26.

Carter et al., (1992) suggest that the design load proposed in the *ASPPR Proposals* corresponds to the average value of the yearly maximum ice pressure. Recall that the probability distribution of yearly maximum ice load can be approximated by a double exponential form Equation (3.13), and the corresponding average of yearly maximum pressure is:

$$\bar{x} = \alpha(\ln(n) + \ln(r) + .577) \tag{4.32}$$

where α is dependent on the design area (see Equation 3.9), n is the number impacts per year and r is the proportion of hits. Suggested value of n for CAC 4 is 10000 and r is 0.46. To explore the relationship between the proposed design pressure (Equation 4.31) to the yearly maximum (Equation (4.32), we calculate the yearly maximum pressure on plate panels with different aspect ratio. Average maximum ice pressures for plate panels with different aspect ratios are plotted against frame spacing in Figure 4.26. Note the average of the yearly maximum for the panel with an aspect ratio of 1.5 matches well with the proposed design values. To be consistent with the present design rules, it is suggested that the yearly maximum ice load be estimated based on a design area of $s \times 1.5s$, where s is the frame spacing. The limit state can be plastic collapse or rupture. For the first, the average of the yearly maximum load should be used as the design pressure. For the latter case, the yearly maximum with a specified probability of exceedance (e.g. 1%) should be used.

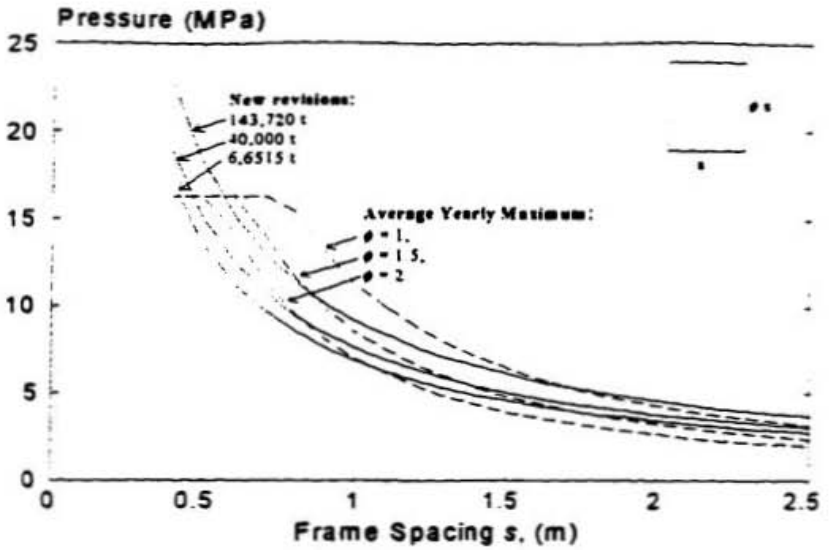

Figure 4. 26 Analysis of design pressure for CAC1 Vessels with r =0.46, n = 10000

4.6 Conclusions and Recommendations

The components of a ship structure and associated strength were reviewed. A long plate, loaded by uniform pressure (referred as the long plate model), was analyzed. Two limit states affect the design of the plating, i.e. plastic collapse and ultimate rupture. The first relates to the serviceability while the latter relates to the safety. There is considerable reserve of strength beyond the three hinge limit in steel plating provided membrane effects can occur. An idealization of ice load as an 'ice belt' is investigated. A model was developed using yield line theory. This model is limited to the plastic collapse and can be only used for serviceability design. The long plate model is easy to implement and is recommended as the design model.

The realistic ice load is more complicated than the idealized uniform pressure, which results in the uncertainties in the design model. Structural response to critical zonal forces are investigated. A plate panel usually fails at a dominant section, which is affected by the lateral support and the interactions between critical zones. Factors affecting the dominant section are investigated in more details in the next chapter.

It is important to associate the design pressure in the long plate model to the yearly maximum ice load. By comparing the yearly maximum ice load from the method presented in Chapter 3 to the new formula in the *ASPPR Proposals*, a design area of $s \times 1.5s$, where s is the frame spacing, is suggested for estimating design ice load. The uncertainties of the design model due to the uncertainty of the ice loads are investigated in the next chapter.

Chapter 5

A Probabilistic Analysis of The Design Model

5.1 Introduction

In Chapter 4, we proposed a design model, which treats the plating as a long plate, loaded by uniform pressure. This model is easy to use in practical design. Realistic ice loads are more complicated than the idealized uniform pressure used in design. They are highly localized, move from place to place and change in intensity. This results in an uncertainty in the design model. If the resistance from the design model is R_d, the true resistance of the plating can be represented as:

$$R = BR_d \quad , \tag{5.1}$$

where R is the true resistance of the plating and B is a factor of uncertainty associated with the randomness of ice load. B is a random quantity and we will investigate this factor in this chapter.

First, we investigate various load scenarios using the finite element method. We approximate ice loads by a number of critical zones, each with a random force, area and location. The dominant failure section in each case is identified, and the section is compared with "an equivalent long plate", which is loaded by strip loads. Factors affecting the

affecting the failure of the plate, such as the size and location of critical zones and the interaction between them are investigated. Second, a model of a long plate, loaded by non-uniform loads is developed. This model can be used to predict the plastic collapse and the ultimate rupture of the equivalent long plate. Third, a scheme of Monte Carlo simulation is proposed to simulate the uncertainty in design model of plating.

We begin with our finite element analysis of structural response to realistic ice loads.

5.2 Structural Response to Realistic Loads

In this section, we further our analysis on the response of the plate panel described in Section 4.4 (see Figure 4.19; material properties of the steel are given in Table 4.1). We assume that the ice loads are applied through a number of critical zones, each approximated by a square with uniform pressure.

The number of critical zones, the area of critical zones, the zonal forces and the locations of critical zones are important factors in the response of the plating. We will use the properties of critical zones from *assumption A* of Chapter 3 in the present analysis. The average number of critical zones is 0.893 zones/m^2. The number of critical zones on a panel can be modelled as a Poisson process. Excluding the case of zero critical zones, the number of critical zones on a panel is a conditional Poisson process. Figure 5.1 shows the probability distribution of the number of critical zones on a panel of 0.72 m^2. Note that one critical zone has the highest probability, and the probability of five critical zones is very small.

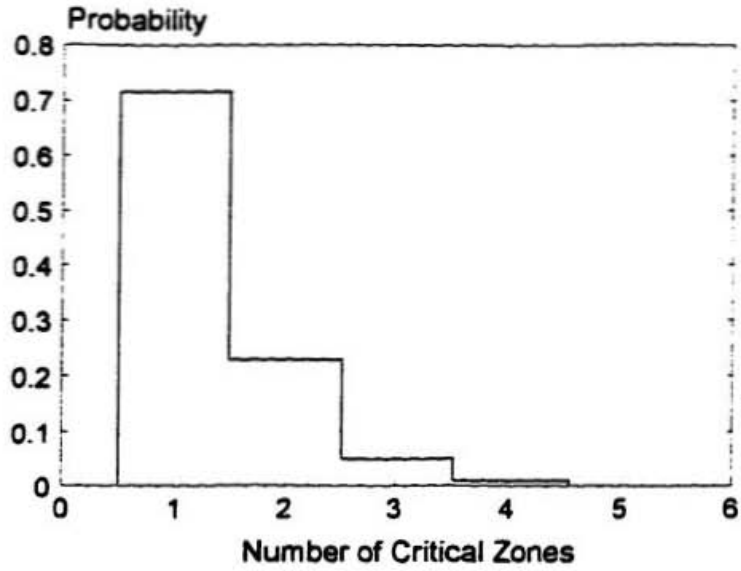

Figure 5. 1 Probability of the Number of Critical Zones on a 0.72 m^2 Panel

The average area of a critical zone is 0.08 m^2, and the probability distribution of zonal area from Louis St. Laurent data is shown in Figure 5.2. The zonal forces range from 0 to 3.45 MN and have an exponential distribution (see Figure 3.11). The data show that the average zonal forces increase with the zonal area. This is shown in Figure 5.3. In the following, we analyze scenarios with one, two and many critical zones, respectively. We use three critical zonal areas, i.e. 0.04, 0.09 and 0.25 m^2, representing small, average and large size critical zones, respectively.

5.2.1 Cases With One Critical Zone

If there is one critical zone on the panel, the plate fails at the dominant section, which passes through the center of the critical zone. The dominant section fails in a way similar to a long plate, loaded by a strip load, with the same width as that of the critical

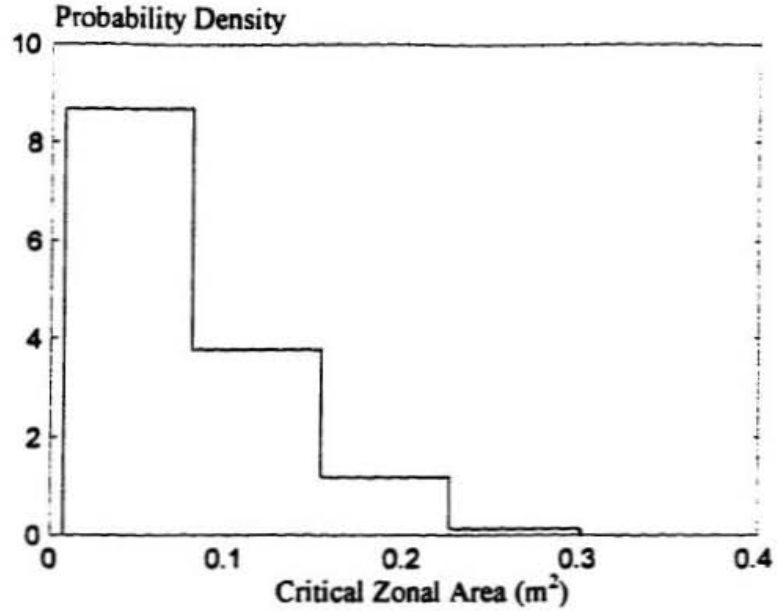

Figure 5. 2 Probability Density of Critical Zonal Area (from Approach A of Chapter 3)

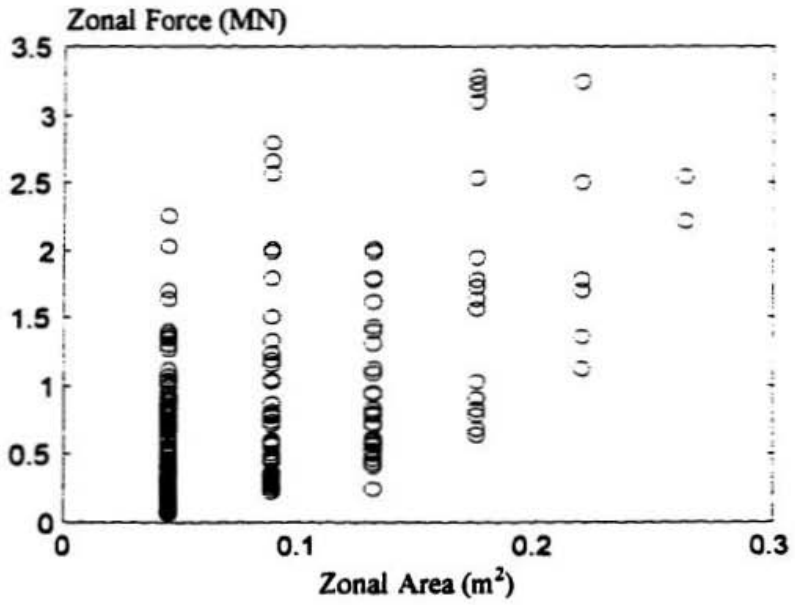

Figure 5. 3 Zonal Forces vs. Zonal Area (from Approach A of Chapter 3)

zone. We refer to this long plate as the "equivalent long plate". This is shown schematically in Figure 5.4. An additional factor affecting the failure of the dominant section is the lateral support. This includes the length of the critical zone (H in Figure 5.4) and the location of the critical zone (y_1 and y_2). To investigate these factors, we selected 20 load cases, which are shown in Figure 5.5.

To investigate the effect of H, we first examine Cases 1 to 3 in Figure 5.5. In these cases, the critical zone is located at the center of the panel. Each case has a different area of critical zone, hence has a different value of H and b. For each case, the pressure of the critical zone at plastic collapse, p_{3h}, is identified from the load deflection curve similar to Figure 4.22. The pressure at ultimate rupture, p_u, which corresponds to 5% of average strain in the dominant section, is identified from the load-strain curve. Similar analyses are carried out on the equivalent long plates (Cases 4 to 6), and pressures at plastic collapse, p_{3h}^e, and at rupture, p_u^e, are identified. We define the factors of lateral support as:

$$f_{3h}^h = \frac{p_{3h}}{p_{3h}^e} , \tag{5.2}$$

and

$$f_u^h = \frac{p_u}{p_u^e} , \tag{5.3}$$

where $h = H/L$, f_{3h}^h, and f_u^h are factors representing lateral support for plastic hinge collapse and rupture, respectively. Results of p_{3h}, p_u, p_{3h}^e, p_u^e, f_{3h}^h, and f_u^h are summarized

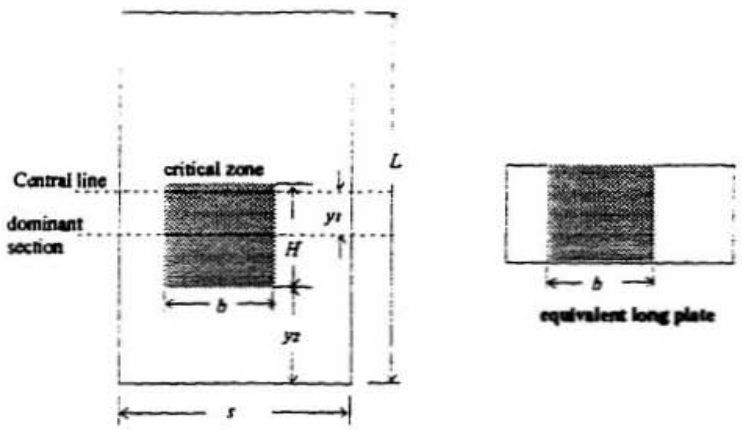

Figure 5. 4 A panel loaded by one critical zone

in Table 5.1. Similar analyses for the cases in which the critical zone is off the center of the panel have been carried out. This includes Cases 10 to 13. The cases of patch load with different h values (Cases 15 to 19) are also included. Results are included in Table 5.1. Values of f_{3h}^{h}, and f_{u}^{h} against different h values are plotted in Figure 5.6 together with the fitted lines. The fitted lines are :

$$f_{3h}^{h} = h^{-0.5582} , \tag{5.4}$$

$$f_{u}^{h} = h^{-0.3563} , \tag{5.5}$$

To investigate the effect of the location, we vary y_1 and y_2. These are Cases 7, 8, 9, 14 and 20. The effect of lateral support increases with y_1 and decrease with y_2. We introduce a location parameter $\Lambda = y_2/y_1$, and the corresponding location factors:

$$f_{3h}^{\Lambda} = \frac{p_{3h}}{p_{3h}^{0}} , \tag{5.6}$$

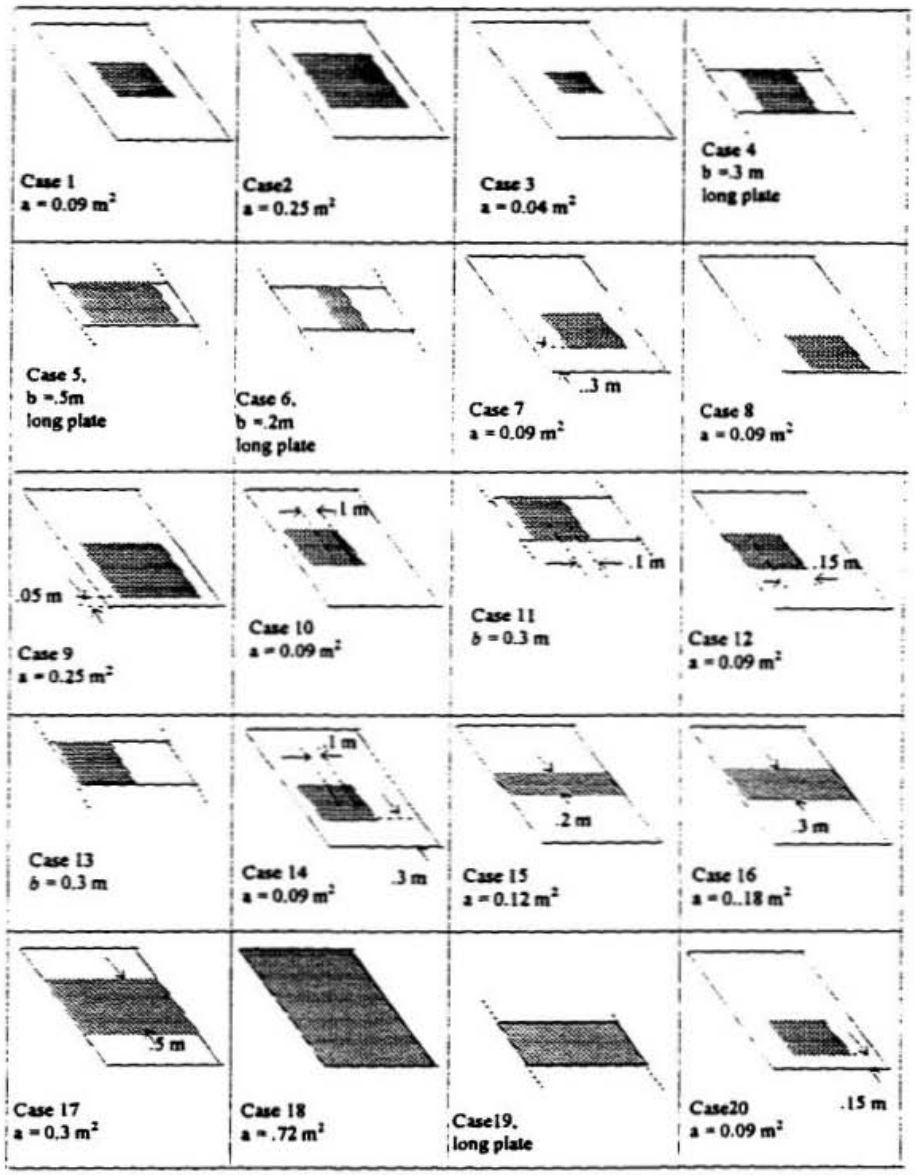

Figure 5. 5 The case with one critical zone

$$f_u^{\Lambda} = \frac{p_u}{p_u^0}, \tag{5.7}$$

where p_{3h}^0 and p_u^0 are pressures at plastic collapse and rupture for the case when $y_1 = 0$, respectively. Values of f_{3h}^{Λ}, and f_u^{Λ} against Λ are plotted in Figure 5.7. Note that the effect of location of critical zones is not significant for $\Lambda > 0.2$. The approximate relations are proposed as:

$$\begin{aligned} f_{3h}^{\Lambda} &= 1.31 - 1.5\Lambda, \quad \Lambda < 0.2 \\ &= 1, \qquad\quad \Lambda \geq 0.2 \end{aligned}, \tag{5.8}$$

$$\begin{aligned} f_u^{\Lambda} &= 1.46 - 1.95\Lambda, \quad \Lambda < 0.21 \\ &= 1.05, \qquad\quad \Lambda \geq 0.21 \end{aligned}, \tag{5.9}$$

We define the mean pressure of the dominant section at failure, $\bar{p}_{3h}$ and $\bar{p}_u$ as the mean pressure over the span:

$$\bar{p}_{3h} = \frac{p_{3h} b}{s}, \tag{5.10}$$

and

$$\bar{p}_u = \frac{p_u b}{s}. \tag{5.11}$$

If the resistance of the plate from the design model (Equations 4.7 and 4.15) are p_{3h}^d and p_u^d for plastic collapse and rupture, respectively, then, the difference between the design model and the selected load scenarios can be evaluated by uncertainty factors B_{3h} and B_u:

$$B_{3h} = \frac{\bar{p}_{3h}}{p_{3h}^d}, \tag{5.12}$$

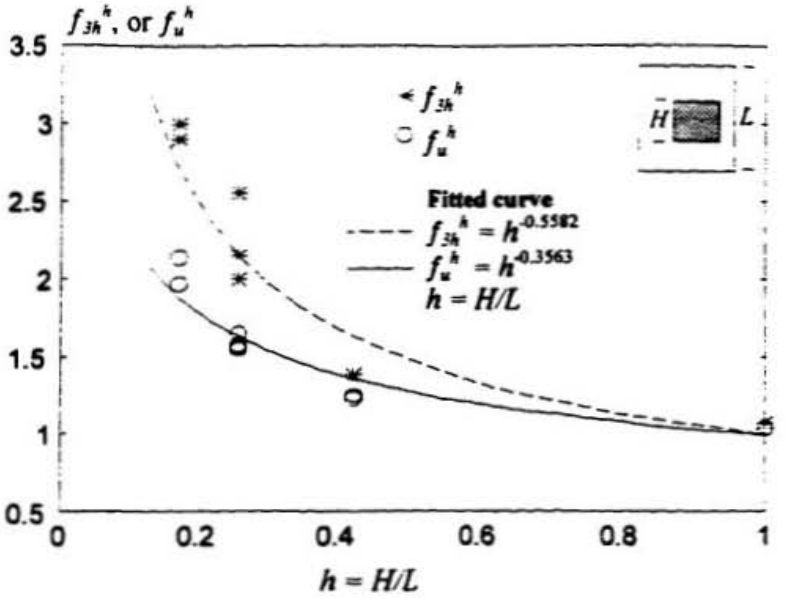

Figure 5. 6 Analysis of the effect of the length of critical zone, h

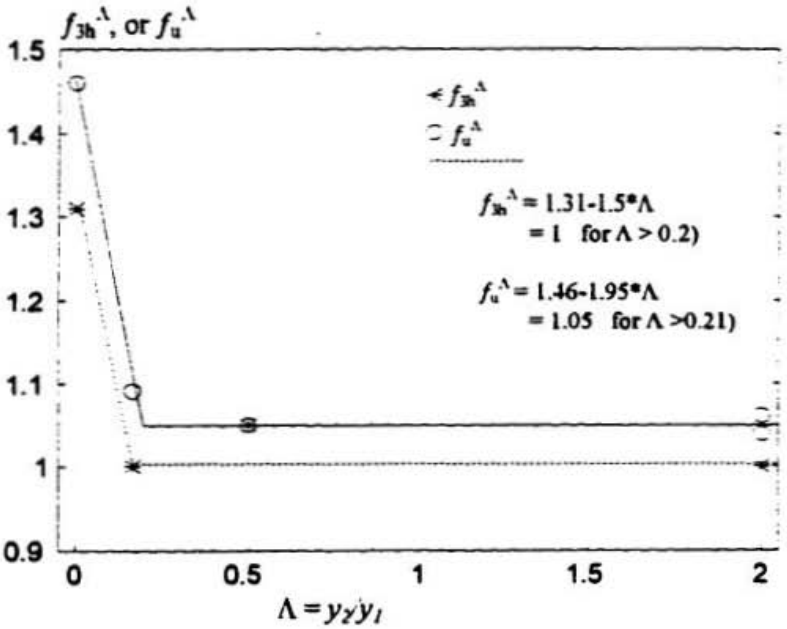

Figure 5. 7 Analysis of the effect of the location of critical zones

Table 5. 1 Results of finite element analysis for Cases 1 to 20

Case	p_{3h} (MPa)	p_u (MPa)	f_{3h}^h	f_u^h	f_{3h}^A	f_u^A	B_{3h}	B_u
1	16	72	2	1.57	-	-	1.32	1.42
2	9	43	1.39	1.23	-	-	1.23	1.41
3	30	122	3	1.97	-	-	1.64	1.60
4	8	46	-	-	-	-	-	-
5	6.5	35	-	-	-	-	-	-
6	10	62	-	-	-	-	-	-
7	16	76	-	-	1	1.06	1.40	1.50
8	21	105	-	-	1.31	1.46	1.73	2.07
9	9	47	-	-	1	1.09	1.23	1.54
10	23	79	2.56	1.55	-	-	1.89	1.56
11	9	51	-	-	-	-	-	-
12	26	91	2.00	1.58	-	-	2.3	1.79
13	13	57.5	-	-	-	-	-	-
14	23	82	-	-	1	1.04	1.89	1.61
15	19	72	2.9	2.14	-	-	3.125	2.83
16	13	55.5	2	1.65	-	-	2.13	2.18
17	9	42	1.38	1.25	-	-	1.48	1.65
18	7	35	1.07	1.04	-	-	1.16	1.38
19	6.5	33.6	-	-	-	-	-	-
20	17	76			1.05	1.05	1.40	1.50

$$B_u = \frac{\bar{p}_u}{p_u^d} \quad . \tag{5.13}$$

Values of B_{3h} and B_u are summarized in Table 5.1. Note that in all cases, B_{3h} and B_u are greater than 1.

5.2.2 The Case With Two or More Critical Zones

If there are more than one critical zones on the panel, the response of the structure is more complicated. In addition to the factors discussed in the case of one critical zone, the response is also dependent on the relative locations between critical zones. The relative locations between critical zones can be divided into three cases, first, the center of these critical zones are aligned along the direction of the frame spacing; second, they are located along the direction of frames; third, these critical zones overlap each other in the direction of frames. We term these *Cases A*, *B* and *C* respectively. This is shown schematically in Figure 5.8.

Case A: If the centers of critical zones are aligned in the direction of frame spacing, the plate fails in a way similar to the case with one critical zone. The dominant section passes through the centers of the critical zones. This dominant section fails in a way similar to the equivalent long plate. Additional factors affecting the failure are the size of critical zones (H in Figure 5.8) and the location of the dominant section. We propose an equivalent length of critical zones as:

$$\bar{h} = \frac{\sum_{i=1}^{n} b_i H_i}{L \sum_{i=1}^{n} b_i} \quad , \tag{5.14}$$

where b_i and H_i are the width and length of *ith* critical zone, n is the number of critical zones and L is defined in Figure 5.4.

To investigate the effect of $\bar{h}$, we examine Cases 21 to 23 of Figure 5.9 together with their equivalent long plates (Cases 24 and 19). The factors of lateral support, $f_{3h}^{\bar{h}}$, and $f_u^{\bar{h}}$ similar to those defined in Equations (5.2 and 5.3) are calculated and the results are summarized in Table 5.2. Values of $f_{3h}^{\bar{h}}$, and $f_u^{\bar{h}}$ against $\bar{h}$ are plotted in Figure 5.10, together with the proposed relations of Equations (5.4 and 5.5). Note that the results agree well with the formulae proposed earlier. For simplicity, we recommend to use Equations (5.4 and 5.5) to account for the effect of $\bar{h}$. We also propose to use Equations (5.8 and 5.9) to account for the effect of locations of critical zones.

Case B: If the critical zones are located along the direction of the frames, the plate fails at a dominant critical zone, which has the maximum zonal force. Other critical zones have effects of interactions with the dominant zone. The interactive effect depends on the distance from each critical zone to the dominant section and the zonal force. The effect increases with the zonal force and decreases with the distance. We define a parameter of interaction, ξ:

$$\xi = \sum_{i=1}^{n} \frac{F_i L}{d_i F} \quad , \tag{5.15}$$

where F_i and d_i are critical zonal force and distance from the center of the critical zone to the dominant section respectively, F is the force of the dominant critical zone. If the plate fails in plastic collapse and rupture at p_{3h}^{ξ} and p_u^{ξ}, respectively, we define the interaction factors for plastic collapse and rupture as:

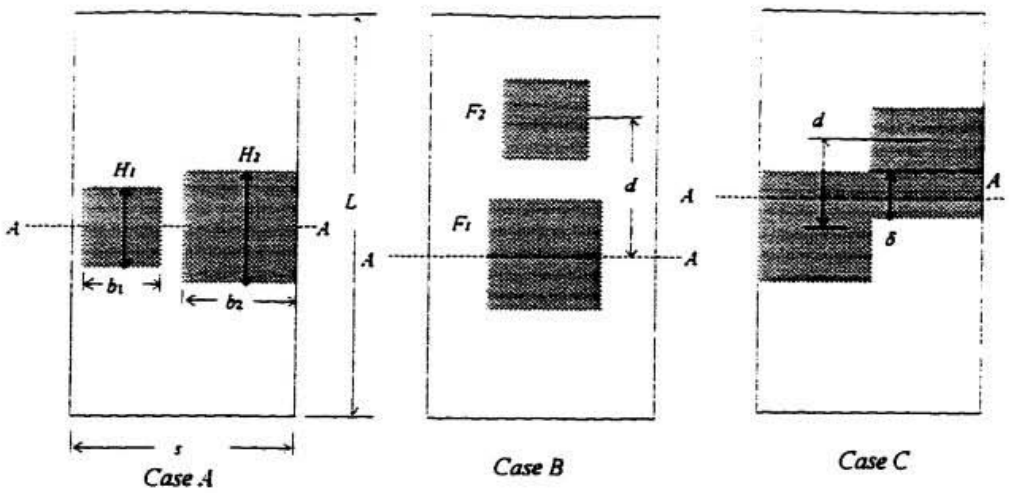

Figure 5. 8 Relative locations between Critical Zones

$$f_{3h}^{\xi} = \frac{p_{3h}^{\xi}}{p_{3h}^{p}} \quad , \tag{5.15}$$

$$f_{u}^{\xi} = \frac{p_{u}^{\xi}}{p_{u}^{p}} \quad , \tag{5.16}$$

respectively, where $p_{3h}{}^{p}$ and $p_{u}{}^{p}$, are pressures at which the plate fails with the dominant critical zone alone.

To investigate the effect of ξ, we examine Cases 25 to 31, 33 and 34 of Figure 5.9. Values of $p_{3h}{}^{\xi}$ and $p_{u}{}^{\xi}$ are obtained from *FEM* and compared with the case in which the plate fails by the dominant critical zone alone (Case 35). The interaction factors are derived from Equations (5.15 and 5.16). Similar analyses are carried out on Cases 32 and 9. Values of $f_{3h}{}^{\xi}$ and $f_{u}{}^{\xi}$ against ξ are plotted together with fitted lines in Figure 5.11. The fitted lines are:

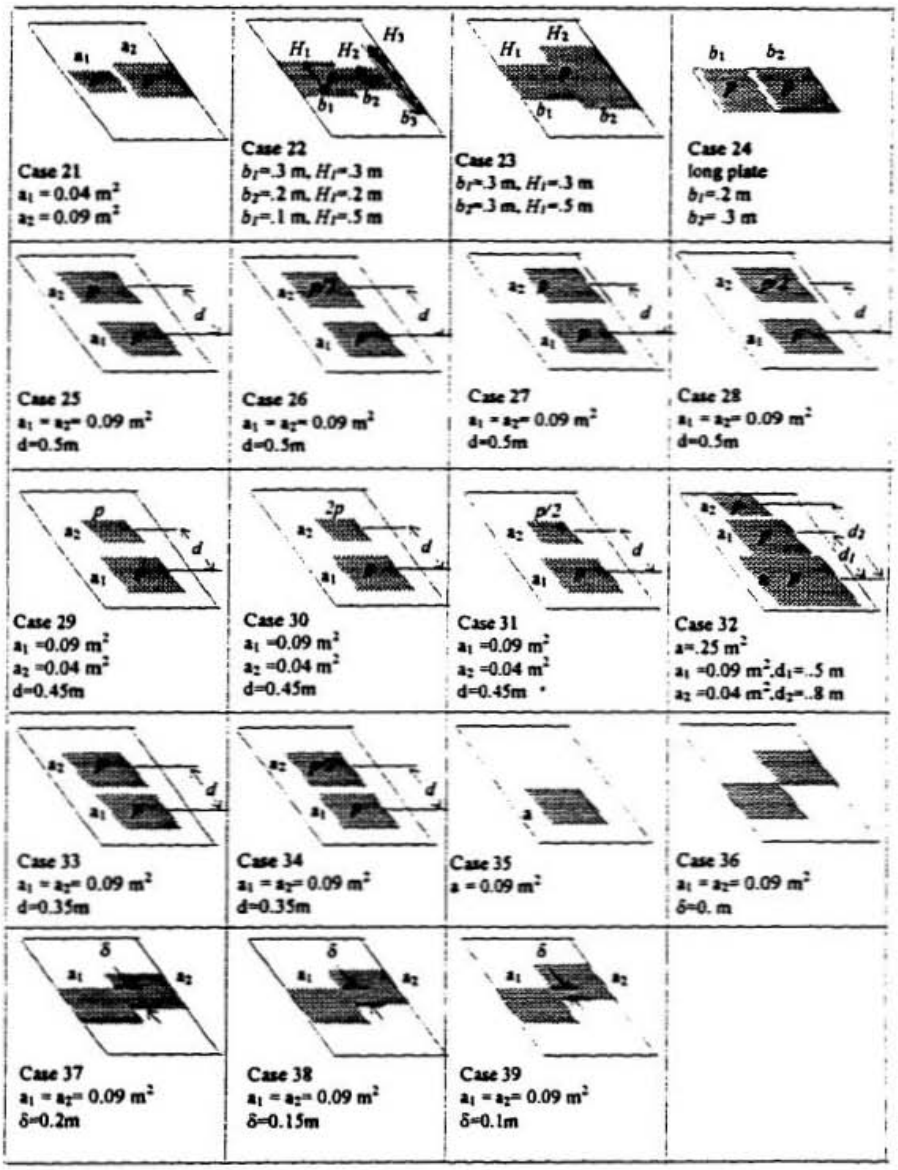

Figure 5. 9 Cases with two or more critical zones

$$f_{3h}^{\xi} = 1 - 0.0571\xi \ , \tag{5.17}$$

$$f_{u}^{\xi} = 1 - 0.0516\xi \ , \tag{5.18}$$

Case B can be simplified by analyzing the case with dominant critical zone alone, with interaction effect from Equations (5.17 and 5. 18).

Case C: If the critical zones overlap each other, the plate fails at a dominant section which is located between critical zones. This is as shown schematically in Figure 5.8. The actual failure of the plate is very complicated. In the present study, we propose a simplified approach.

First, we identify the dominant critical zone, which has the maximum zonal force. For the rest of the critical zones, we divide each into two parts, one aligned on the dominant section and another along the direction of the frame. The first part can be analyzed by the method proposed in *Case A* and the second can be treated as an interacting zone proposed in *Case B*. This is shown schematically in Figure 5.8. The failure pressure can be estimated by analyzing the equivalent long plate with the modifications from the effect of lateral support and the effect of interaction:

$$p_{3h} = f_{3h}^{h} f_{3h}^{\Lambda} f_{3h}^{\xi} p_{3h}^{e} \ , \tag{5.19}$$

$$p_{u} = f_{u}^{h} f_{u}^{\Lambda} f_{u}^{\xi} p_{u}^{e} \ , \tag{5.20}$$

where p_{3h} and p_u are pressures of plastic collapse and rupture at dominant section, respectively, p_{3h}^{e} and p_u^{e} are failure pressures of the equivalent long plate, f_{3h}^{h}, f_{3h}^{Λ}, f_{3h}^{ξ}, f_u^{h}, f_u^{Λ} and f_u^{ξ} are defined as before.

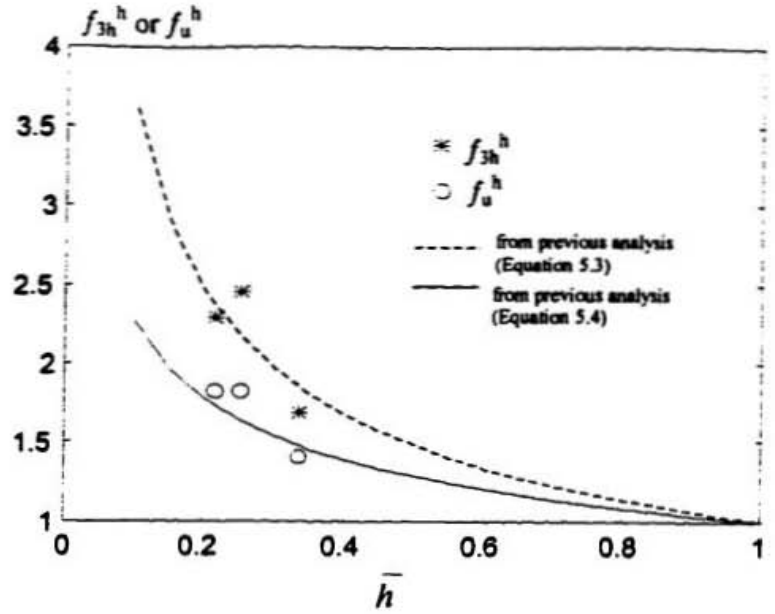

Figure 5. 10 Effect of $\bar{h}$ (the analysis is supported by the previous analysis of h)

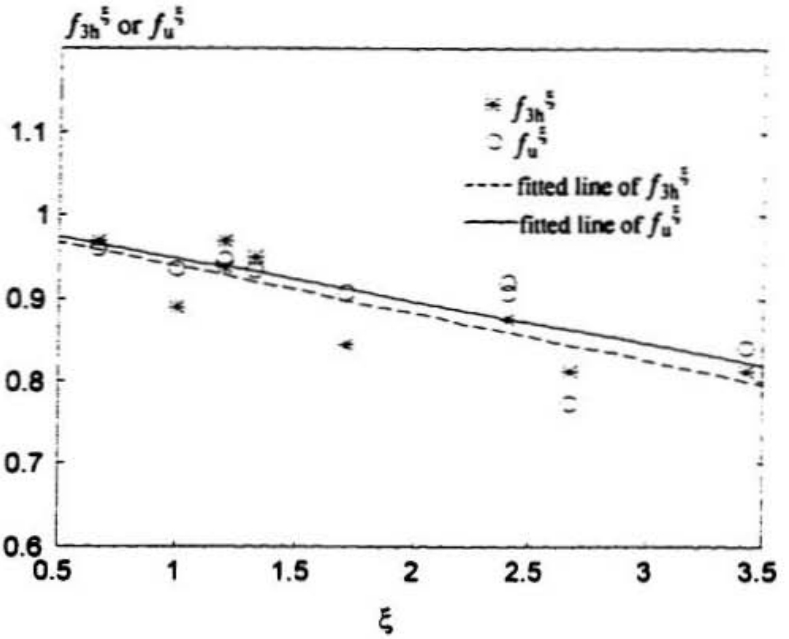

Figure 5. 11 Analysis on the effect of interaction between critical zones.

Table 5. 2 Results of finite element analysis for Cases 21 to 39

Case	p_{3h} (MPa)	p_u (MPa)	f_{3h}^{h}	f_u^{h}	f_{3h}^{ξ}	f_u^{ξ}	B_{3h}	B_u
21	16	71	2.29	1.82	-	-	2.19	2.33
22	16	61	2.46	1.82	-	-	2.63	2.4
23	11	47.5	1.69	1.41	-	-	1.81	1.87
24	7	39	-	-	-	-	-	-
25	14	68	-	-	.875	.907	1.15	1.34
26	15	71	-	-	.938	.947	1.23	1.40
27	14	69	-	-	.875	.92	1.15	1.36
28	15.5	71	-	-	.961	.947	1.28	1.40
29	15.2	71	-	-	.95	.933	1.25	1.40
30	13	58	-	-	.813	.773	1.07	1.14
31	15.5	72	-	-	.969	.96	1.28	1.42
32	8	44	-	-	.889	.936	1.10	1.44
33	13.5	68	-	-	.844	.907	1.11	1.34
34	13	63	-	-	.813	.84	1.07	1.24
35	16	75	-	-	-	-	-	-
36	20	70	-	-	.77	.794	1.65	1.38
37	13.5	54	2.4	1.75	.886	.897	2.22	2.13
38	15	52	2.55	1.81	.848	.86	2.46	2.05
39	15	59	2.72	1.89	.771	.794	2.46	2.32

The above method is applied to Cases 36 to 39 in Figure 5.9. These cases are also analyzed by finite element method. Results from Equations (5.19 and 20) are plotted against the results from FEM in Figure 5.12. The results from the simplified method agree well with those from the finite element method.

Mixed Case: The plate will fail by a dominant zone, which can be analyzed by an equivalent long plate. The pressure distribution on the equivalent long plate can be obtained by superimposing the pressure of the dominant zones with the ones of those overlapping with the dominant zone. This is illustrated later in Figure 5.19. Other zones affect the failure in terms of effect of interaction or the effect of lateral support which can be approximated by the proposed formula.

5.3 A Long Plate Loaded By Non-Uniform Forces

As we concluded from the preceding section, the response of a plate to the critical zonal forces can be approximated by an equivalent long plate with modifications from the effect of lateral support and the interaction effect between critical zones. The equivalent long plate is loaded by non-uniform loads. In this section, we propose a simple model to analyze the plastic collapse and rupture of such a plate. The plate is schematically shown in Figure 5.13. We define the "equivalent uniform strength" as the maximum mean pressure that the plate can support.

5.3.1 Three Hinge Mechanism

We assume that three plastic hinges form at points A, B and i as shown in Figure 5.14. We assume that the beam is rigid plastic and use the upper bound theorem. First,

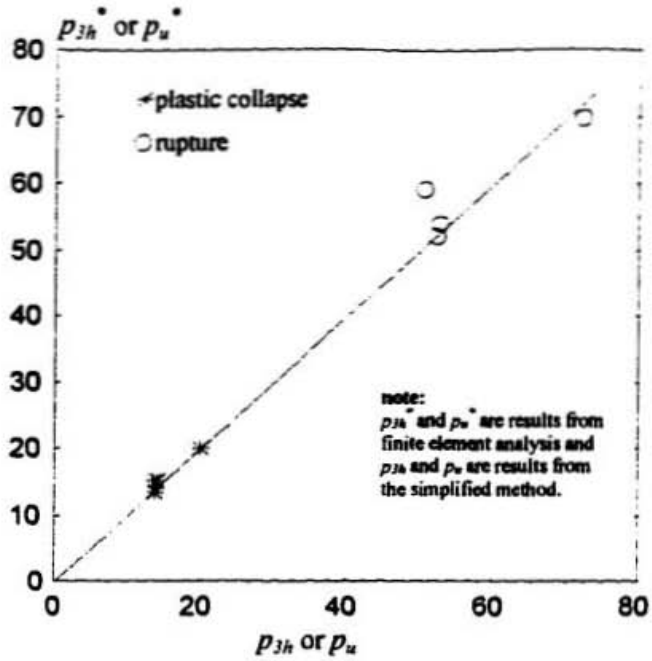

Figure 5. 12 Analysis of CASE C

the governing equation is derived by equating the external work to internal energy as:

$$M_A \frac{\delta_i}{x_i} + M_B \frac{\delta_i}{s - x_i} + M_i \left(\frac{\delta_i}{x_i} + \frac{\delta_i}{s - x_i}\right) = \sum_{j=1}^{i} F_j \frac{x_j}{x_i} \delta_i + \sum_{j=i+1}^{n} F_j \frac{s - x_j}{s - x_i} \delta_i \qquad (5.21)$$

where M_A, M_B and M_i are bending moments at points A, B and i respectively and are equal to plastic moment M_P defined in Equation (4.2). We define the proportional loads, at which the three hinges form, as follows:

$$F_j' = A' f_j \qquad (5.22)$$

where f_j is a profile of point loads which varies from 0 to 1. A' in Equation (5.22) is the amplitude at which the third plastic hinge forms at i point. Further we define corresponding proportional mean pressure as:

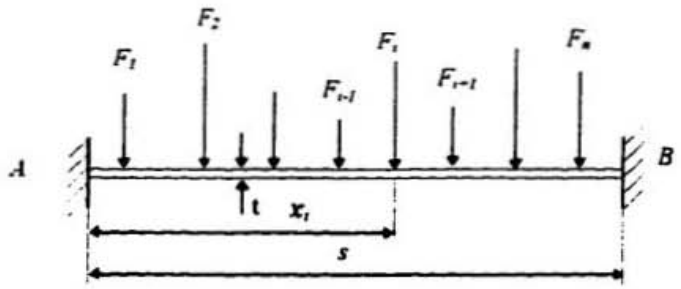

Figure 5. 13 Schematic Diagram of a Beam Loaded by multiple Point loads

$$P' = \frac{\sum_{j=1}^{n} A' f_j}{s} \tag{5.23}$$

Substituting equations (5.22) and (5.23) into (5.21) and rearranging gives:

$$P' = \frac{\sum_{j=1}^{n} f_j}{\left(\sum_{j=1}^{i} f_j \frac{x'_j}{x'_i} + \sum_{j=i+1}^{n} f_j \frac{1-x'_j}{1-x'_i} \right) x'_i (1-x'_i)} \frac{2M_p}{s^2} \quad , \tag{5.24}$$

where $x'_i = x_i / s$ and $x'_j = x_j / s$ are normalized coordinates. The strength of the plate at plastic collapse can be then derived by minimizing the proportional pressure in Equation (5.23). Since plastic hinges at points A and B are necessary for the mechanism, the strength of the plate can be obtained by minimizing P_i with respect to x_i,

$$P_{3H} = \min(P') \tag{5.25}$$

where i = 1 to n. Note that point i does not need to be at a point with force F_i, but between F_{i-1} and F_i.

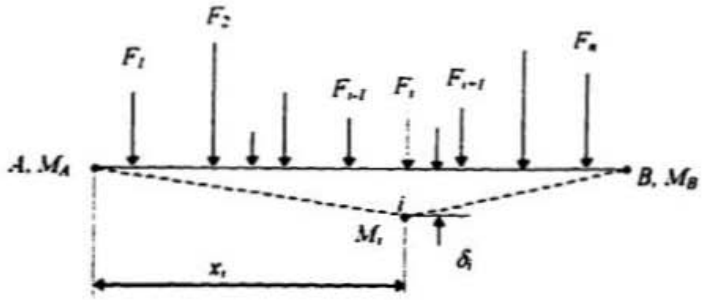

Figure 5. 14 Three Hinge Mechanism

5.3.2 Membrane Action and Ultimate Rupture

We assume that the effect of bending is negligible when the membrane action takes place. The deflection of the beam due to point forces is schematically shown in Figure 5.15. In the following, we will derive the deflection and the nominal strain due to the membrane action. We will use the equilibrium conditions in deriving the governing equation and as a result, the solution is a lower bound. First, the vertical reaction forces at the ends of the beam can be derived based on the equilibrium condition as:

$$F_A = \frac{\sum_{i=1}^{n} F_i(s - x_i)}{s} = A\sum_{i=1}^{n} f_i(1 - x'_i) \,, \tag{5.26}$$

and

$$F_B = \frac{\sum_{i=1}^{n} F_i x_i}{s} = A\sum_{i=1}^{n} f_i x'_i \,, \tag{5.27}$$

where $F_i = Af_i$ is the proportional load at ith point, A is the proportion at which the ultimate rupture occurs and f_i is the load profile described before. The equilibrium condition at each load point gives:

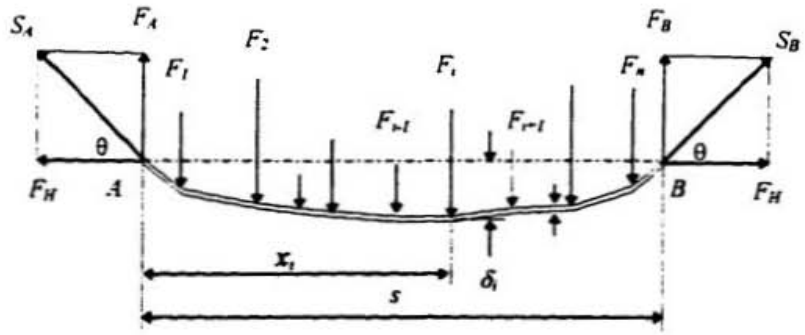

Figure 5. 15 Schematic View of Membrane Action of a Beam Loaded with point Loads

$$F_A x'_i - \sum_{j=1}^{i} (x'_i - x'_j) F_j - F_H w'_i = 0, \qquad i = 1...n \ , \tag{5.28}$$

where $w'_i = w_i / s$ is normalized deflection at ith point. Manipulating (5.28) yields:

$$w'_i = \frac{F_A x'_i + \sum_{j=1}^{i} (x'_i - x'_j) F_j}{F_H} \ , \tag{5.29}$$

where F_H can be derived based on the geometric condition indicated in Figure (5.15):

$$F_H = \frac{F_A}{\tan(\theta)} = \frac{F_A x'_1}{w'_1} \ . \tag{5.30}$$

Similarly, w'_1 in Equation (5.30) can be derived as:

$$w'_1 = \frac{F_A x'_1}{\sqrt{S_A^2 - F_A^2}} \ , \tag{5.31}$$

where S_A is the membrane force. For full plastic membrane action, S_A is the plastic tensile stress in the plate and can be expressed as:

$$S_A = \sigma^*_y t \quad , \tag{5.32}$$

where σ^*_y is the yield strength. Substituting Equation (5.30) into (5.29) yields:

$$\begin{aligned} w'_i &= \frac{F_A x'_i - \sum_{j=1}^{i} (x'_i - x'_j) F_j}{\frac{F_A x'_1}{w'_1}} \\ &= \left(\frac{x'_i}{x'_1} - \sum_{j=1}^{i} \frac{x'_i - x'_j}{x'_1}\right) w'_1 \end{aligned} \quad , \tag{5.33}$$

Finally, we define the nominal strain for the membrane action as the ratio of the total elongation to the original length:

$$\begin{aligned} \varepsilon &= \frac{\sum_{i=2}^{n} \sqrt{(w_i - w_{i-1})^2 + (x_i - x_i)^2} + \sqrt{w_1^2 + x_1^2} + \sqrt{w_n^2 + (s - x_n)^2}}{s} - 1 \\ &= \sum_{i=2}^{n} \sqrt{(w'_i - w'_{i-1})^2 + (x'_i - x'_i)^2} + \sqrt{w'^2_1 + x'^2_1} + \sqrt{w'^2_n + (1 - x'_n)^2} - 1 \end{aligned} \quad . \tag{5.34}$$

Usually, the ultimate strength of the plate is characterized by a nominal ultimate strain ε_u and $\varepsilon_u = 0.05$ for steel plate was suggested by Egge and Böckenhauer (1991). Substituting the suggested ε_u and Equation (5.33) into Equation (5.34) one can derive the corresponding w'_i. In the present approach, this is achieved numerically. Once w'_1 is obtained, the corresponding F_A can be derived from Equation (5.31) and subsequently the factor A defined in Equation (5.27) can be derived. We define the corresponding *ultimate strength* as:

$$P_u = \frac{\sum_{i=1}^{n} F_i}{s} = \frac{A}{s}\sum_{i=1}^{n} f_i \qquad (5.35)$$

5.3.3 Results and Comparison With Finite Element Modelling

The two models presented in preceding sections were implemented into a computer program using **matlab**. First, we use these models to analyze three typical cases shown in Figure 5.16 (a), (b) and (c). Figure 5.16 (c) represents the load profile corresponding to the minimum strength for the plate. The pressure in (a) and (b) is approximated by nineteen point forces. The results of three-hinge collapse are presented in Table 5.3 in terms of normalized strength. The exact solutions are also given in the table and good agreements are noticed. The results of ultimate rupture are given in Table 5.4. The approximate solutions of Equations (4.15) and (4.16) are also given in the table. The results of the point load model agree well with the approximate solutions.

Next, we analyze the cases (d, e and f) in Figure 5.17 and compare the results with those of finite element analysis. The material properties are given in Table 4.1. The results are summarized in Table 5.5. Note that results from the present analysis and the finite element modelling agree well in the case of plastic collapse. For the rupture, the present analysis under-estimates the pressure by a factor greater than 1.3.

Table 5. 3 The Mean Pressure at Three Hinge Collapse for Different Load Type

Load Type	P_{3H} (point loads model)	P_{3H} (exact solution)
Uniform Load	16 M_p/s^2	16 M_p/s^2
Tent Shape	11.7 M_p/s^2	12 M_p/s^2
Point Load	8 M_p/s^2	8 M_p/s^2

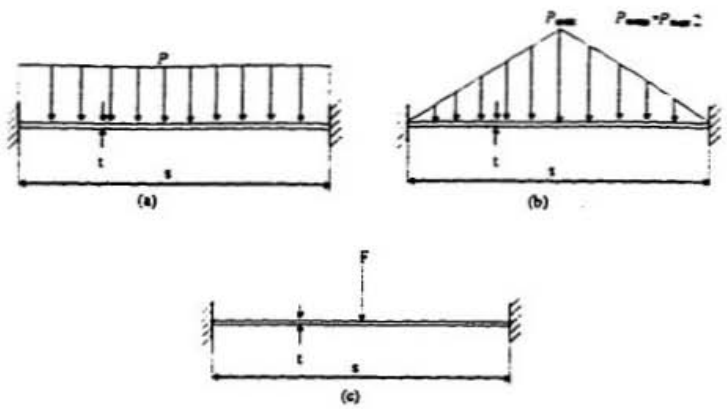

Figure 5. 16 Beam under Different Loading Conditions, (a) Beam Loaded by Uniform Point Loads, (b) Beam Loaded by Tent Shape Point Loads, (c) Beam Loaded by A Single Point Load

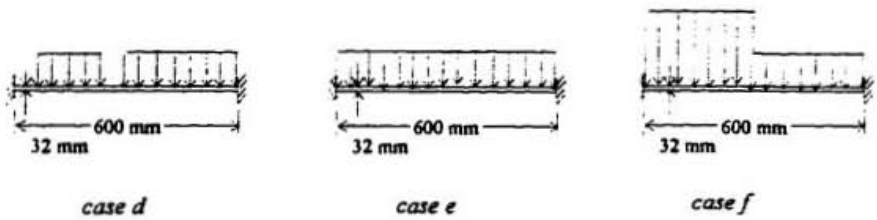

Figure 5. 17 Different load cases

Table 5. 4 Comparison of Point Load Model with the Approximate Solutions

		Present Model	**Approximate Solution Equations (4.15) and (4.16)**
Uniform Distribution	p_U	$0.976\sigma^*_y t/s$	$1.03\sigma^*_y t/s$
	δ_{max}	$0.141s$	$0.168s$
Tent Shape Distribution	p_U	$0.802\sigma^*_y t/s$	
	δ_{max}	$0.146s$	
Single Point Load	p_U	$0.61\sigma^*_y t/s$	

Table 5. 5 Results for Cases d, e and f

Case	Case d	Case e	Case f
p_{3h}	6.05	6.08	5.95
p_U	24.15	24.06	22.91
p_{3h}^* (from FEM)	5.83	6.5	5.85
p_U^* (from FEM)	32.5	33.6	32.25
p_{3h}^* / p_{3h}	0.963	1.07	0.983
p_u^* / p_u	1.35	1.40	1.41

5.4 Modeling of the Uncertainty in the Design Model

5.4.1 The Model

In this section, we propose a probabilistic approach to the uncertainty in the design model. We assume that the ice load is applied through a random number of critical zones, each with a random size, force and location. We approximate each critical zone by a square, with uniform pressure. For each load case, the strength of the panel is estimated and compared with that of the design model. We analyze this by Monte Carlo simulations. The scheme is described below.

First, we randomly chose the number of critical zones on the panel. We assume that the number of critical zones follows a Poisson process, with a density of ρ zones/m^2. In present analysis, $\rho = .893$ zones/m^2 is used following *Approach A* in Chapter 3. In our model, we are not considering the case in which the number of critical zones is zero;

therefore the probability for the number of critical zones is a conditional probability of $n > 0$, where n is the number of critical zones. The *pdf* of the number of critical zones used in present analysis (for an area of 0.72 m^2) is shown in Figure 5.1.

Next, we randomly chose the size, location and zonal force for each critical zone. The size can be determined from the *pdf* of the ship trial data of Louis St. Laurent (Figure 5.2). For the location, we assume that the critical zone is fully located within the panel following the assumption in *Approach A* of Chapter 3. The center of the critical zone (x, y) is randomly located between ([$b/2$, $s-b/2$], [$H/2$, $L-H/2$]), following an uniform distribution. This is shown schematically in Figure 5.18. The zonal force referred here is the relative amplitude between critical zones. We chose this force randomly from the probability of exceedance shown in Figure 3.11 (*Approach A*).

Figure 5.19 shows schematically a load case chosen randomly by the above described procedure. For such a load case, we identify the dominant critical zone as the one with the maximum zonal force. Next, we examine the pressure distribution on the dominant section. This is achieved by superimposing the pressure of the dominant zone with the zones of others which are aligned with the dominant one, e.g. Zone 1 in figure 5.19, and which overlap with the dominant zone, e.g. Zone 3 in Figure 5.19. The strength of the dominant section can be obtained by analyzing the equivalent long plate, the effect of lateral support and the interactive effects. The failure of the equivalent long plate can be analyzed by the model proposed in Section 5.3 (Equations 5.25 and 5.35). The effect of location of the dominant critical zone can be obtained from Equations (5.8 and 5.9). The

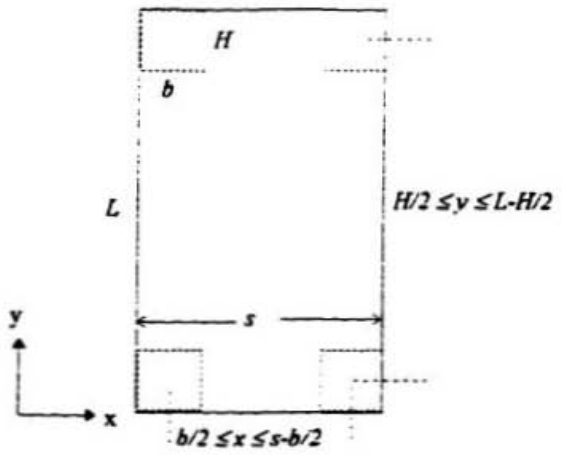

Figure 5. 18 Variation of the location of a critical zone

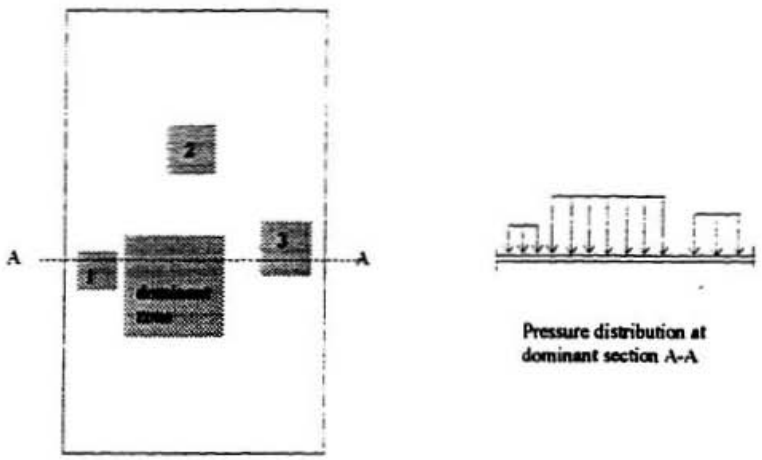

Figure 5. 19 A randomly chosen load case

effect of lateral support can be estimated from Equations (5.4, 5.5 and 5.14). The effect of interactions between critical zones can be estimated by Equations (5.17, 5.18 and 5.15). Once the strength of the dominant section is obtained, it is compared with the results of

the design model, hence the model uncertainty defined by factor B in Equation (5.1) can be evaluated.

5.4.2 Results

The flow chart of the above described procedure is shown in Figure 5.20. The procedure is implemented in a computer program using **matlab**. As an example, we perform our analysis on the plate panel shown in Figure 4.19. A total of 1000 iterations are performed. Figure 5.21 and 5.22 show the results in terms of the probability distribution of uncertainty factors B_{3h} and B_u for plastic collapse and ultimate rupture, respectively. An approximation of the probability densities by a lognormal distribution with parameter $\Lambda(\mu, \sigma^2)$ and by a truncated Weibull distributions are also plotted in the figures. Both distributions approximate the left tail of the probability density well. For convenience, we use the lognormal distribution to approximate these uncertainties in the present analysis. Parameters of the lognormal distribution corresponding to Figures 5.21 and 5.22 are given in Table 5.6.

Table 5. 6 Probability Density Functions for Model Uncertainty (lognormal)

	mean	*COV*	μ	σ
Three Hinge Collapse, B_{3h}	1.553	0.206	0.420	0.204
Ultimate Rupture, B_u	1.371	0.182	0.299	0.180

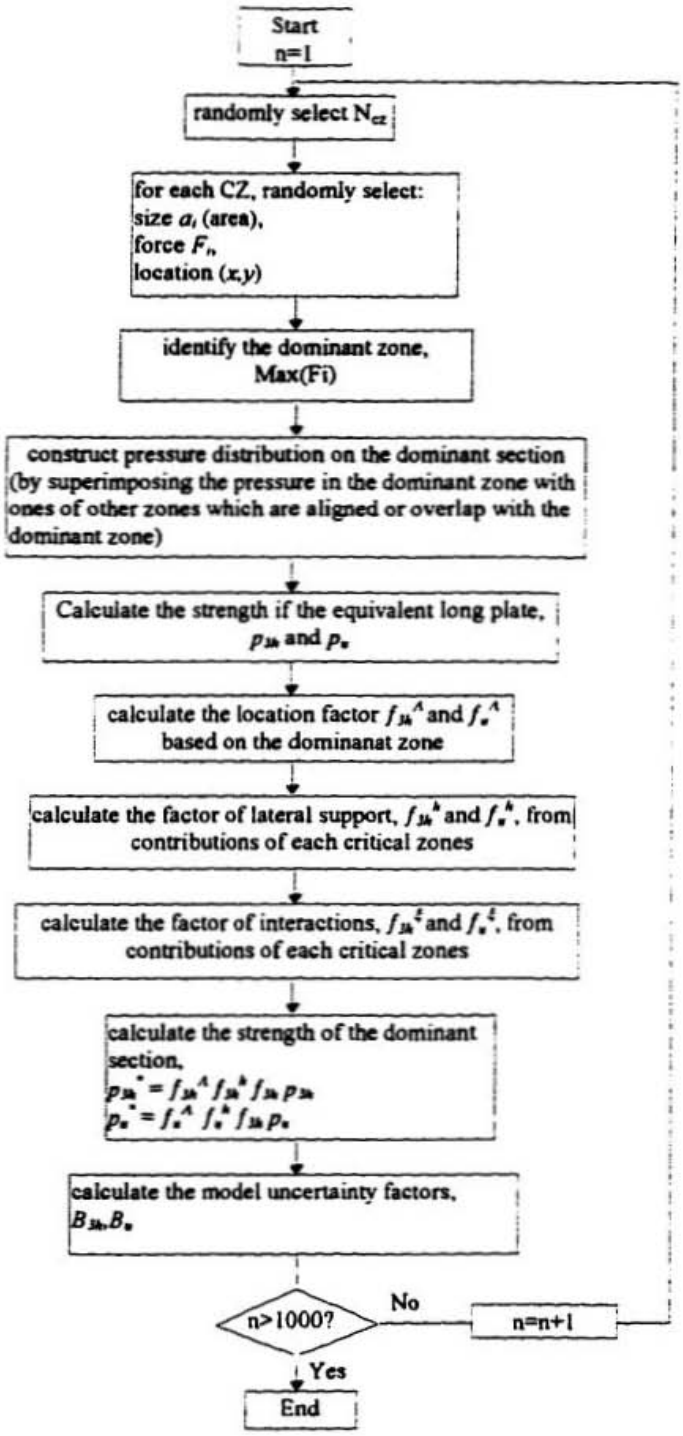

Figure 5. 20 A Scheme of Monte Carlo Simulations

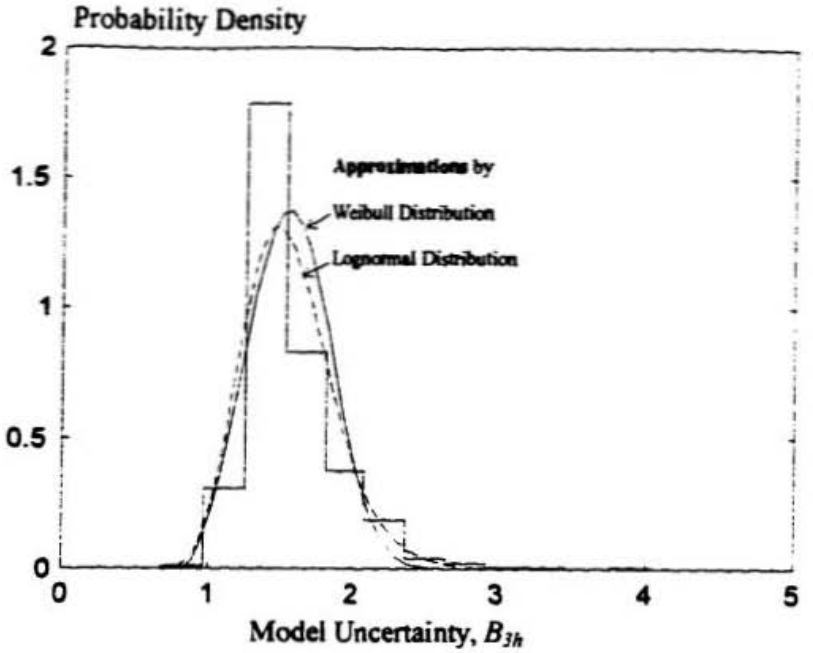

Figure 5. 21 Model Uncertainty for Plastic Collapse

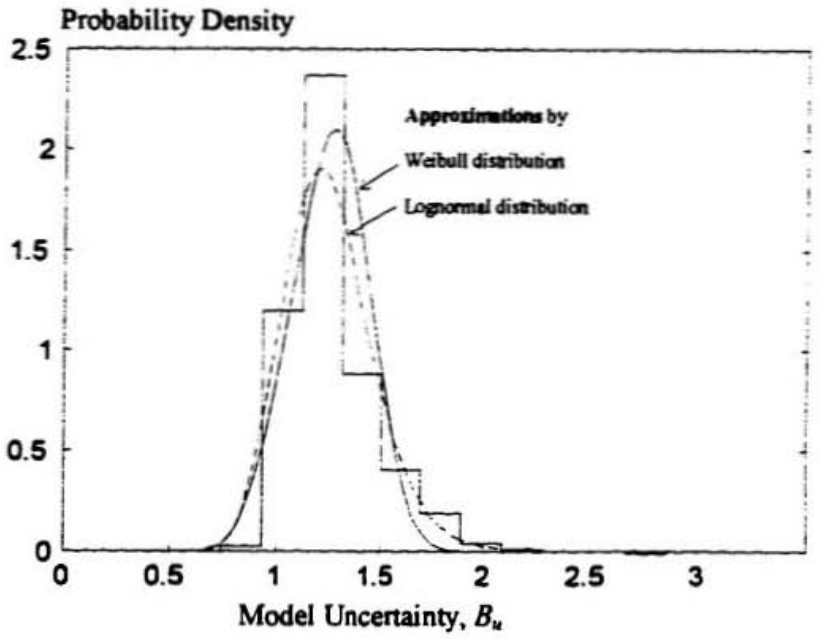

Figure 5. 22 Model Uncertainty for Ultimate Rupture

5.6 *Conclusions and Recommendations*

The uncertainty of the design model due to the randomness of the ice loads was analyzed. A number of 39 load cases are analyzed using finite element method. It was found that the plate failed by a dominant critical zone. The dominant section fails in a way similar to an equivalent long plate. Additional factors affecting the failure of the dominant sections are the effect of lateral support, the effect of location and the effect of interaction between critical zones. Empirical formulae for these factors are proposed based on the results of finite element analysis.

A simplified model of a long plate, loaded by a non-uniform load was proposed. The model considered both three hinge failure mechanism and the ultimate failure by membrane action. This model can be used to estimate the strength of the equivalent long plate. A scheme of simulating the uncertainty in the design model due to the randomness of the ice loads was proposed. Monte Carlo simulations were performed and the results were presented in terms of the probability density of uncertainty factors. The uncertainty factor for plastic collapse has a mean value of 1.553 and a *COV* of 0.206. The uncertainty factor for the ultimate rupture has a mean value of 1.371 and a *COV* of 0.182. Both probability densities can be approximated by a lognormal distribution. It is recommended that the model uncertainty should be considered when evaluating the safety of the structures which are designed by the design model.

Chapter 6

Design Principles

6.1 Introduction

The most important issue in an ice related design is to select a design ice load and to choose a structural resistance. Chapters 3 to 5 investigated the uncertainties in ice loads and in the design model of the structure. This chapter discuss the design principles from the findings of the previous chapters.

First, we review two design methods, namely the reliability method and the code design method. Second, we discuss the rationale in selecting a design ice load and a structural resistance. Third, we apply both the reliability method and the code design method to the calculation of ship plating. Different design strategies are proposed to specify the ice load and resistance. The probability of failure for each strategy is evaluated. The analysis is based on a concept design of an oil tanker, which is described below.

The concept design: A vessel, with an approximate capacity of 830,000 bbls, is proposed to serve as a tanker for a local refinery in Newfoundland or as a shuttle tanker to and from an offshore oil field. Interaction with glacial ice is a potential hazard to this vessel and is a major consideration for structural design. Glacial ice includes icebergs of all sizes including bergy bits and growlers. The expected number of impacts per year is

very low for this vessel, and varies for different operating routes. A study by Fuglem et al., (1996) showed that the expected number of glacial-ice impacts for this kind of tanker is 0.5 to 2 per year. This number could be even lower if measures of avoidance are taken. A design code for such a case is not available. In this analysis, we will use a reliability method and partial safety method in selecting the structural resistance. We will limit our analysis to the plating. The expected number of impacts is chosen as one per year. The principal dimensions for the tanker are determined based on a similar concept design of an OBO vessel in Carter et al. (1992) and are listed in Table 6.1.

First, we review two design methods mostly used in practice.

6.2 Design Methods

The design of a structure can be viewed as a decision problem. The designer has to give due considerations to two conflicting objectives:

- safety: the minimization of the risk to individuals and the environment; and
- economy: the careful and efficient use of private and public resources.

There is no unique solution to the design decision problem. Indeed, technical decisions are made in the face of uncertainty, since the future state of nature, e.g. loads imposed by the environment, is not known at the time of decision-making.

Figure 6.1 shows a decision tree for the design of a certain structural member. Suppose a particular specified strength or resistance (e.g. yield strength) for the structure, r_{sn}, is decided upon, the actual resistance is not necessarily equal to r_{sn}, but is a random

Table 6. 1 Principal Particulars of the Vessel

Length, BP	260 M
Beam	44 M
Depth	24 M
Design Draft	16 M
Displacement	140,000 tones
Power	20.5 MW
Frame Spacing (Bow Area)	600 mm
Frame Spacing (Main Hull)	750 mm

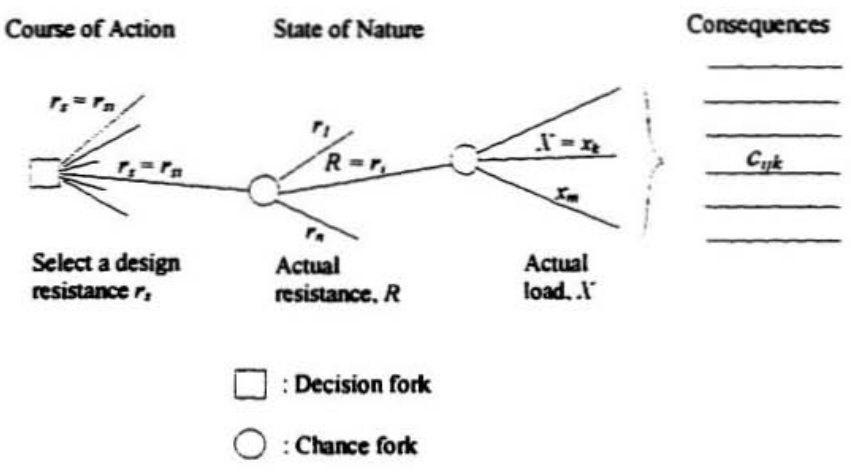

Figure 6. 1 Analysis of a Design Decision

quantity R with a probability density function, $f_{R|r_{si}}(r|r_{si})$, where the notations $R|r_{si}$ and $r|r_{si}$ represent the condition "given r_{si}". Not only the actual resistance R, but also the actual load, X, is random. Both random quantities characterize the "uncertain states of nature" that the designer is faced with.

In Figure 6.1, to each combination of selected r_{si}, actual resistance r_j and actual load x_k, we can ascribe certain consequences c_{ijk}. The degree of satisfaction associated with c_{ijk} is generally the product of many interacting evaluations and is expressed by the "utility" $u(c_{ijk})$. The object of utility theory is to analyze formally the preferences among each of the consequences, c_{ijk}.

The above described decision process is usually complicated due to the large number of possible outcomes. This complexity can be greatly reduced by an approach using risk analysis. Suppose the level of performance of a particular combination (i, j, k) in Figure 6.1 is valued in terms of a single criterion, namely a limit. In our analysis, this limit state can be three-hinge collapse or ultimate rupture of a plate. For given values of $R = r_j$ and $X = x_k$, the outcome would be either that the structure will fail or not fail. By working back two steps in the decision tree in Figure 6.1, it is possible to appreciate the effectiveness of original choice of design strength r_{si} by means of a single number, namely the probability of failure (Jordaan, 1982). This failure probability is readily evaluated once the probability densities of resistance, R and load, X are known:

$$P_f = \iint_{all\ r \le x} f_X(x) f_R(r) dr dx , \tag{6.1}$$

where $f_X(x)$ and $f_R(r)$ are probability densities of load and resistance respectively. As schematically shown in Figure 6.2 (a), the probability of failure P_f depends on the zone where two densities overlap. Based on P_f, it is possible to evaluate the systems which are unsafe, illustrated in Figure 6.2 (b) and those are too safe, Figure 6.2 (c). An optimal criterion is obtained when the probability of failure is close to a certain target value.

In practical design, two methods can be used to achieve this target value, namely the reliability design method and code design method. These two methods are described below.

6.2.1 Reliability Method.

The reliability method is directly based on the probabilistic analysis of structural failure. The solution of the analysis (the optimal design) is the one with the probability of failure close to the target value of the probability of failure. Usually, the reliability design of a ship structure involves an iterative process consisting of initial estimation of ship parameters, prediction of the environmental loads, analysis of the structural response and evaluation of the structural safety (Jordaan et al. 1987). Figure 6.3 illustrates such a process, in which, the estimations of the environmental forces, the structural capacity and the reliability are the key steps of the whole procedure. Initial estimates of overall ship parameters, including displacement, operating mode, bow geometry, scantling of principal members, can be achieved based on the previous experience. The optimization enables a designer to achieve the desired safety at minimum structural costs. The optimal design is

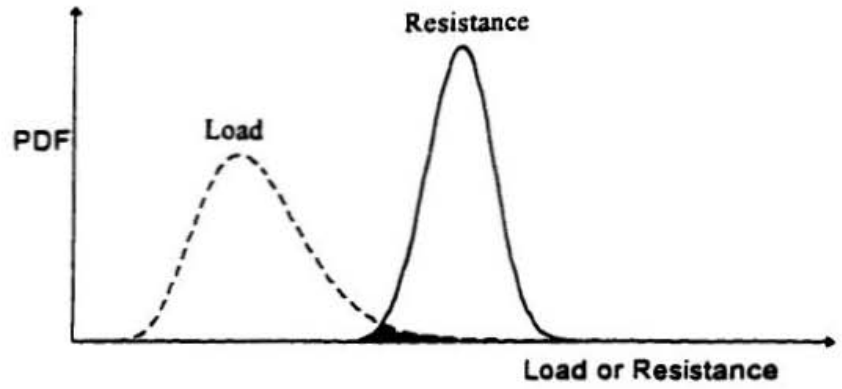

a) Failure Probability (calculated)

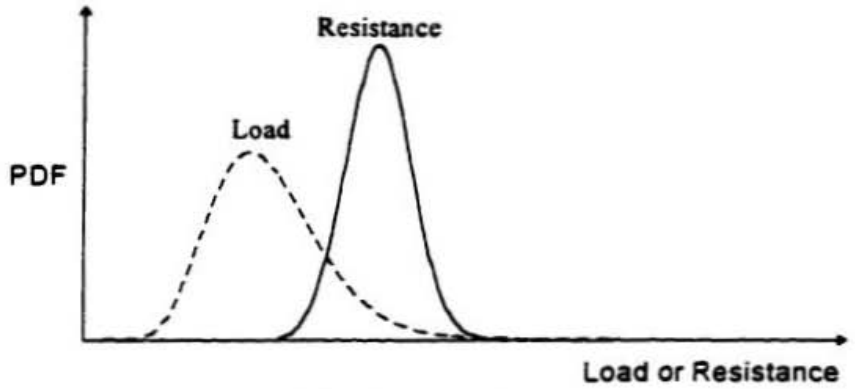

b) Unsafe Structure

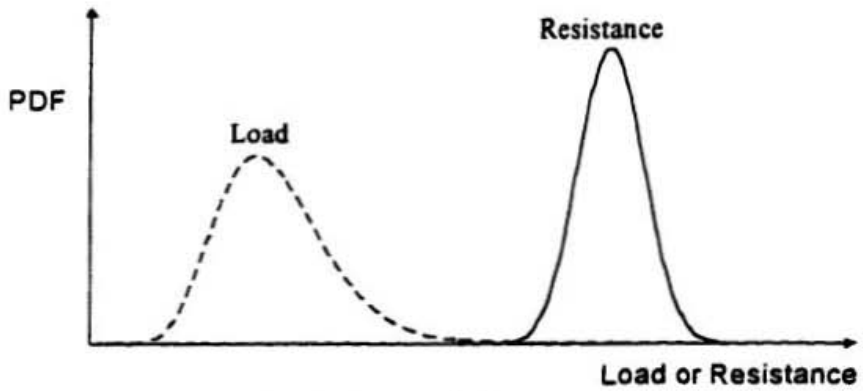

c) Over-Designed Structure

Figure 6. 2 Comparison of Failure Probabilities a) A Safe Structure, b) An Unsafe Structure, and c) An Over-designed Structure

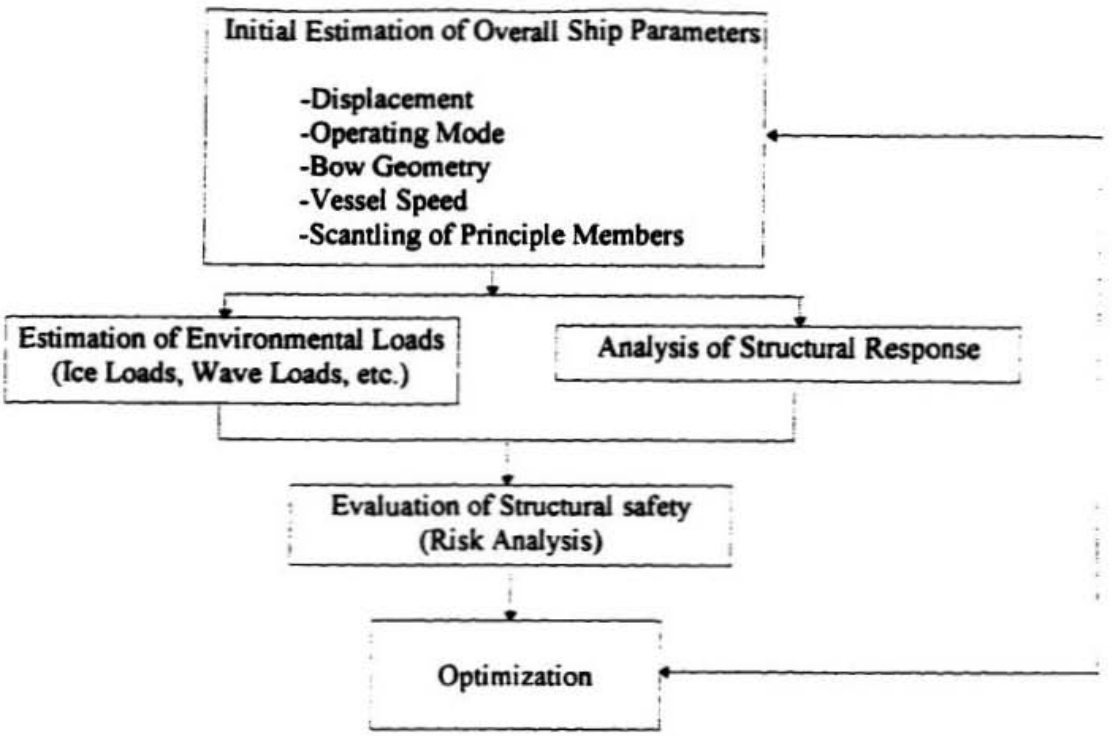

Figure 6. 3 Schematic View of the Process of Optimal Design of Structure

crucial to the preliminary design of a ship, which determines the location, spacing and scantlings of the principal members.

Reliability design offers several benefits including economy and safety. Since it involves an iterative process the aid of a computer is necessary to achieve cost effectiveness. The approach is also important in the formulation of the design code.

6.2.2 Code Design

In the design of ship structures, there are a large number of structural items. It would be inefficient to design all of them from first principles. A rule-based method is

more efficient in this case. Most of the structural items that come under detailed design are similar from ship to ship and in-service experience provides a sound basis for their design. A design code is usually formulated based on past experience and has intrinsic safety margins accepted in practice. Newer design codes are also calibrated using risk analysis (e.g. CSA S.471, the *ASPPR Proposals*).

A comprehensive review of different formats in rule-based design was carried out by Mansour et al., (1984) The most common format is the method of partial safety factors, which involves a specified load, x_s and a specified resistance r_s. The principles implied in x_s and r_s can be better explained by the probability density curves of X and R shown in Figure 6.4.

As illustrated in the figure, the specified load x_s, which most directly characterizes a particular situation, usually corresponds to a certain probability of exceedance, or to the n-year return period event. (n is generally 100). A load factor α is applied to x_s, resulting in the design load x_d:

$$x_d = \alpha x_s \,. \tag{6.2}$$

The value of the specified resistance, which is the basic unknown in the design problem, is obtained by applying a material factor β to the design load:

$$r_s = \frac{x_d}{\beta} = \frac{\alpha}{\beta} x_s \,. \tag{6.3}$$

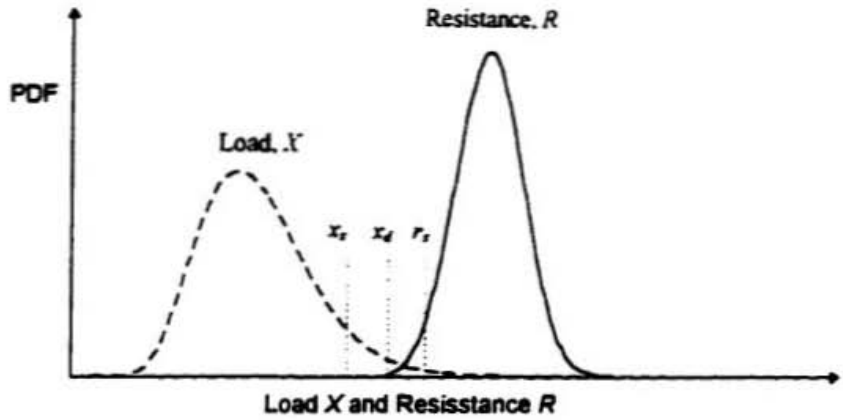

Figure 6. 4 Load-Resistance Problem

The purpose of the above procedure is to specify an extreme load that is exceeded on average once in *n* years. The safety factor is designed to take into account parameter uncertainty and uncertainties associated with load-event (e.g. ice load vs ice impact). The resistance factor characterizes similar uncertainties for the structural member.

For both optimal design and code formulation, it is important to understand the probabilistic nature of the load and resistance, which is investigated in the next two sections.

6.3 Design Load

The environmental loads for a ship hull include hydrostatic loads, wave loads, wind loads and ice loads. These forces are generally random in nature due to the varying environmental conditions. Here, we will focus our analysis on ice loads. An analysis on

extremal ice loads is described in Chapter 3. As we concluded, the fundamental issue in estimating extremal ice load is exposure, which is discussed first.

6.3.1 Exposure

The exposure of a structure to an ice hazard relates to duration of impacts (or, interactions), number of ice impacts, area of contact (design area) and position on ship (proportion of hits). The duration of impact relates to the nature of interaction (i.e. ice-breaking - ice ramming) and has been discussed in Section 3.5. Other factors are discussed below:

Expected number of impacts: As already illustrated in Figure 3.6 of Chapter 3, the probability density of extremal ice loads will shift to the right as the expected number of impacts increase. Such a number also indicates the ice capability of the structure. For instance, in *ASPPR Proposals*, each arctic class implies a range of expected number of impacts (Carter et al., 1992):

CAC1:	several thousand;
CAC2:	hundreds ,
CAC3:	decades ,
CAC4:	several .

The expected number of ice impacts for the tanker in the concept design ranges from 0.5 to 2 times per year. Another important aspect is that as the number of impacts

decreases, the load changes from frequent to rare, and the principles in selecting a design load need to be changed accordingly. This will be discussed in the following section.

Area Factors and Proportion of Hits: The exposure of the structure to ice impacts is different depending on the position of the structure. For instance, the bow region of an arctic vessel is more exposed to ice than the bottom region. In our extremal analysis on ice loads, this can be accounted for by the proportion of hits (i.e. r in Equation 3.11). In practical design, this can be accounted for by an area factor. For instance, in *ASPPR proposals*, area factors are suggested for different positions relative to the bow region as:

Position on the Hull	Area Factor
Bow Area	1.0
Appendage and Ice Skeg Area	2
Continual Ice Skeg Area	1.5
Middle Body and Stern Area	0.5
Bottom Area	0.3

Area of Contact: It has been found in field tests of different scales (Sanderson, 1988; Frederking et al. 1990) that the ice pressure decreases with the increase of the nominal contact area. This was further supported by the probabilistic analysis of local ice load of Jordaan et al, (1993a) and by the analysis on critical zones in Chapter 3. (see Figures 3.16 and 3.17). For design of plating, it is important to select an appropriate design area (unsupported area). Based on the analysis in Chapter 4 and the study by Brown,

Brown, (1993), an unsupported rectangle of $s \times 1.5s$ (s, frame spacing) is appropriate when the method in Chapter 3 is used to evaluate the extreme ice loads.

6.3.2 Specified Load and Load Factor

As we described earlier, in a code design, the design load is determined from a specified load x_s, and a load factor, α. Usually, three rules are used in the determination of a specified load. They are, first, to specify the annual maximum load with an exceedance probability, p_e, usually 0.01; second, to specify the load with a return period r, usually 100 years; third, to specify the most probable maximum load in r years. For a frequent load, the above mentioned three rules can arrive at the same or similar answer. This is schematically illustrated by Figure 6.5, in which, the return period is the reciprocal of the exceedance probability, and the most probable value of the '100 year maximum' also corresponds to the yearly maximum with $p_e = 0.01$. As learned from the development of CSA S.471 (e.g. Jordaan and Maes, 1991), among the above mentioned three rules, the first is more appropriate. This is because, first, the most probable maximum is difficult to interpret and may not even exist for a rare event; second, the return periods are often misinterpreted. For instance, a 100-year return period does not imply that one needs 100 years of data.

Environmental loads can be divided into three classes, namely frequent, occasional and infrequent loads. For frequent loads, a large number of events occur in an one-year period of time. Consequently, the probability density curve is very peaky as illustrated in Figure 6.6(a). Examples of this kind of loads are wind, wave, current and certain sea ice

loads. For occasional loads, the events are not as numerous as the former and result from intermittent processes or seasonal events. The probability distribution is spread

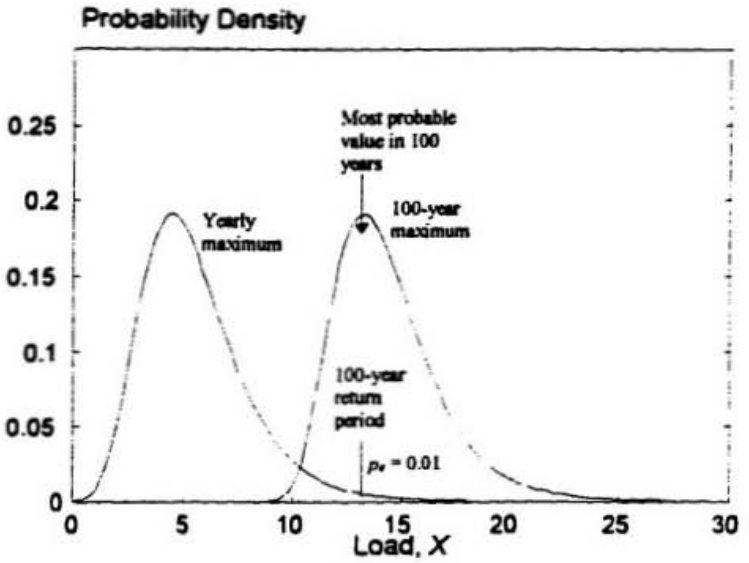

Figure 6. 5 Schematic illustration of different rules of specifying the load.

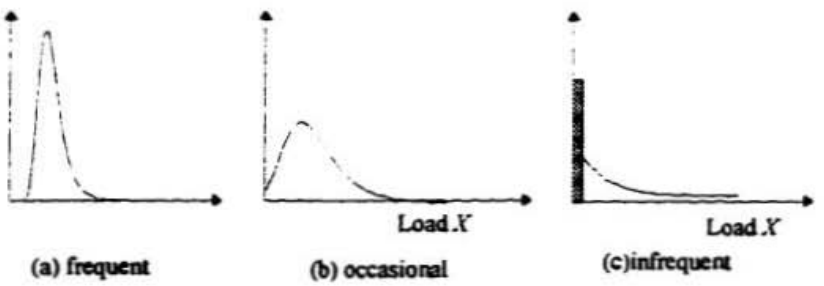

Figure 6. 6 Three classes of loads (Maes, 1986)

out over a much larger interval as shown in Figure 6.6 (b). For infrequent loads, such as earthquake and iceberg loads, events have a very low probability of occurrence. The probability density curve is characterized by a tail and a spike at zero as shown in Figure

6.6 (c). The selection of a design load depends on which kind of load is considered. For a frequent load or an occasional load, a specified load with an exceedance probability of 0.01 is usually used and a load factor is applied. For infrequent events the specified load usually has a low probability of exceedance, i.e., 10^{-3} to 10^{-4} and no load factor is applied to the design load.

It is also important to consider which limit state should be used for the design. Usually two limit states, i.e. serviceability and ultimate rupture, are considered. For a frequent load, it is essential to prevent any dent to the plating of the hull in order to maintain good serviceability. For an occasional load, such as multi-year ice impact to CAC4 class ships, both denting and rupture should be considered. The value of specified load depends on which limit state is considered. If the limit state is ultimate rupture, the specified load should be the 100 year load to ensure safety. For denting, certain judgment is needed. On one hand, allowing some denting will greatly reduce the cost of the structure; on the other hand, excessive denting means repeated repair and is uneconomical. The designer has to find an appropriate balance. In this case, an optimization such as the one carried out by Brown (1993) is appropriate. For a rare event, the limit state should be ultimate rupture. The denting in this case is judged as acceptable.

The purpose of the load factor is to further reduce the probability of exceedance for the design load. For instance, applying a safety factor of 1.35 to a 100-year load may yield a design load with the probability of exceedance of 10^{-4}. However, such a safety factor does not give the same safety margin to loads with all exposure as found by Maes

(1986). To appreciate this, let us analyze the ice load on a 0.54 m^2 plate panel. The 100-year loads for different exposure (expected number of impacts) obtained from Equations

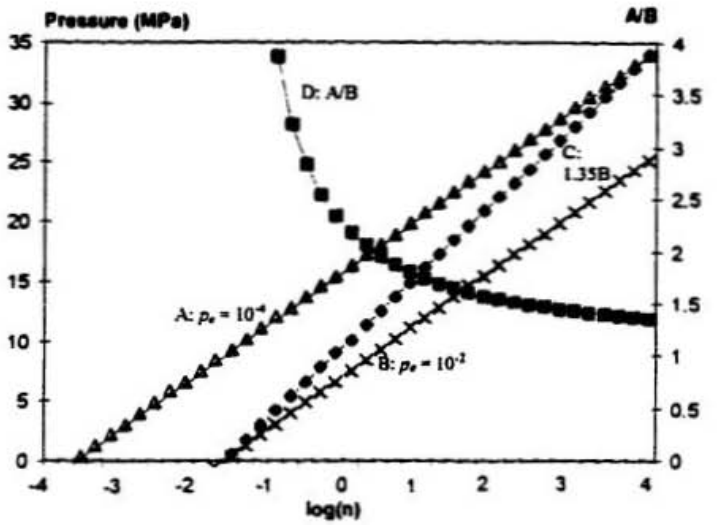

Figure 6. 7 Relationship between Safety Factors and Exceedance Probability

(3.9) and (3.14) are plotted in Figure 6.7 (curve B). Loads corresponding to a probability of exceedance of 10^{-4} are also plotted in the figure (curve A). A safety factor of 1.35 is applied to 100-year loads and yields the design loads which are also plotted in Figure 6.7 (curve C). As indicated in the figure, the load factor of 1.35 results in a design load with a probability of exceedance of 10^{-4} in the case when the expected number of impact is 10000; the same factor results in a design load with approximately no improvement in exceedance probability for design load when the exposure 0.1 per year. The figure also shows values of load factors (curve d: *A/B*) necessary to give a design load with an uniform probability of exceedance of 10^{-4}. The results show that values of the safety factor

factor range from 1.35 to 4. It is concluded that use of a load factor is not appropriate for rare loads.

6.3.3 Design Ice Load for the Concept Design

The main ice hazards for the concept design of this chapter are iceberg impacts. The expected number of impacts are very small. Fuglem et al., (1996) showed that, for a shuttle tanker traveling in Newfoundland waters, the expected number of impacts ranges from 0.1 to 4 depending on the traveling route and the ice conditions. Tentatively we specify the expected number of impact as one per year. The ice load in this case is an infrequent one and the specified load should correspond to a low exceedance probability.

In selecting a design load, one has to bear in mind that most designers are used to the method of partial safety factor; and the load with 10^{-4} seems to be "unrealistic". For this reason, we propose a number of strategies in selecting the design load. This includes the loads which correspond to 10^{-2},10^{-3} and 10^{-4} exceedance probabilities, and with safety factors ranging from 1 to 2.4. We will calculate the safety for each strategy in Section 6.5.

6.4 Resistance of the Structure

In Chapter 4, we proposed to model the strength of a plate by a long plate loaded by uniform pressure. The resistance for plastic collapse and rupture from the design model are:

$$R_{1A}^{d} = \frac{16M_p}{s^2} \text{ , and} \qquad (6.4)$$

$$R_u^d = 1.03\sigma_y^* \frac{t}{s} \quad . \tag{6.5}$$

respectively, where M_p is the plastic moment resistance; s is frame spacing, t is the thickness of the plate and σ_y^* is the dynamic yield stress. As we know from Chapter 5, the realistic ice load is not uniform. This causes uncertainties in the design model. For plastic collapse, this uncertainty can be represented by a random factor B_{3h}. B_{3h} can be approximated by a lognormal distribution with a mean value of 1.553 and a *COV* of 0.206. In addition, M_p is also random due to the uncertainties in material strength and sizes. According to Maes (1986) and Kennedy and Baker (1984), M_p has a lognormal distribution with a mean of $1.22M_{ps}$ and a *COV* of 0.1, where M_{ps} is the specified plastic moment resistance. If we denote the random quantity M_p as B_{3f}, the real resistance of the plate can be presented as:

$$R_{3h} = \frac{16}{s^2} B_{3f} B_{3h} \quad . \tag{6.6}$$

A special point to note is that, in the case that both B_{3f} and B_U have lognormal distributions, $R_{3h} = 16B_{3f}B_u / s^2$ also has a lognormal distribution (Ochi, 1990). The mean and *COV* of R_{3h} can be derived as $1.895(16M_p/s^2)$ and 0.227 respectively.

In case of ultimate rupture, the probability distribution of the real resistance can be derived similar to the case of three-hinge collapse. The uncertainty of the material properties include yield strength σ_y^* and plate thickness t. According to Nessim (1991) and Kennedy and Baker, (1984), the yield stress of steel has a lognormal distribution. The mean and *COV* of this distribution are suggested as $1.08\sigma_{ys}$ and 0.05 respectively

(Galambos and Ravindra, 1978), where σ_{yz}. Is the specified yield stress. We assume that the plate thickness also has a lognormal distribution. The mean and *COV* of the plate thickness is assumed as $1.014t_s$ and 0.01 respectively according to Kennedy and Aly (1980), where t_s is specified plate thickness. Consequently, $\sigma^*_y t$ also has a lognormal distribution with a mean of $1.095\sigma^*_{ys}t_s$ and a *COV* of 0.051. The resulting strength of the plate R_u, has a lognormal distribution with a mean of $1.371(1.03\sigma_{ys}{}^*t_s^2/s)$ and a *COV* of 0.182.

6.5 Design of the Plating

In the present section, the plating is designed to resist ice impact load. Consideration of other environmental forces is not included. Both the method of reliability design and the partial safety method are used in deriving plate thickness. Different strategies are used to define design load. The expected number of impact with icebergs is one per year. For such infrequent events, ultimate rupture is considered as the limit state for plate failure. Three hinge collapse is considered acceptable. Plate thickness is calculated from the design model (Equation (6.5). EH-36 steel is used for plating following the suggestions in Carter et al. (1992). The dynamic yield and dynamic ultimate stresses of the steel are used as the material strength. Probability distributions of ice load and pressure strength defined in Section 6.3 and 6.4 are used in risk estimates. The probability of failure is calculated using First Order Reliability Method (FORM, Gollwitzer et al., 1988).

6.5.1 Dynamic Yield and Dynamic Ultimate Stresses

Since the ice-structure impact is characterized by high speed and short duration, we will use dynamic yield and dynamic ultimate stress in calculating the plate strength. The calculation of these stresses are based on the work of Nessim et al. (1992).

The dynamic yield stress of structural steel is dependent (among other factors) on the service temperature and the strain rate. Results of Soroushian and Choi (1987) were used to calculate the actual dynamic stress from specified (static) yield stress. The ratio between the yield stress at strain rate ε, $\sigma_{dyna}(\varepsilon)$ and the static yield stress, $\sigma(0)$, is given as follows:

$$\frac{\sigma_{dyna}(\varepsilon)}{\sigma_y(0)} = -0.31\times10^{-4}\sigma_y(o)+1.46\}+\{-0.634\times10^{-4}\sigma_y(0)+0.093\}\log(\varepsilon). \qquad (6.7)$$

The actual yield stress also depends on the temperature. This dependence was characterized using data given by Malik and Tomin (1991). This data is for EH-36 steel with a specified yield stress of 355 MPa, and the tests were carried out at a strain rate of $5x10^{-2}\cdot s$. The ratio of the actual yield stress at temperature T, $\sigma_y(T)$, to the specified yield stress, σ_{ys}, can be calculated based on the test data:

$$\frac{\sigma_y(T)}{\sigma_{ys}} = 1.14 - 0.004T, \qquad (6.8)$$

where T is in $°C$. Equations (6.7) and (6.8) are used to estimate the dynamic yield stress for any combination of temperature and strain rate.

A similar analysis on dynamic ultimate stress was also carried out by Nessim et al., (1992). The analysis was based on the same data set reported by Malik and Tomin (1991). The ratio between $\sigma_{ult}(T)$ and σ_{ys} as a function of the temperature is derived:

$$\frac{\sigma_{ult}}{\sigma_{ys}} = 1.62 - 0.003T. \tag{6.9}$$

The strain rate effect is given by the following relationship (Soroushain and Choi, 1987):

$$\frac{\sigma_{ult}(\varepsilon)}{\sigma_y(\varepsilon)} = \{-0.47 \times 10^{-7}\sigma_y(0) + 1.72\} + \{-0.944 \times 10^{-8}\sigma_y(0) + 0.144\}\log(\varepsilon), \tag{6.10}$$

where $\sigma_{ult}(0)$ and $\sigma_y(0)$ are the static yield and ultimate stresses respectively. Equations (6.9) and (6.10) can be used to calculate the ultimate strength for any combination of temperature and strain rate.

The temperature used in present analysis is $0°C$ and the strain rate is 10^{-2}. The corresponding dynamic yield stress and dynamic ultimate stress was calculated and is summarized below:

Material	EH36 Steel
Temperature °C	0
Strain rate ε	10^{-2}
σ_y (MPa)	355
σ_{dyna} (MPa)	388
σ_{ult} (MPa)	537
$\sigma^*_y = (\sigma_{dyna} + \sigma_{ult})/2$ (MPa)	462.5

6.5.2 Design of Plate Thickness and Risk Analysis

Reliability Design:

The objective of the design is to find a minimum plate thickness which satisfies the target safety. The accepted range of target values of annual reliability in offshore industry is 1-(10^{-4} to 10^{-5}). For shipping, a higher reliability is desirable. The value of 1-10^{-6} is chosen as our target value of annual reliability following the suggestion by Carter et al., (1995). An iterative process is carried out. In each iteration, a plate thickness is chosen and the probability density of the resistance is derived. The probability density function of ice load for an unsupported area of 0.54 m^2 can be derived from the method presented in Chapter 3. The probability of failure is then calculated. The probability of failure is plotted against the plate thickness in Figure 6.8. The optimal plate thickness, which corresponds to a failure probability of 10^{-6}, is 29 mm. The figure also shows the failure probability against the plate thickness for the case when the average rams per year, n, is 0.5 and 5. The plate thickness varies between 27 to 33 mm for n between 0.5 to 5. For the purpose of comparison, plate thickness for Arctic class CAC4 and for the Baltic class 1AS and open water were also calculated and are presented in Table 6.2. It shows that, for the present vessel, significant ice strengthening is required. The thickness is between that of the Baltic class 1AS vessel and the open water.

Method Using Partial Safety Method

In the following, we use the method of partial safety factor (Equation 6.3) to design the plate thickness. First, we calculate the specified load, x_s. Ice loads which corre-

correspond to 1%, 0.1% and 0.01% of exceedance probabilities are used as the specified load x_s. The design load is then calculated by applying a safety factor α to the specified load. Values of α ranging from 1.0 to 2.4 are used. The specified strength is then obtained by applying a material factor β to the design load. β usually equals to 0.75.

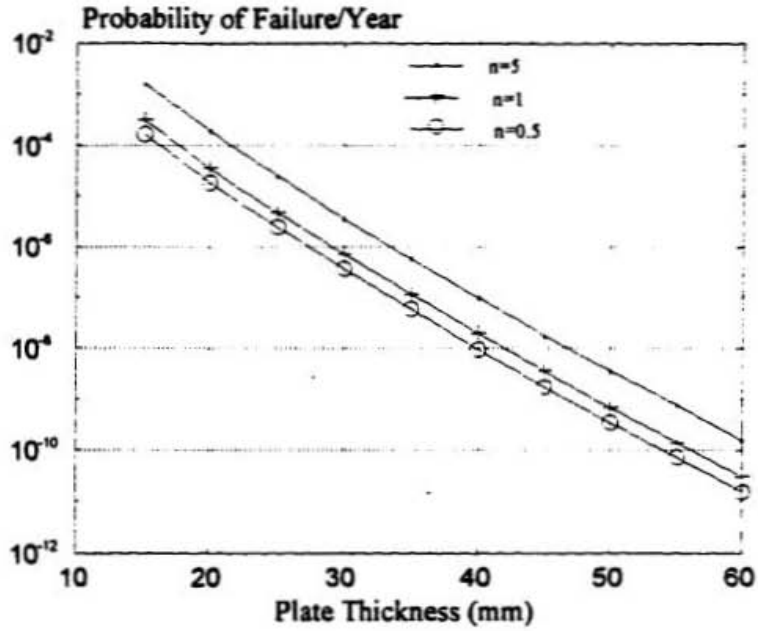

Figure 6. 8 Probability of Failure for Different Plate Thickness

Table 6. 2 Plate Thickness for Different Class Ships

Class of Ship	Plate thickness (mm)
Reliability Design	29-30
Arctic Class CAC4	36
Baltic Class 1AS	30
Open Water	16

Once the specified resistance is selected, the plate thickness can be calculated using Equation (6.5). Values of plate thickness corresponding to different strategies are calculated and results are presented in Figure 6.9. The probability distribution of ultimate strength corresponds to each plate thickness is then derived from the results of Section 5.4 and the probability of failure is calculated using FORM. The results are presented in Figure 6.10. As shown in the figure, the combinations of a specified load with 10^{-4} exceedance probability and a safety factor α = 1, and a specified load with 10^{-3} exceedance probability and a safety factor α = 1.48 satisfy the target safety value of 10^{-6}. The probability density for three hinge failure was also derived for each plate thickness and the probability of failure is calculated. The results are shown in Figure 6.11. As expected, the probability of three hinge collapse is high.

6.6 Conclusions and Recommendations

Structural design can be viewed as a decision process. The main objective is to achieve required safety at minimum cost. This can be achieved by a risk analysis. Two design methods, namely the reliability design method and the partial safety method, are introduced and are applied to design of the plating of a concept design. To achieve an optimal design of the structure, it is essential to understand the uncertainties associated with the load and structure strength. Environmental load can be divided into three categories, namely frequent, infrequent and rare loads; accordingly, different strategies are

needed in specifying the design load. The partial safety method is most suitable for the design of frequent loads but not suitable for rare events. The limit states design includes serviceability and ultimate failure. The limit state for a particular design also depends on the kind of environmental loads considered. For frequent loads, serviceability should be considered, while in a rare event the main consideration is the ultimate safety.

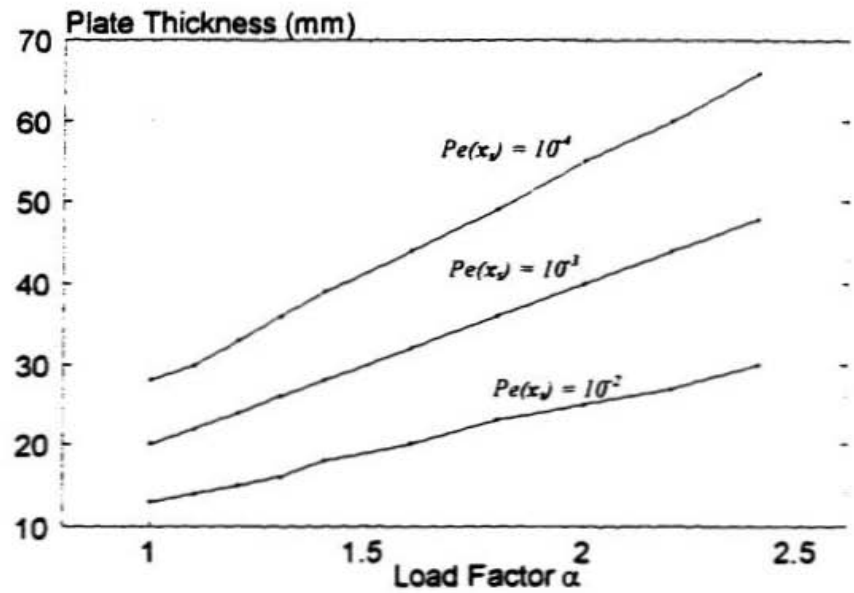

Figure 6. 9 Plate Thickness for Different Design Strategies

Through the design of plating for an oil tanker for Offshore Newfoundland, for rare loads such as the ice loads from the iceberg impacts, the design load can be chosen as the one with a probability of exceedance of 10^{-4}. It was also found that a class between Baltic class 1AS and open water needs to be developed for the design for Offshore Newfoundland waters.

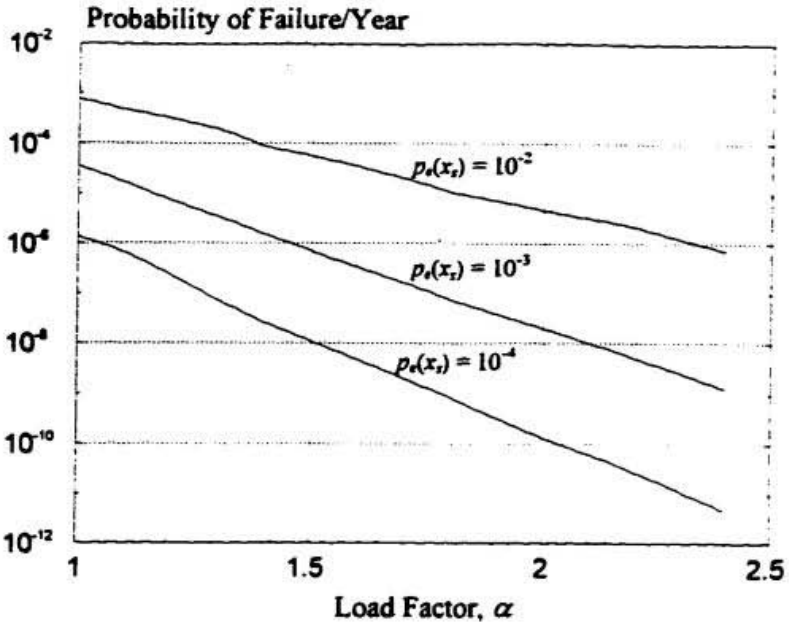

Figure 6. 10 Probability of Failure (ultimate Rupture)

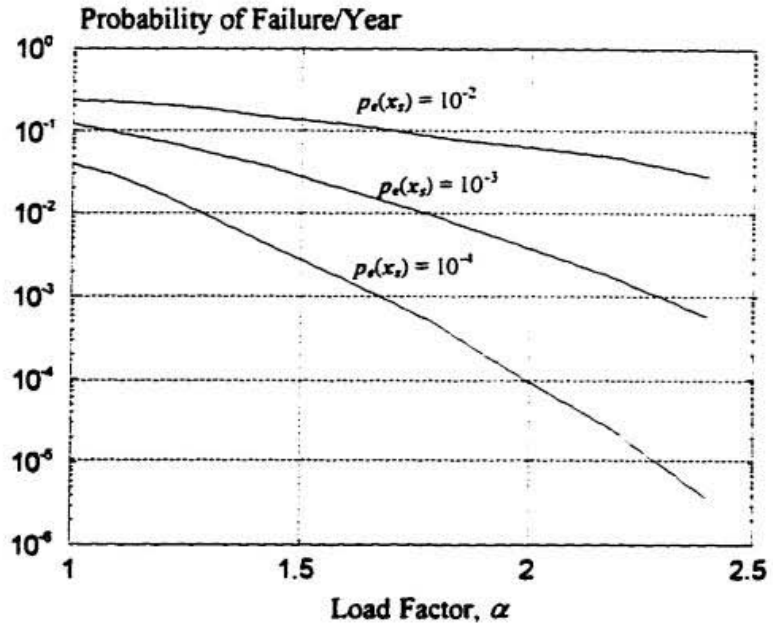

Figure 6. 11 Probability of Failure (Three hinge Failure)

Chapter 7 Concluding Remarks

A comprehensive analysis of ship structural design for ice environments has been presented. Mechanics of ice-structure interaction, statistics of ice loads and an analysis of the structural response to ice loads were identified as three important and interlinked aspects in the structural design. Localized high pressures (critical zones), the key element in all of these aspects, are the focus of the present work.

From the view point of mechanics, ice impacts are characterized by ice fracture and damage. This leads to pieces of ice spalling off and formation of critical zones. The fracture process governs the size and location of these critical zones. Kendall's double cantilever beam is not suitable for the analysis of ice fracture since it is limited to the case of a long central crack. The model of Hutchinson and Suo accounts for both shear and tensile fractures and may provide a better solution for ice spalling. Since this model is also derived for the case of a long crack, further development is needed for the modelling of critical zones. In reality cracks are small compared with the size of the ice feature. These cracks, under the mixed mode of stresses, are the likely candidates for fracture spalling. Due to the randomness of these cracks, spalling resulting from fracture and critical zones are also random. As a result, critical zones are also random.

A probability distribution of ice loads can be estimated by probabilistic modelling of critical zones. The ice loads on a design area can be assumed as a random number of critical zones, each with a random force. The probability distribution of the maximum ice

loads can be approximated by a double exponential distribution. This distribution is dependent on the exposure of the structure to the ice loads. The exposure is related to the design area, location of the structure and the design route for ship operations .

For the design of ship plating, a long plate model is considered appropriate. This has the advantage of been easily implemented by designers. The ice load on this plate can be estimated from the yearly maximum load on a panel with an aspect ratio of 1.5. It should be kept in mind that the real structure and the ice loads are quite different from the idealization, and therefore model uncertainty associated with this idealization should be considered in design.

A plate under localized loads such as critical zonal forces usually fails in a dominant section. This dominant failure section behaves in a similar way to a 2-D plate loaded by non-uniform pressure. The failure of this 2-D plate can be estimated by the simple model derived in this study. In addition to the dominant section, additional factors affecting the failure of the plate include the lateral support, the location of critical zones and the interaction between critical zones. These factors can also be estimated by the empirical formulae derived in this study.

The real strength of a structure can be calculated using the design strength and a factor of model uncertainty. In the present study this factor is a random quantity which can be approximated by a lognormal distribution. In addition to the model uncertainty in ice load, uncertainties also exist in material strength and sizes.

Reliability design yields an optimal solution yet it is difficult to implement in practice. For the load factor design method, care must be taken when selecting the specified load. For rare loads such as ice impact loads in offshore Newfoundland waters, the load factor does not always increase the safety by the "expected amount". As a result, this method is not appropriate in the design of a structure for a rare event. The characteristics of ice loads in offshore Newfoundland waters are quite different from that of the Baltic and the Canadian arctic. A design rule for ships operating in this region is needed. The present study can be used in the development of such a rule.

Reference

Ayuub, B.M., White, G.J. and Purcell, E.S., 1989, "Estimation of Structural Service Life of Ships", Naval Engineers Journal, ASNE, Vol. 101, No. 3, pp.156-166.

Baker, 1956, **The Steel Skeleton**, Vol 2, Cambridge University Press.

Blanchet, D., 1990, "Thirteenth Canadian Geotechnical Colloquium: Ice Design Criteria For Wide Arctic Structures", Canadian Geotechnical Journal, Vol 27, No. 6, pp. 701-725.

Blount, H., Glen, I.F., Comfort, G. and Tam, G., 1981, "Results of Full Scale Measurements Aboard CCGS Louis St. Laurent During a 1980 Fall Arctic Probe", Report for Canadian Coast Guard by Arctec Canada Ltd., Vol I and II.

Brown, P., 1993, "Optimal Design of Bow Plating for Ships Operating in Ice", M.Eng. Thesis, Memorial University of Newfoundland.

Carter, J., Daley, C., Fuglem, M., Jordaan, I., Keinonen, A., Revill, C., Butler, T., Muggeridge, K., Zou, B., 1996, "Maximum Bow Force for Arctic Shipping Pollution Prevention Regulations - Phase II", Ocean Engineering Research Centre, Memorial University of Newfoundland, Report Prepared for Transport Canada, Ship Safety Northern, Report Number TP 12652, p. 443.

Carter, J., Daley, C., Fuglem, M., Jordaan, I.J., Keinonen, A., Zou, B., 1995, "Maximum Bow Force For Arctic Shipping Pollution Prevention Regulations", Report for Canadian Coast Guard Arctic Ship Safety by Ocean Engineering Research Centre, Memorial University of Newfoundland.

Carter, J.E., Frederking, R.M.W., Jordaan, I.J., Milne, W.J., Nessim, M.A., and Brown, P.W., 1992, "Review and Verification of Proposals for the Revision of the Arctic Shipping and Pollution Prevention Regulations", Final Report, Transport Canada Report No. TP 11366E, Memorial University of Newfoundland, St. John's, Newfoundland.

Conrad, N., 1976, "On Microcrack Growth and Arrest in Simulated Fibrous Composites", Mechanics and Materials Research Center, Texas A & M University, College Station, Report MM 3168-76-10.

Cotterll, B., and Rice, J.R., 1980, "Slightly Curved or Kinked Cracks", International Journal of Fracture Mechanics, Vol. 16, pp.155-169.

Daley, C.G., Ferregut, C. and Brown, R., 1991, "Structural Risk Model of Arctic Shipping", In the proceedings of the IUTAM/IAHR Symposium on Ice-Structure Interaction, St. John's, NFLD, August 1989, Springer Verlag, pp. 507-540.

Daley C.G. and Riska, K., 1990, "Review on Ship-Ice Interaction Mechanics", Report from Finish-Canadian Joint Research Project No. 5, 'Ship Interact With Actual Ice Conditions', Interim Report on Task 1A.

Daley, C.G., St. John, J.W., Brown, R. and Glen, I., 1986, "Consolidation of Local Ice Impact Pressure Measured Aboard USCGC Polar Sea (1982-1984), Report No. TP 8533E, submitted to Transportation Development Center, Arctec Canada Limited, Kanata, Ontario, 214 p.

DeFranco, S.J., Dempsey, J.P., 1990, "Crack Growth Stability In S2 Ice", IAHR Ice Symposium, Espoo.

Dempsey, J.P., Wei, Y., DeFranco, S., Ruben, R., and Frachetti, R., 1989, "Crack Length and Specimem Size Effects, Part I, Proceedings of 8th International Conference on Offshore Mechanics and Arctic Engineering, The Hugue, Holland, Vol. IV, pp83-89.

Dome Petroleum Ltd., 1982, "Report on Full Scale Measurement of Ice Impact Loads and Response of the 'Canmar Kigoriak' -August and October 1981", Prepared by Dome Petroleum Ltd.

Egge, E.D. and Böckenhauer, M., 1991, "Calculation of the Collision Resistance of Ships and its Assessment for Classification Purposes", Marine Structures: Design, Construction and Safety, Vol. 4, No. 1, pp.35-56.

Evans, A.G., Palmer, A.C., Goodman, D.J., Ashby, M.F., Hutchinson, J.W., Ponter, A.R.S. and Williams, G.J., 1984, "Indentation Spalling of Edge-loaded Ice Sheet", IAHR Ice Symposium, Hamburg.

Finish-Swedish Ice Class Rules, 1989, "Board of Navigation Rules for Assigning Ships Separate Ice Due Classes", Helsinki.

Frederking, R.M.W., Jordaan, I.J. and McCallum, J.S., 1990, "Field Test of Ice Indentation at Medium Scale, Hobson's Choice Ice Island", Proceedings of 10th IAHR Symposium on Ice, Espoo, Finland, Vol. 2, pp. 931-944.

Fuglem, M.K., Jordaan, I.J. and Crocker, G., 1996, "Iceberg-Structure Interaction Probabilities for Design". Accepted for publication by the Canadian Journal of Civil Engineering.

Galambos, T. and Ravindra, M.K., 1978, "Properties used in LRFD", ASCE, Journal of Structural Engineering, Vol. 104, No. ST9, September.

Glen, I.F. and Blount, H., 1984, "Measurement of Ice Impact Pressure and Loads Onboard CCGS Louis S. St. Laurent", Offshore Mechanics and Arctic Engineering Symposium, New Orleans, Vol. III, pp. 246-252.

Gollwitzer, S., Abado, T., Rackwitz, R., 1988, First Order Reliability Method (FORM). RCP GmbH, Munich, West Germany.

Hallam, S.D., 11986, "The Role of Fracture in Limiting Ice Forces", Proceedings of IAHR Ice Symposium, 1986, Vol. 1, Iowa City.

Hill, R., 1950, **The Mathematical Theory of Plasticity**, Clarendon Press, Oxford.

Hughes, O.F., 1988, **Ship Structural Design - A Rational-Based, Computer-Aided Optimization Approach**, 2nd edition, The Society of Naval Architects and Marine Engineers, Jersey City, NJ

Hutchinson, J.W., and Suo, Z., 1992, "Mixed Mode Cracking in Layered Materials", **Advances in Applied Mechanics**, Academic Press, Volume 29, pp. 63-191.

Jefferies, M.G. and Wright, W.H., 1988, "Dynamic Response of Molikpaq to Ice Structure Interaction", OMAE'88, Vol IV, pp.790-799.

Johnston, M., Milord, P., Stone, B., Xiao, J., Zou, B., Jordaan, I.J., 1993, "Ice Load Modeling: Development and Implementation", Report for National Energy Board by Memorial University of Newfoundland.

Johnston, M., 1993, "Variation of Local Pressures During Ice-Structure Interaction", M.Eng. Thesis, Memorial University of Newfoundland.

Jordaan, I.J., Xiao, J. and Zou, B., 1993 "Fracture and Damage of Ice: Towards Practical Implementation", The 1st Joint Mechanics Meeting of ASME, ASCE, SES MEET'N'93, Charlottesville, Virginia, AMD-Vol. 163, pp.251-260.

Jordaan, I.J., Maes, M.A., Brown, P.W. and Hermans, I.P. 1993a, "Probabilistic Analysis of Local Ice Pressure", Journal of Offshore Mechanics and Arctic Engineering, ASME, Vol 115, No. 1, pp. 83-89.

Jordaan, I.J. and Maes, M., 1991, "Rationale for Load Specifications and Load Factors in the New CSA Code for Fixed Offshore Structures", Canadian Journal of Civil Engineering, Vol. 18, No. 3, pp.454-464.

Jordaan, I.J. and McKenna, R.F., 1988, "Modelling of Progressive Damage in Ice", IAHR Symposium on Ice, Sapporo, Japan, August, Proceedings Vol II, pp.585-624.

Jordaan, I.J., 1987, "Probabilistic Analysis of Environmental Data for Design of Fixed and Mobile Arctic Offshore Structures", Reliability and Risk Analysis in Civil Engineering, Proceedings of 5th International Conference on Applications of Statistics and Probability in Soil and Structural Engineering, Vancouver, B.C., May 25-29, Vol. 2, pp. 1130-1137.

Jordaan, I.J., Nessim, M.A., Ghoneim, G.A. and Murray, A.M., 1987, "A Rational Approach to the Development of Probabilistic Design Criteria for Arctic Shipping", Proceedings, 6th Offshore Mechanics and Arctic Engineering Symposium, Houston, Vol. IV, pp. 401-406.

Jordaan, I.J., 1982, "Decision Analysis Applied to Problems of Structural Code Formulation", Proceedings, NATO Advanced Study Institute on Reliability Theory and Its Application in Structural and Soil Mechanics. Bornholm, Denmark.

Kachanov, M., 1993, Elastic Solids with Many Cracks and Related Problems. Advances in Applied Mechanics, Vol 30, Academic Press.

Kärnä, T., and Muhonen, A., 1990, "Preliminary Results from Ice Indentation Tests Using Flexible and Rigid Indentors", IAHR Ice Symposium, Espoo, Finland, Vol. 3, pp.261-275.

Karr, D.G. and Choi, K., 1989, "A Three-Dimensional Constitutive Damage Model for Polycrystalline Ice", Mechanics of Materials, Vol. 8, pp. 55-66.

Kendall,K., 1978, "Complexities of Compression Failure" Proceedings of the Royal Society of London, Vol. A361, 1978, pp. 245-263.

Kennedy and Baker 1984, Resistance Factors for Steel Highway Bridge, Canadian Journal of Civil Engineering, Vol. 11.

Kennedy, K. and Gad Aly, M., 1980, "Limit States Design of Steel Structure - Performance Factors, ", Canadian Journal of Civil Engineering, Vol. 07.

Kheysin, D. Ye., 1973a, "Use of Probability Methods in Estimating the Maneuvering Qualities of Ships in Ice", Ice Navigation Qualities of Ships, Edited by D. Kheysin and Yu. Popov, CRREL Translation, pp. 19-39.

Kheysin, D. Ye. 1973b, "On the Ice Navigation Speed of Ships in Extremely Solid Ice", Ice Navigation Qualities of Ships, Edited by D. Kheysin and Yu. Popov, CRREL Translation, pp. 40-57.

Kujala, P.J., (1991), "Safety of Ice Strengthen Ship Hulls in the Baltic Sea", Transactions of the Royal Institute of Naval Architects, Vol 133, Part A, London, UK, pp83-94.

Kujala, P.J., (1994), **On the Statistics of Ice Load on Ship Hull in the Baltic,** (Ph.D thesis), ACTA POLYTECHNIC SCANDINAVICA Mechanical Engineering series No. 116.

Likhomanov, V.A., 1973, "The Strength of Icebreakers and Transport Vessels", Ice Navigation Qualities of Ships, Edited by D. Kheysin and Yu. Popov, CRREL Translation, pp. 115-126.

Maes, M.A., Hermans, I.P., 1991, "Review of Methods of Analysis of Data and Extreme Value Techniques for Ice Loads", Queens University, Kingston, ON, 83p.

Maes, M.A., 1986, "A Study of a Calibration of the New CSA Code for Fixed Offshore Structures", Report for Report for Canada Oil and Gas Land Administration (COGLA) by Net Norske Veritas, March.

Maes, M.A., Jordaan, I.J. and Cormeau, A., 1986, "Probabilistic Theories For the Failure of Sea Ice", International Conference on Ice Technology, MIT, Boston, pp. 37-54.

Maes, M.A., 1985, "Extremal Analysis of Structural Loads", Ph.D Thesis, University of Calgary.

Maes, M.A., Jordaan, I.J., Appleby, J., and Fidjestoel, P., 1984, "Risk Assessment of Ice Loading for Fixed Structures", Proceedings, 3rd International Offshore Mechanics and Arctic Engineering Symposium, New Orleans, February, pp. 220-227.

Malik, L and Tomin, M., (1991), Evaluation of Toughness of Conventional Ship Steels at Intermediate Loading Rate and its Implications", Unsolicited Proposal A7-026, Marine Technology Center Report No. E73331C, Fleet Technology Ltd., Kanata, ON, and Reltec Advisory Services, Calgary, AB.

Mansour, A.E., Jan, H.Y., Zigelman, C.I., Chen, Y.N. and Harding, S.J., 1984, "Implementation of Reliability Methods to Marine Structures". SNAME Transactions, Vol. 92, pp. 353-382.

McDermott, J.F., Kline, R.G., Jones Jr., E.L., Maniar, N.M. and Chiang, W.P., 1974, "Tanker Structure Analysis", Transactions, The Society of Naval Architects and Marine Engineers, Jersey City, NJ, Vol. 82, pp.382-414.

McKenna, R.F., Meyssonnier, J. and Jordaan, I.J., 1989, "Peak Pressure From a Damage Model for Ice in Compression", Proceedings of 8th International Conference on Offshore Mechanics and Arctic Engineering, The Hague, Netherlands, Vol. IV, pp. 67-73.

Melville Shipping Ltd., 1989, "Proposals for Revision of the Arctic Shipping Pollution Prevention Regulations", Transport Canada Report No. TP 9981E, Melville Shipping Ltd, Ottawa, ON.

Nessim, M.A., Hong, H.P. and Stephens, M.S. (1992), "Reliability Based Assessment of Hull Failure and Brittle Fracture of Ships Designed to ASPPR", C-FER report 90-35

Nessim, M.A. and Jordaan, I.J., 1991, "The Selection of Design Ice Load and Design Ice Features for Fixed Structures in the Beaufort Sea", Proceedings, IUTAM-IAHR Symposium on Ice-Structure Interaction, St. John's, Newfoundland, August 1989, Springer-Verlag, pp.483-506.

Nessim, M.A., Cheung, M.A. and Jordaan, I.J., 1987, "Ice Action on Fixed Offshore Structures - A State-of-the-Art Review", Canadian Journal of Civil Engineering, Vol. 14, No. 3, June, pp. 381-407.

Ochi, Michel K., 1990, **Applied Probability and Stochastic Process In Engineering and Physical Sciences**, John Wiley & Sons

Ochi, Michel K., 1981, "Principles of Extreme Value Statistics and their Application", presented at Extreme Loads Response Symposium, Arlington, VA, October 19-20, 1981.

Palaniswamy, P. and Knauss, W.G., 1974, "On the problem of Crack Extension in Brittle Solids Under General Loading", California Institute of Technology, SM-74-8.

Paulling, J.R. (1988), "Strength of Ships", Principles of Naval Architecture, ed. E.V. Lewis, The Society of Naval Architects and Marine Engineers, Jersey City, NJ, Vol. I, Chapter IV, pp.205-299.

Ratzlaff, K.P. and Kennedy, D.J.L., 1985, " Analysis of Continuos Steel Plates Subjected to Uniform Transverse Loads", Canadian Journal of Civil Engineering, Vol. 12, No. 3, pp.685-699

Sanderson, T.J.O., 1988, **Ice Mechanics: Risks to Offshore Structures**, Graham and Trotman Ltd., London, U.K.

Schapery, R.A., 1981, "On Viscoelastic Deformation and Failure Behaviour of Composite Material With Distributed Flaws", Advances in Aerospace Structure and Material, Ed., S.S. Wang and W.J. Renton, The American Society of Mechanical Engineers.

Schapery, R.A., 1991, "Models for the Deformation Behaviour of Viscoelastic Media with Distributed Damage and Their Applicability to Ice", In the proceedings of the IUTAM/IAHR Symposium on Ice-Structure Interaction, St. John's, NFLD, August 1989, Springer Verlag, pp. 191-230.

Shackelford, James F., 1988, **Introduction to Materials Science for Engineers** (second edition), Macmillan Publishing Company

Shen, W. and Lin, S.Z., 1986. "Fracture Toughness of Bohai Bay Sea Ice", Proceedings of the Fifth International Conference on Offshore and Arctic Engineering (OMAE), Vol. IV, pp.354-357.

Sih, G.C., 1973, "A Special Theory of Crack Propagation", in Mechanics of Fracture 1, Methods of Analysis and Solutions of Crack Problems, Ed. G.C. Sih, Nordoff, Leyden, pp. XXI-XLV.

Sih, G.C., and Tzou, D.Y., 1983, "Mechanics of Nonlinear Crack Growth: Effects of Specimen Size and Loading Steps", Conference on Modelling Problems in Crack Tip Mechanics.

Smith, T.R., and Schulson, E.M., 1991, "The Brittle Compressive Failure of Freshwater Columnar Ice Under Biaxial Loading", Proceedings of OMAE, Vol. IV, pp.207-214.

Soroushian, P., and Choi, K., 1987, "Steel Mechanical Properties at Different Strain Rates", Journal of Structural Engineering, ASCE, Vol. 113, No. 4, pp.663-672.

Suo, Z., 1990, "Delamination Specimens For Orthotropic Materials", Journal of Applied Mechanics, 57, pp627-634.

Timco, G. and Frederking, R.M.W., 1986, "The Effects of Anistropy and Microcracks on the Fracture Toughness of Freshwater Ice", Proceedings of Fifth International Offshore Mechanics and Arctic Engineering (OMAE), Tokyo, Japan, Vol. IV, pp.341-348.

Varsta, P., (1983), "On the mechanics of ice load on ships in level ice in the Baltic Sea", Espoo. VTT Publications 11, 91p.

Wiernicki, C.J., 1987, "Damage to Ship Plating Due to Ice Impact Loads", Marine Technology, Vol. 24, No. 1, pp. 43-58.

Wood, R.H., 1961, **Plastic and Elastic Design of Slabs and Plates**, Ronald Press, New York.

Xiao, J., Jordaan, I.J., 1991, "Modeling of Fracture and Production of Discrete Ice Pieces", Report for Canada Oil and Gas Land Administration (COGLA) by Ian Jordaan and Associates Inc.

Xiao, J., Jordaan, I.J., 1996, "Application of Damage Mechanics to Ice Failure in Compression", Parts I and II (in preparation).

Zou, B., Xiao, J., Jordaan, I.J., 1996, "Fracture and Spalling in Ice-Structure Interaction", accepted by Cold Regions Science and Technology.

CENTRE FOR NFLD. STUDIES
JUL 18 1978
MEMORIAL UNIVERSITY
OF NEWFOUNDLAND